Doctoral theses at NTNU, 2022:341

Cathrine Kyung Won Solem

Parametric Study of Molten Aluminium Oxidation in Relation to Dross Formation at Laboratory and Industrial Scale

Doctoral thesis

NTNU
Norwegian University of Science and Technology
Thesis for the Degree of
Philosophiae Doctor
Faculty of Natural Sciences
Department of Materials Science and Engineering

NTNU
Norwegian University of
Science and Technology

Cathrine Kyung Won Solem

Parametric Study of Molten Aluminium Oxidation in Relation to Dross Formation at Laboratory and Industrial Scale

Thesis for the Degree of Philosophiae Doctor

Trondheim, November 2022

Norwegian University of Science and Technology
Faculty of Natural Sciences
Department of Materials Science and Engineering

NTNU
Norwegian University of
Science and Technology

NTNU
Norwegian University of Science and Technology

Thesis for the Degree of Philosophiae Doctor

Faculty of Natural Sciences
Department of Materials Science and Engineering

ISBN 978-82-326-6390-3 (printed ver.)
ISBN 978-82-326-6606-5 (electronic ver.)
ISSN 1503-8181 (printed ver.)
ISSN 2703-8084 (online ver.)

Doctoral theses at NTNU, 2022:341

Printed by NTNU Grafisk senter

Preface

The present work has been a collaboration between three Norwegian partners, *i.e.*, the Norwegian University of Science and Technology, Department of Materials Science and Engineering (NTNU-DMSE) in Trondheim, Alcoa ANS (Alcoa) in Mosjøen, and Hydro Aluminium AS (Hydro) in Karmøy, within the Centre for Research-based Innovation (SFI) Metal Production funded by the Research Council of Norway (RCN) and the centre's industrial partners (project number: 237738).

The work presented focuses on molten aluminium (Al) oxidation at laboratory and industrial scales. The Al alloys 5182 and 6016 disc samples used in the laboratory scale experiments were supplied by Alcoa. Hydro also provided samples for the laboratory scale experiments and played an essential role together with Alcoa during the development of the sampling tool and the procedures used for collecting representative white dross samples. During several industrial campaigns, Alcoa welcomed and helped the author to collect industrial Al white dross samples from their casthouse at Mosjøen.

Most of the experimental part of the work presented has been performed at the lab facilities at NTNU-DMSE, with additional sample preparation activities (cryomilling) performed at the Institute for Energy Technology (IFE) at Kjeller, Norway. Surface analysis was also carried out during a research visit at Laval University in Quebec, Canada, through the CaNAl (Canada-Norway Aluminium) collaboration project funded by the RCN (project number: 274984).

The work has resulted in 6 manuscripts attached as supplements to the present thesis, 13 oral presentations at national and international conferences/seminars, and 2 poster presentations. Manuscripts 1-4 have been published, and manuscript 5 has been accepted for publication in the Journal of Sustainable Metallurgy. Due to the COVID-19 pandemic, some of the experimental work included in manuscript 6 was delayed, and data is still being processed. Therefore, this work will be included in the thesis as a preliminary manuscript. It is, however, the intention of the author to submit the manuscript for publication in the Journal of Sustainable Metallurgy.

Thesis structure

The present thesis is structured as a collection of manuscripts. An overall introduction and objectives for the present work are first given, followed by the theory of Al oxidation. Then, a summary of the first four publications presenting the oxidation at the laboratory scale is given. The next chapter presents the background of Al oxidation and dross formation at the industrial scale, followed by a summary of the two last manuscripts, including the work related to the industrial campaigns. The thesis ends with overall conclusions and an overview of possible future activities on the topic of Al oxidation/dross formation and its importance in a global prospect.

Supplements

1. **C. K. W. Solem**, K. E. Ekstrøm, G. Tranell and R. E. Aune, "Evaluation of the Effect of CO_2 Cover Gas on the Rate of Oxidation of an AlMgSi Alloy", *Light Metals 2020*, pp. 1141-1147. Winner of 2021 Light Metals Subject Award – Warren Peterson Cast Shop for Aluminum Production. DOI: 10.1007/978-3-030-36408-3_154

2. **C. K. W. Solem**, E. Solberg, G. Tranell and R. E. Aune, *"Influence of Mg Concentration on the Inhibiting Effect of CO_2 on the Rate of Oxidation of Aluminum Alloys 5182 and 6016"*, Light Metals 2021, pp. 742-750. DOI: DOI: 10.1007/978-3-030-65396-5_97

3. **C. K. W. Solem**, P. E. Vullum, G. Tranell and R. E. Aune, *"Heat Treatment of Mg-Containing Aluminum Alloy 5182 and 6016 in an Oxidizing Atmosphere with 4 % CO_2"*, *Light Metals 2022*, pp. 587-593. DOI: 10.1007/978-3-030-92529-1_77

4. **C. K. W. Solem**, P. E. Vullum, M. Ebadi, G. Tranell and R. E. Aune, *"The Role of CO_2 on the Oxidation-Protection of Mg-Containing Aluminum Alloys"*, Metallurgical Materials Transactions B, DOI: 10.1007/s11663-022-02524-3

5. **C. K. W. Solem**, S. Deledda, G. Tranell and R. E. Aune, *"Sampling Procedure, Characterization, and Quantitative Analyses of Industrial Aluminum White Dross"*, Journal of Sustainable Metallurgy, accepted for publication, October 2022.

6. **C. K. W. Solem**, S. Deledda, H. Zedel, G. Tranell and R. E. Aune, *"Effect of (5%) CO_2 on the Oxidation Rate During Cooling of Industrial Aluminum White Dross"*, to be submitted to the Journal of Sustainable Metallurgy.

Oral presentations

7. **C. K. W. Solem**, E. Solberg, G. Tranell and R. E. Aune, *"Parametric Study of Dross Formation at Industrial Scale"*, Canada and Norway Aluminium International Partnership (CaNAl IntPart) Summer School, June 14th-16th, 2022, Trondheim, Norway.

8. **C. K. W. Solem**, *"A Scientist via the Screen – How to Make Grey Aluminium Green"*, Bergen Cathedral School, April 28th, 2022, virtual seminar.

9. **C. K. W. Solem**, *"A Scientist via the Screen – How to Make Grey Aluminium Green"*, Gauldal High School, April 27th, 2022, virtual seminar.

10. **C. K. W. Solem**, E. Solberg, G. Tranell and R. E. Aune, *"Heat Treatment of Mg-Containing Aluminum Alloy 5182 and 6016 in an Oxidizing Atmosphere with 4 % CO_2"*, SFI Metal Production Spring Meeting, April 27th, 2022, Trondheim, Norway.

11. **C. K. W. Solem**, E. Solberg, G. Tranell and R. E. Aune, *"Characterisation of Oxidised Aluminium Samples and Collected Industrial White Dross"*, SFI Metal Production Webinar Series: Aluminium, March 24th, 2022, virtual seminar.

12. **C. K. W. Solem**, P. E. Vullum, G. Tranell and R. E. Aune, *"Heat Treatment of Mg-Containing Aluminum Alloy 5182 and 6016 in an Oxidizing Atmosphere with 4 % CO_2",* The TMS 2022 151st Annual Meeting & Exhibition, February 27th to March 3rd, 2022, Anaheim, California, USA.

13. **C. K. W. Solem**, E. Solberg, G. Tranell and R. E. Aune, *"Parametric Study of Molten Aluminium Oxidation in Relation to Dross Formation – Preliminary Results from Industrial Campaign"*, SFI Metal Production Dross Seminar, November 4th, 2021, Trondheim, Norway.

14. **C. K. W. Solem**, E. Solberg, G. Tranell and R. E. Aune, *"Parametric Study of Molten Aluminium Oxidation in Relation to Dross Formation: Preliminary Findings and Potential Industrial Implementations"*, SFI Metal Production Autumn Meeting, November 3rd, 2021, Trondheim, Norway.

15. **C. K. W. Solem**, E. Solberg, G. Tranell and R. E. Aune, *"Influence of Mg Concentration on the Inhibiting Effect of CO_2 on the Oxidation Rate of Aluminum Alloys 5182 and 6016",* The TMS 2021 150th Annual Meeting & Exhibition, March 15th-18th, 2021, virtual conference.

16. **C. K. W. Solem**, L. Rossato, E. Solberg, S. Akhtar, G. Tranell and R. E. Aune, *"Sampling Procedure, Microstructural Characterisation and Quantitative Analyses of Industrial Aluminium White Dross Samples"*, The 11th International Conference on Molten Slags, Fluxes and Salts. February 21st-25th, 2021, virtual conference.

17. **C. K. W. Solem**, K. E. Ekstrøm, G. Tranell and R. E. Aune, *"Evaluation of the Effect of CO_2 Cover Gas on the Rate of Oxidation of an AlMgSi Alloy"*, The TMS 2020 149th Annual Meeting & Exhibition, February 23rd-27th, San Diego, California, USA.

18. **C. K. W. Solem**, E. Solberg, G. Tranell and R. E. Aune, *"PhD Aluminium Dross – The Project and Methodology"*, SFI Metal Production Autumn Meeting, November 5th, 2019, Trondheim, Norway.

19. **C. K. W. Solem**, E. Solberg, G. Tranell and R. E. Aune, *"Parametric Study of Molten Aluminium Oxidation in Relation to Dross Formation"*, SFI Metal Production – International Dross and Packaging Recycling Workshop, May 14th-16th, 2019. Trondheim, Norway.

Poster presentations

20. **C. K. W. Solem**, S. Akhtar and R. E. Aune, *"Parametric Study of Molten Aluminium Oxidation in Relation to Dross Formation"*, The 7th International Conference & Exhibition on Aluminium, January 31st to February 3rd, 2019, Bhubaneswar, Odisha, India.

21. **C. K. W. Solem**, G. Tranell and R. E. Aune, *"Preliminary Study on Oxidation of Molten AlMgSi in an Oxidizing Atmosphere of Synthetic Air with Additions of Pure Ar and CO_2"*, The TMS 2019 148th Annual Meeting & Exhibition, March 10th-14th, 2019, San Antonio, Texas, USA.

Other relevant contributions

22. **C. K. W. Solem**, L. Rossato, E. Solberg, S. Akhtar, G. Tranell and R. E. Aune, *"Sampling Procedure, Microstructural Characterisation and Quantitative Analyses of Industrial Aluminium White Dross Samples"*, The 11th International Conference on Molten Slags, Fluxes and Salts. February 21st-25th, 2021, E-Proceedings.

Abstract

Aluminium (Al) white dross, classified as a hazardous waste, is a heterogeneous mixture of metallic Al, oxides, and non-metallic compounds (NMC) originating from the primary production route of Al. Over the past few decades, a significant number of studies have been performed on topics related to molten Al oxidation. However, the formation mechanisms are still not fully understood, nor how to inhibit the oxidation.

The overall scientific outcome of the present work has therefore been to systematically determine the extent and rate of molten Al oxidation at the laboratory scale and dross formation at the industrial scale. Special attention was given to investigating how different parameters influenced the oxidation process and whether a correlation between laboratory and industrial-scale trials could be made. During the laboratory tests, variations in the Mg concentration in the AlMg and AlMgSi alloy systems were investigated in view of Al oxidation and inhibition, as well as the effect of the heat treatment atmosphere. For the industrial campaigns, the same AlMg alloys as those investigated in the laboratory tests were reproduced, and the influence of the general furnace operations and the location in the holding furnace on the characteristics of the dross investigated. Even protective cooling of the dross was addressed and evaluated in view of inhibition of further oxidation of the metallic Al content in the hot dross compared to cooling in ambient air.

From the laboratory activities, it was concluded that additions of as small amount as 4% CO_2 into an oxidising atmosphere inhibited the oxidation rate of AlMg and AlMgSi alloys when heat treated at 750°C for 7h (normal temperature of the casthouse holding furnaces). The CO_2 in the oxidising atmosphere was identified to have adsorbed onto a MgO layer, forming an amorphous C-C layer (never observed before) and thereby inhibiting further evaporation and oxidation of Mg and breakaway oxidation. This was proven to be the case for both high- and low Mg-containing Al alloys, but to a lesser extent for the low Mg-containing Al alloy.

To allow for a systematic study with reproducible results to be performed under industrial conditions, a sampling tool and a step-by-step procedure for collecting, pulverising, and quantitatively analysing the collected samples were designed, developed, and validated. For pulverising the dross samples, both ring milling and cryomilling were used, as well as XRD and EPMA combined with deterministic image analysis for analysing the dross. It was concluded from the industrial campaigns that the dross characteristics were influenced by the furnace operations and by where in the furnace the samples were collected from. Higher metallic Al concentrations were identified for the samples collected at Location 1 (closest to the injection point of primary produced Al), and the metallic Al concentration decreased as a function of distance from Location 1 towards Location 4 (furthest away from the injection point of primary produced Al) simultaneously as the oxide/NMC concentrations increased from Location 1 to Location 4. Protective cooling under a lid with additions of 5% CO_2 proved to have an inhibiting effect on further oxidation of the dross during cooling, with lower metallic Al concentrations present in the samples cooled in ambient air. The inhibiting effect of small amounts of CO_2 in the cooling atmosphere confirms the laboratory results at an industrial scale.

Keywords: Aluminium, Aluminium magnesium, Oxidation, Dross formation, Inhibition of oxidation, Inhibition of dross formation, CO_2, Representative sampling

Acknowledgements

This work would not have been possible had it not been for the support of a great many people. To mention them all is an impossible task, however, there are some I would like to give special attention to.

First, my greatest gratitude is given to Ragnhild E. Aune. Not only have you been my supervisor, but also a role model through the past 4-5 years. Your guidance, support and discussions have been essential for making the work succeed, and I am forever grateful that you gave me the opportunity to step into the academic world.

I would also like to show my utmost appreciation to my co-supervisors. Thank you, Gabriella Tranell, for your engagement, inputs, and for sharing your knowledge. Thank you also, Egil Solberg, for your help through many industrial campaigns at Alcoa Mosjøen and with the development, trials, and valuable operational information regarding aluminium production.

The contributions from all the co-authors of the published manuscripts are also highly appreciated, and I would like to express how thankful I am for the time and involvement you all have offered to strengthen the work we have published together.

I would like to give my gratitude to Shahid Akhtar from Hydro Karmøy. Your generosity and help with planning and conducting industrial campaigns at Hydro Karmøy, as well as relevant information about the operations, have been extremely valuable for this work.

I am also grateful for Houshang Alamdari. Thank you for welcoming me to Laval University, and for your support of my experimental work. It was a valuable experience being a guest in your research group, and I hope we will meet again in the near future.

Many engineers, administration- and technical staff at NTNU have played important roles during my work, and I would like to give a special thanks to Morten P. Raanes, Dmitry Slizovskiy, Arman Hoseinpur, Berit V. Kramer, and Viviann Hole Pedersen. I would also like to thank Anne-Grethe Nilsen and Marianne Lenes for your many kind words throughout this period of my life.

After these intense years, I learned that a coffee break can do much more than adding caffeine to your system. I am deeply grateful to all my colleagues and friends for the countless hours spent on coffee breaks, ice creams, and other beverages we have shared over the years. To Kamilla, Karin, Marit, Katarina, Erlend, Massoud, Daniel, SiMnTiAl-friends, seniors, and juniors that always have had a smile and a laugh to share: You have made the journey as valuable as the goal.

Finally, the greatest gratitude is warmly given to my family. Mum and dad, I am forever grateful that you have always supported me and allowed me to pursue what I am passionate about. It cannot be said enough how grateful I am for you. Anne, you have been there through loud discussions and silent hours and have been present even when we have been apart. I thank you for that. And last, my Julian Bradley, I believe that no words are needed.

Cathrine KW Solem

September 8th, 2022, Trondheim

Nomenclature

Abbreviation	Description
CE	Circular Economy
DSC-TG	Differential Scanning Calorimetry and Thermogravimetry
EDS	Energy Dispersive X-ray Spectrometry
EELS	Electron Energy Loss Spectroscopy
EOL	End-of-life
EPMA	Electron Probe Microanalysis
FIB	Focused Ion Beam
GHG	Greenhouse Gas
HAADF	High Angle Annular Dark Field
LAADF	Low Angle Annular Dark Field
NMC	Non-Metallic Compound
OES	Optical Emission Spectroscopy
SEM	Scanning Electron Microscopy
STEM	Scanning Transmission Electron Microscopy
TEM	Transmission Electron Microscopy
TG	Thermogravimetry
UBC	Used Beverage Can
XPS	X-ray Photoelectron Spectroscopy
XRD	X-Ray Diffraction

Symbols	Description
C_0	Concentration before diffusion
C_s	Concentration at the surface after time t
C_x	Concentration at distance of diffusion x after time t
C	Celsius
D	Diameter
D	Diffusion coefficient
ΔG^0	Gibbs free energy at the standard state
J	Diffusion flux
p_x	Partial pressure
S	Seconds
T	Temperature
t	Time
x	Distance/thickness in the direction of diffusion

Chemical formulas	Chemical name
Al_2Ca	Aluminium calcium
Al_2O_3	Aluminium oxide (alumina)
Al_4C_3	Aluminium carbide
AlMg	Aluminium magnesium
AlMgSi	Aluminium magnesium silicon
AlN	Aluminium nitride
$AlSr_4$	Aluminium strontium
BeO	Beryllium oxide
$C_{10}H_8$	Naphthalene
$CaAl_2O_4$	Calcium aluminate
$CaCO_3$	Limestone
CaF_2	Calcium fluoride
CH_4	Methane
CO_2	Carbon dioxide
H_2S	Hydrogen sulfide
HF	Hydrogen fluoride
KCl	Potassium chloride
$MgAl_2O_4$	Spinel
MgO	Magnesium oxide (periclase)
Na_3AlF_6	Cryolite
NaCl	Sodium chloride
NH_3	Ammonia
PH_3	Phosphine
SO_2	Sulfur dioxide

Table of Contents

Chapter 1 Introduction

1.1 Oxidation and aluminium dross formation

Aluminium (Al) was not discovered until the mid-1800s, and at the time, it was more valuable than gold (Au) due to its rareness[1, 2]. During the last century, however, the manufacturing of Al has become one of the most commonly known processes and Al the second most important material in our modern society[3–5]. The demand for Al is rapidly increasing[5, 6], and with the recent developments in the automotive industry, the growth of cities around the world, and the use of Al in the power industry, Al have strengthened its position as one of the key structural materials of the 21st century.

The primary production of Al is presently responsible for ~3.5% of the global use of electricity, and the industry was in 2009 reported being responsible for approximately 1.1% of the greenhouse gas (GHG) emissions[5, 7]. It is, therefore, essential that the losses of metallic Al during production are kept to a minimum to avoid any unnecessary spills. Even though the recycling of post-consumer Al scrap is increasing, there will still be a need to continue to produce Al through the primary production route for many years to come as new applications are continuously arising in addition to today's use, see Fig. 1.1[8, 9].

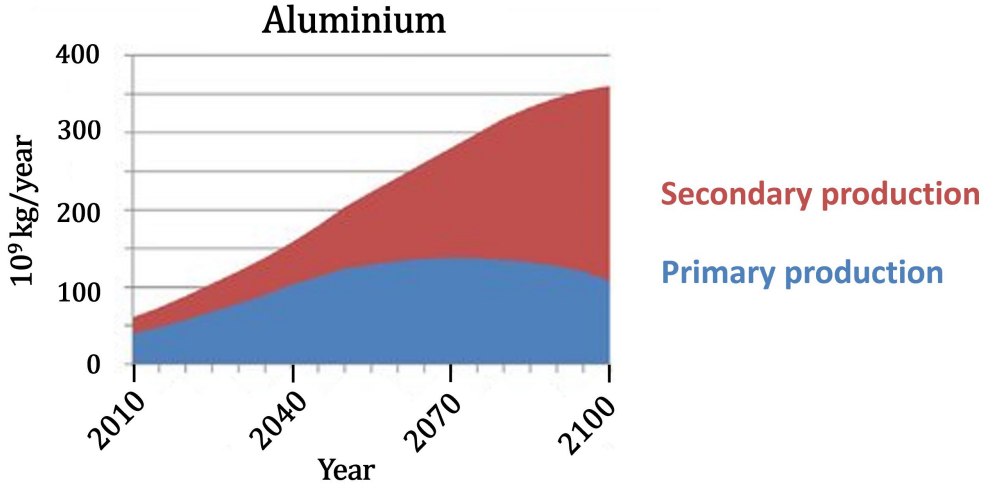

Fig. 1.1: The primary and secondary production of aluminium (Al) following a circular economy scenario predicted for 2010-2100. Reproduced from Van der Voet et al.*[9].*

To maximise the metallic yield of the primary produced Al, it is critical to minimise the losses of Al during furnace operations. It is, however, well-known that Al, as well as some of the most used alloying elements, *e.g.*, magnesium (Mg) and silicon (Si), are more stable

as oxides than as pure metals at higher temperatures. As a result, oxidation of Al is unavoidable when exposed to oxygen-containing atmospheres[10]. The alloying elements may also affect the mechanism of the oxidation process and, thereby, the structure and morphology of the formed oxides.

1.1.1 Al melt treatment operations

During Al melt treatment operations in the casthouse holding furnaces, the melt is prepared for casting by adding different alloying elements mixed with primary produced Al[11]. This involves several furnace operations, such as (i) injection of the primary produced Al, (ii) addition and stirring of alloying elements to ensure complete homogenisation, as well as (iii) skimming to remove the oxides and non-metallic compounds (NMCs) floating on top of the hot pool of metallic Al[12]. The present state-of-the-art procedure for removing the oxides and NMCs is based on the use of a rake that is manually controlled by one of the furnace operators, see Fig. 1.2[13]. As the oxide layer is removed, unreacted metallic Al is constantly exposed to the oxidising atmosphere in the air, increasing the white dross formation. Dross is, in other words, an Al-containing residue formed during smelting, melt treatment, and casting of primary produced Al.

During the skimming step, the dross is carefully held at the furnace gate to drain off as much excess metallic Al as possible, and thereby minimising the losses, before being transferred to dross bins for cooling. It is, however, challenging to balance the removal of oxides/NMCs and metallic Al as alloying elements may also be removed at the same time[14]. The loss of metallic Al in the skimming process can result in the dross containing as much as 10% of the metallic Al annually produced[15].

Fig. 1.2: Image of the skimming of an Al melt, where dross bins are placed in front of the furnace gate to collect the oxides and non-metallic compounds (NMCs) floating on top of the melt before casting. Metallic Al is entrained, generating Al-rich white dross. © 2021, Alcoa Mosjøen, Norway.

1.1.2 Effect of alloying elements on Al dross formation

Different parameters have been mentioned to enhance the Al dross formation, of which some are easier controlled during process operations and others are more complex. For example, an increasing Mg concentration in the alloy will increase the oxidation rate of the molten Al, however, Mg is a crucial alloying element that secures the mechanical properties of the final product and thereby an essential addition to molten Al[14, 16]. The atmosphere in the casthouse holding furnace has also been discussed as a critical parameter, as well as the atmosphere in contact with the dross during cooling. In view of the latter, it has been reported in the literature that purging argon (Ar) onto the dross during cooling by placing large lids over the dross bins inhibits further oxidation of the metallic Al present in the dross and thereby secures a higher recovery of metallic Al when re-melting the dross[17].

1.1.3 Environmental impact of Al dross formation

There are various reasons why Al dross is undesirable. In addition to the decreased metallic yield obtained during Al production, dross is defined as a hazardous waste that has to be handled and treated following strict routines due to the generation of toxic gases when in contact with the humidity in the air and/or rain (water)[4, 18, 19].

A global review published in 2020 identified that up to 50% of the dross generated today is still landfilled[20]. When the dross is reacting with the moisture in the soil, undesirable reactions take place and can cause landfill fires due to the flammable gases generated[21]. In view of this, it is not only desirable to reduce the dross formation to increase the metallic Al yield but also to lower the negative environmental impact of the Al industry.

1.2 Project scope

The overall scientific outcome of the present study has been to systematically determine the extent and rate of molten Al oxidation at the laboratory scale, as well as investigate how oxidation at the industrial scale, *i.e.*, dross formation, is influenced by different parameters. The scientific impact of the work has been to reduce dross formation by improving casthouse operations. Fig. 1.3 shows the overall scope and structure of the project, as well as the link between the different parts, *i.e.*, between the laboratory and industrial activities supported by thermodynamic calculations.

The laboratory work summarised in Fig. 1.3 is based on the experiments performed in a Differential Scanning Calorimeter equipped with a Thermogravimetric analyser (DSC-TG), exposing disc samples to different cover gases during heat treatment. The obtained data, as well as the metallographic evaluation of the disc samples before and after heat treatment, were supported by thermodynamic calculations in view of the oxidation rate of Al. The specific Al alloy systems investigated were selected based on their importance to the industry and widespread use.

The industrial work summarised in Fig. 1.3 is based on developing a dross sampling tool, as well as a detailed step-by-step sampling procedure supported by suitable powder preparation

and characterisation techniques. Samples were collected from the casthouse holding furnace at Alcoa's facilities at Mosjøen in Norway during 7 campaigns and experimentally controlled to be safe in view of the release of phosphine (PH_3) gas before being further processed and analysed. The experimental evaluation of the safety of the dross samples was supported by thermodynamic calculations. The industrial results were linked to the laboratory findings to identify the parameters that enhanced and inhibited the oxidation rate of Al.

The overall result from the present work was reviewed based on (i) the collection of reproducible dross samples from the holding furnace, (ii) the influence of the chemical composition of the Al alloy produced with focus on the Mg content, (iii) the heat treatment/cooling atmosphere of disc samples and industrial dross samples and their influence on the oxidation rate of Al, and the (iv) the inhibiting effect of small additions of CO_2 to the oxidating atmosphere.

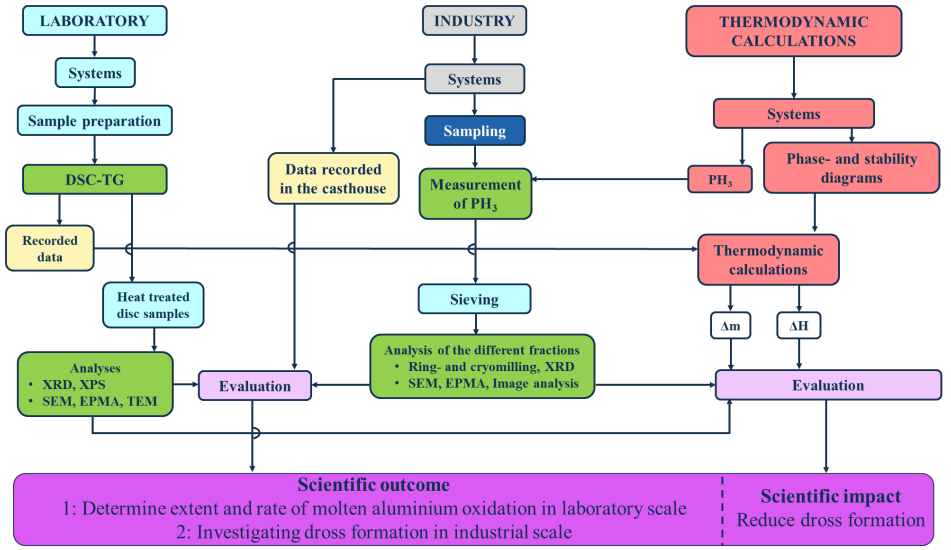

Fig. 1.3: Flow sheet of the project showing the scope and structure of the laboratory and industrial activities, as well as the supporting thermodynamic assessment.

Chapter 2 Background

2.1 Production of aluminium

For the production of Al, there are today two conventional routes, *i.e.*, the primary and secondary routes. In Fig. 2.1, a simplified flow sheet of the two production routes is presented, where the orange arrows illustrate the primary production route, the blue arrows the secondary production route, and the double-coloured arrows are part of both routes[22, 23].

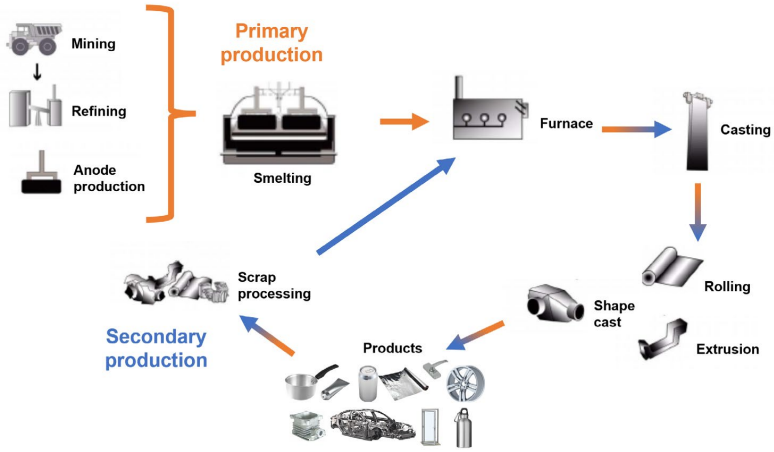

Fig. 2.1: Flow sheet of the conventional production routes of Al, where orange and blue arrows mark the primary and secondary routes, respectively (the double-coloured arrows are part of both routes)[22, 23].

As previously mentioned, the primary route for the production of Al is still the dominating route (see Fig. 1.1), however, it is predicted that the secondary route will overtake the primary route in the near future[9]. Based on data published by the International Aluminium Institute in 2022, over 1.5 billion tons of Al were produced from 1973 to 2021 through the primary production route, and in 2021 China had more than 50% of the world's production[24]. The Al industry is estimated to be responsible for 3.5% of the electricity use worldwide, which equals about 1.1% of the global CO_2 emissions[5].

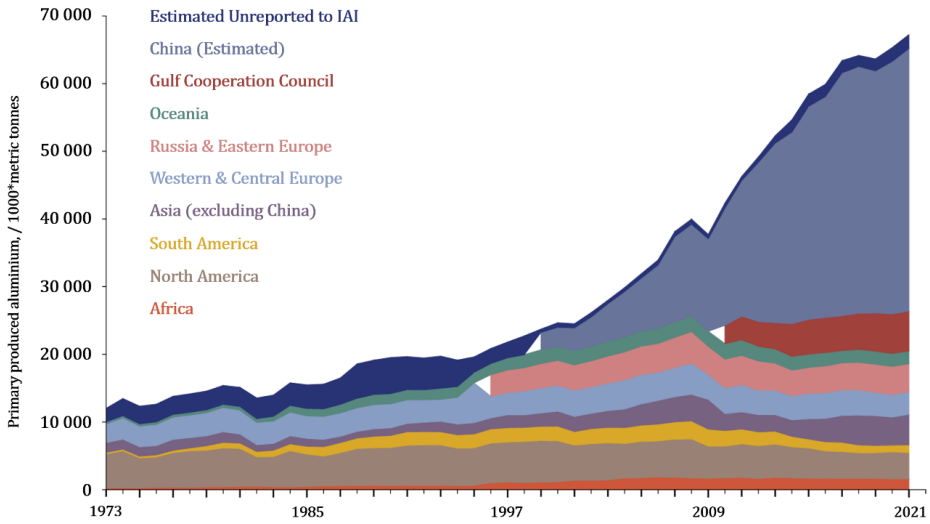

Fig. 2.2: The primary production of Al in thousands of tonnes, from 1973 to 2021, given by regions. Reproduced from © International Aluminium Institute[24].

2.1.1 The primary production of Al

The primary production route of Al, as we know it today, was not industrialised until the late 1800s. From the bauxite ore, rich in H_2O-bonded Al_2O_3 (40-60%), Al_2O_3 is extracted by the Bayer process and further used as the raw material for the production of Al through the Hall-Héroult process (which is an electrochemical reduction process)[25]. The overall reaction for the primary production of Al is presented in Eq. 2.1:

$$\frac{1}{2}\,Al_2O_3\ \text{diss.} + \frac{3}{4}\,C\ (s) = Al\ (l) + \frac{3}{4}\,CO_2\ (g) \qquad \text{Eq. 2.1}$$
$$\Delta G^0_{960°C} = 345.1\ \text{kJ/mol}$$

In the Hall–Héroult process, Al_2O_3 is dissolved into a solution containing cryolite (Na_3AlF_6), aluminium fluoride (AlF_3) and calcium fluoride (CaF_2), which reacts with the C anodes producing molten Al together with CO_2[26]. As the Gibbs Free Energy of the reaction presented in Eq. 2.1 is >> 0 kJ, a significant amount of electricity is used to drive the reaction to the right. Cryolite is, therefore, commonly added to the process to lower the melting point of Al_2O_3[27, 28], which also results in the need for less energy to reduce the Al_2O_3. Additions of cryolite do, however, introduce fluor (F) into the process, which is found both as an impurity in the melt and as part of the off-gas in the form of the very hazardous compound hydrogen fluoride (HF)[29].

2.1.2 The secondary production of Al

In Fig. 2.1, it can be seen that it is end-of-life (EOL) products that are the input material in the secondary production route of Al, *e.g.*, used beverage cans (UBCs), cream cheese tubes,

window frames, and other Al products (often referred to as post-consumer scrap). Because the input material is heterogeneous in both chemical composition and geometrical form, it is crucial that the scrap is collected and pre-treated before being melted. This can include milling and shredding steps to ease the sorting, as well as other pre-treatment steps to ease the melting, *i.e.*, pre-heating to remove organic materials and compaction of the scrap[30–32].

The milled/shredded/pre-treated scrap is then fed into a furnace and remelted together with salts, *e.g.*, a mixture of sodium chloride (NaCl) and potassium chloride (KCl), to improve the coalescence of the Al by removing the oxide films[33]. Both (tilting) rotary furnaces and casthouse melting/holding furnaces are in use[34].

The most energy-consuming step during primary production of Al is the reduction of Al_2O_3 in the Hall-Héroult process, a process step which is not part of the secondary route. In view of this, a decrease of ~95% of the energy needed to produce 1 kg of Al is obtained through the secondary production route[35].

It should not be underestimated that the lower energy consumption is one of the reasons why the secondary production route of Al has experienced such a massive leap in use during the last decades. For example, in 2007, Xiao *et al.*[36] reported that 40% of the post-consumer scrap originating within Europe was recycled through the secondary route and 50% in the United States (US). It should, in this regard, be noted that ~75% of all Al ever produced are still in use because of the reuse of post-consumer scrap[27].

2.2 Theoretical approach to oxidation

Oxidation of metals has been studied in detail for over a century, and the overall reaction, as it is often presented, is given in Eq. 2.2 where *Me* can be any substance or metallic element. As can be seen from the reaction, oxidation takes place when a substance/metal (*Me*) comes into contact with O_2 (g) or with another oxidising substance.

$$x\mathrm{Me} + \tfrac{1}{2}\, y\mathrm{O_2} = \mathrm{Me_xO_y} \qquad \text{Eq. 2.2}$$

The mechanism behind the oxidation reaction in Eq. 2.2 is presented in Fig. 2.3, where an O_2 (g) molecule is adsorbed onto a metal surface, and the nucleation of oxide is initiated. As the oxide film continues to grow, diffusion of O_2 towards the bulk will also occur through cracks, causing internal oxidation, porosity, formation of potential molten oxide phases, and oxide evaporations[37].

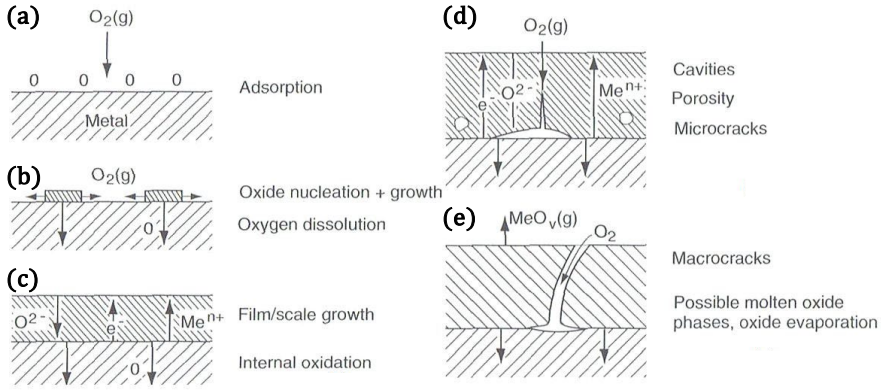

Fig. 2.3: Mechanism of oxide film growth on a metal surface. © 2012 Izman et al.*[37].*

In view of oxidation, iron (Fe) was the first system to be studied, followed by copper (Cu). Even how oxide nuclei were grown on the top metal surface of these elements was early given special attention[38].

2.2.1 Thermodynamics of Al oxidation

In Fig. 2.4 the Gibbs Free Energy (ΔG^0) at the standard pressure (p^0) has been plotted as a function of temperature for Al when reacting with 1 mole of O_2 (g). Even reactions for some of the alloying elements used during the production of the most common Al alloys, *i.e.*, Mg, Si, and Mn, have been added to the same plot. From this simple illustration of the well-known Ellingham diagram, the different element's stability in view of oxidation can be evaluated, and standard ΔG^0 values retrieved as a function of temperature. Even the equilibrium composition of the system can be calculated. It should be noted that the standard ΔG^0 values are nothing more than lower integration constants, however, they are very useful when evaluating the stability of different elements in a multi-component system.

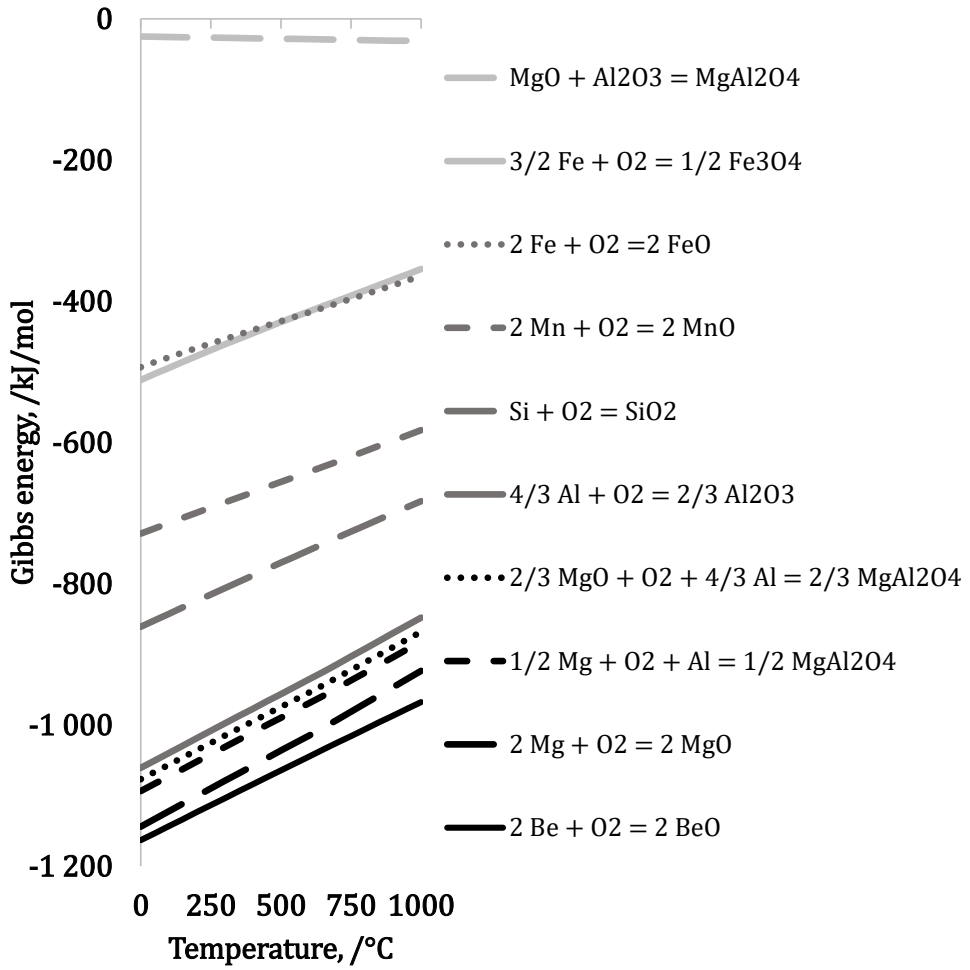

Fig. 2.4: Standard Gibbs Free Energy (ΔG^0) in kJ/mol for typical alloying elements reacting with 1 mole O_2[39].

From the diagram in Fig. 2.4, it can be seen that all included reactions have negative ΔG^0 for the temperature range given, *i.e.*, from 0 to 1000°C, meaning that they all are favoured to the right (towards the oxide state)[39, 40]. The reaction between metallic Al and O_2 (g) can be found in the middle part of the diagram. As the standard ΔG^0 change for the Al reaction is greater (more negative) relative to the reactions for Si, and Mn at all temperatures, the equilibrium constant is larger for the Al reaction, which is the reason why Si and Mn that appear higher up in the diagram are more stable than Al. As the standard ΔG^0 change for all the reactions is negative, the large decrease in entropy must be counteracted by a large enthalpy of the reaction. In other words, the relative stability of the oxide of Al compared with the oxide of the other elements is due to the much larger standard enthalpy of the reaction.

In view of this, Al's higher affinity to O is a known characteristic commonly used to protect other materials from corrosion as a protective Al_2O_3 film is formed[41]. However, elements below Al in the diagram (Fig. 2.4) are more stable as oxides and will oxidise before Al, and may thereby hinder Al from oxidising.

As previously mentioned in section 1.1, all of the elements in question are more stable as oxides than as pure elements, which is the driving force for oxidation during melt treatment. The reactions presented in Fig. 2.4 can also be found in Eq. 2.3 to Eq. 2.12 for clarity together with the equations for respective reactions standard ΔG^0 at 750°C (typical casthouse temperature during Al production)[42].

$$MgO\ (s) + Al_2O_3\ (s) = MgAl_2O_4\ (s) \quad \Delta G^0_{750°C} = -29.77\ kJ/mol \qquad \text{Eq. 2.3}$$

$$^3/_2\ Fe + O_2 = ½\ Fe_3O_4 \quad \Delta G^0_{750°C} = -391.93\ kJ/mol \qquad \text{Eq. 2.4}$$

$$2\ Fe + O_2 = 2\ FeO \quad \Delta G^0_{750°C} = -396.65\ kJ/mol \qquad \text{Eq. 2.5}$$

$$2\ Mn\ (s) + O_2\ (g) = 2\ MnO\ (s) \quad \Delta G^0_{750°C} = -619.57\ kJ/mol \qquad \text{Eq. 2.6}$$

$$Si\ (s) + O_2\ (g) = SiO_2\ (s) \quad \Delta G^0_{750°C} = 726.14\ kJ/mol \qquad \text{Eq. 2.7}$$

$$^4/_3\ Al\ (l) + O_2\ (g) = {}^2/_3\ Al_2O_3\ (s) \quad \Delta G^0_{750°C} = -903.01\ kJ/mol \qquad \text{Eq. 2.8}$$

$$MgO\ (s) + O_2\ (g) + {}^4/_3\ Al\ (l) = {}^2/_3\ MgAl_2O_4\ (s) \quad \Delta G^0_{750°C} = -922.11\ kJ/mol \qquad \text{Eq. 2.9}$$

$$½\ Mg\ (l) + Al\ (l) + O_2\ (g) = ½\ MgAl_2O_4\ (s) \quad \Delta G^0_{750°C} = -936.86\ kJ/mol \qquad \text{Eq. 2.10}$$

$$2\ Mg\ (l) + O_2\ (g) = 2\ MgO\ (s) \quad \Delta G^0_{750°C} = -981.08\ kJ/mol \qquad \text{Eq. 2.11}$$

$$2\ Be + O_2 = 2\ BeO \quad \Delta G^0_{750°C} = -1015.58\ kJ/mol \qquad \text{Eq. 2.12}$$

2.2.2 Kinetics of Al oxidation

Smeltzer[43] proposed in 1956 that not one oxidation rate alone could explain the kinetics of the oxidation of Al, but rather three, *i.e.*, (i) a rapid rate, (ii) a linear constant rate, and (iii) a slow parabolic rate. This is also partly illustrated in Fig. 2.3, where Al is the metal/substance in question, and the Al_2O_3 film can be seen attached to and grow on top of

its Al metal surface. From the figure, it is realised that the oxidation process of Al can be described both as a rapid and as a slow process[44].

Jeurgens *et al.*[45] observed in their research that the growth of the oxide layer thickness initially occurs rapidly, followed by a slower rate after ~15 000 s (4 h 20 min). From their results, the growth rate of the oxide layer thickness as a function of time was calculated, see Fig. 2.5, where (a) shows the oxide layer thickness, Fig. 2.5 (b) the growth rate, and Fig. 2.5 (c) the change in growth rate[45].

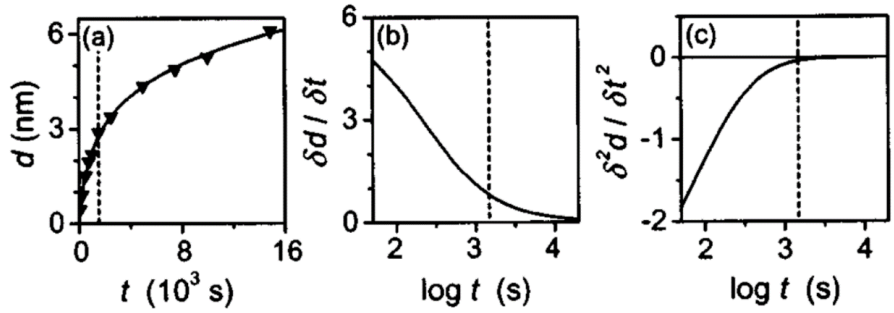

Fig. 2.5: Oxide growth thickness as a function of time for an Al substrate heat treated at 773 K (p_{O2} = 1.33 × 10^{-4} Pa), where (a) shows the thickness of the oxide layer, (b) shows the growth rate of the oxide layer thickness, and (c) shows the change in the growth rate of the oxide layer thickness. © 2002 American Institute of Physics, Jeurgens et al.*[45].*

Based on some of the observations, a theoretical approach to the kinetics of Al oxidation can be made through Fick's first and second laws. According to Fick's first law (Eq. 2.13), the concentration gradient from the surface towards the bulk is fixed. However, this is not the case for Fick's second law (Eq. 2.4), as it is defined as non-steady state diffusion.

$$J = -D\frac{\partial C}{\partial x} \qquad \text{Eq. 2.13}$$

$$\frac{\partial C}{\partial t} = D\frac{\partial^2 C}{\partial x^2} \qquad \text{Eq. 2.14}$$

In the above equations, J is the diffusion flux, D the diffusion coefficient, C the concentration, x the thickness of the oxide layer, and t the time[46]. The solution of Fick's second law is given in Eq. 2.15, where the bulk concentration after diffusion at a distance x (C_x), the surface concentration (C_s), and the initial concentration before diffusion (C_0) are fixed for a specific time t. In view of this, it can be expressed that the depth from the surface into the bulk x is a function of the square root of the time t, as seen in Eq. 2.16.

$$\frac{C_x - C_0}{C_s - C_0} = 1 - \text{erf}\left(\frac{x}{2\sqrt{Dt}}\right) \quad \text{Eq. 2.15}$$

$$x = \sqrt{t} \quad \text{Eq. 2.16}$$

The solution to Fick's second law correlates well with the findings of Jeurgens *et al.*[45] and the shape of the oxide layer thickness graph (Fig. 2.5 (a)) as a function of time.

2.2.3 Oxidation of AlMg alloys

Aluminium magnesium (AlMg) alloys are an essential group of Al alloy as the Mg content improves the final product's mechanical properties, as well as corrosion resistance. The alloys are therefore well suited for seawater applications, *e.g.,* boats and other vehicles[42]. Studies performed on the oxidation of AlMg alloys have shown that adding Mg increases the oxidation rate of Al[47, 48] through different possible reactions favoured under production conditions.

One such reaction is Eq. 2.11, where Mg (l) and MgO (s) are in equilibrium at 750°C. The logarithmic partial pressure of O_2 (g) can for this reaction be calculated to a value of log p_{O2} = -45.63[39], which reveals that MgO is more stable than $MgAl_2O_4$ (log p_{O2} = -43.58 for Eq. 2.14) and Al_2O_3 (log p_{O2} = -42.00 for Eq. 2.13) and will therefore be favourably formed. This is a well-known oxidation step during the production of AlMg alloys[49].

To study the different steps of the oxidation process in more detail, the process is often graphically described with a mass-gain curve, where the mass change is on the y-axis, and time on the x-axis, giving the classical S-shaped mass gain curve, as seen in the lower part of Fig. 2.6[50, 51]. In the linear segment of the curve, the mass gain is controlled by the Mg concentration in the alloy until reaching steady state. At steady state, the Mg has completely oxidised, forming a MgO layer on top of the Al alloy. The oxidation process will continue as long as elemental Mg is available in the system, initiating breakaway oxidation.

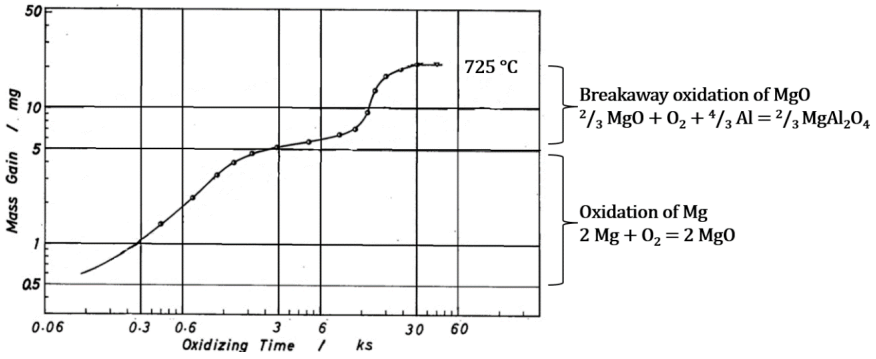

Fig. 2.6: Oxidation and breakaway oxidation of an AlMg alloy with 10 wt.% Mg, heat treated at 725°C in dried air. © 1983 Transactions of the Japan Institute of Metals, Haginoya and Fukusako[50].

Breakaway oxidation is the oxidation process of MgO and is graphically presented in the upper part of Fig. 2.6[50]. This is the second step of the oxidation process occurring after the oxidation of Mg, and it has been reported to occur whenever the activity of Mg at the very top surface of the Al alloy decreases below 0.023[49]. However, if the activity of Mg is higher than 0.023, $MgAl_2O_4$ will not form as MgO is favoured[49, 52].

Impey *et al.*[53] established that the dross formation mechanisms for AlMg alloys are similar to that of pure Al. It was reported that for a pure Al melt, a γ-Al_2O_3 film was formed on top of the melt. With time, the γ-Al_2O_3 would then transform to η-Al_2O_3 and cause the oxide layer to rupture due to the volume changes resulting in a nodular oxide layer[53].

The same observation was made for AlMg melts but initiated by forming a layer with clusters of MgO. The MgO further initiated the formation of the crystal growth of $MgAl_2O_4$ at the interface between the melt and the oxide, followed by complete breakaway oxidation, which is the initial stage of dross formation[53].

In view of this, it should be noted that several reactions may occur during the oxidation of AlMg alloys, as presented in Eq. 2.3, Eq. 2.9 and Eq. 2.10. Based on the standard ΔG^0 values for these reactions, it can be seen that Eq. 2.10, representing the oxidation of Mg to $MgAl_2O_4$ (s), has the lowest ΔG^0 at 750°C (-936.86 kJ/mol), and will therefore be the first of several possible breakaway oxidation reactions to take place, given that there is free Mg (l) left in the system.

2.3 Inhibition of oxidation

Oxidation of Al has been a challenging topic for a long time, and so is also the case with inhibition of oxidation. Several parameters have been investigated as potential inhibitors aiming to retard the oxidation process and thereby increasing the metallic Al yield. In view of this, most of the published literature has focused on reducing the partial pressure of O_2 in the system.

Some potential inhibitors that have been investigated over the years, as well as the effect of the atmosphere and its influence on the oxidation rate, will be summarised and discussed in the coming sections.

2.3.1 The effect of alloying elements

Beryllium (Be)

In 1954, the inhibiting effect of beryllium (Be) was studied, and it was established that as small amounts as 0.0001 wt.% Be in an AlMg10 alloy significantly impacted the oxidation rate[54].

Beryllium was and still is, used at some Al plants during production to inhibit the oxidation rate for high Mg-containing Al alloys and thereby retard the breakaway oxidation of MgO by forming a protective BeO film[55, 56]. As seen in Fig. 2.4, BeO is more stable than MgO

and $MgAl_2O_4$ and will therefore be favoured. The BeO film will inhibit further diffusion of O_2 towards the bulk and hinder the diffusion of Mg towards the surface[57, 58]. It should, however, be noted that due to the toxicity of Be, even at low concentrations, its use has been questioned in many parts of the world[55, 59].

Calcium (Ca)

Calcium (Ca) is in the same group of the periodic table as Mg and Be and is also capable of forming an oxide. Yoon *et al.*[60] reported that additions of 0.03 wt.% Ca through aluminium calcium (Al_2Ca) additions to an AlMg5 alloy had an apparent inhibiting effect on the mass gain during heat treatment (reducing the mass gain from 10% to 0.01%), as well as on the oxide layer thickness, which was significantly reduced. It was concluded that a protective CaO layer had formed and mixed with MgO, preventing breakaway oxidation. Ha *et al.*[61] observed the same inhibiting behaviour when adding small amounts of Al_2Ca. It should, however, be noted that Ca has been reported to negatively influence the Al product when rolled and is often seen as an impurity causing edge cracking[62].

Strontium (Sr)

Strontium (Sr) has also been investigated as an alloying element for AlMg alloys. Different effect of adding small amounts of Sr has, however, been found in the literature. For example, Ozdemir *et al.*[63] reported that when comparing AlMg alloys (0.5 wt.%, 1 wt.%, and 5 wt.% Mg) with and without small additions of Sr, a clear drop in the mass gain was seen for the alloys with Sr additions. However, the drop in mass gain decreased with an increasing amount of Sr, ranging from 250-1000 ppm. Another study reported that when adding 300 ppm Sr to an AlSi7Mg0.35 alloy, the oxidation rate increased[64]. Additions of Sr are therefore still questioned, as it may increase the oxidation rate and cause an increased porosity which in turn causes lower strength and poorer machinability[65].

Sodium (Na)

Sodium (Na) was reported to have an enhancing effect on the oxidation rate of Al alloys. However, Cochran *et al.*[66] proved that Na has an inhibiting effect for AlMg (0.7 wt.% Mg) alloys. By adding as small amounts as 0.0002% Na during heat treatment at 725°C, the oxidation rate of the Mg in the alloy was significantly decreased. The oxidation of the alloy was prolonged even further when adding 0.003% Na to the alloy[66]. The presence of small amounts of Na in the melt (even as low as <125 ppm) can, however, jeopardise the quality of the final product.

2.3.2 The effect of atmosphere

Argon

For oxidation to occur, O_2 must be present in the system. Several experimental studies have therefore been performed using inert gas to protect the melt from oxidation. By removing the oxidant from the system, oxidation should, theoretically, not take place. Nitrogen (N_2)

has also been studied, and Cochran *et al.*[66] reported that by adding N_2 to the atmosphere, the breakaway oxidation step was postponed but not prevented.

Carbon dioxide (CO_2)

Haginoya and Fukusako[67] reported that a mixture of CO_2 and air inhibited the mass gain of an AlMg10 alloy after heat treatment at 750°C for 250 min. The proposed mechanism was that the CO_2 prevented the diffusion of O_2 towards the bulk and that 30-70% CO_2 had the greatest inhibiting effect compared to pure air or 100% CO_2, see Fig. 2.7.

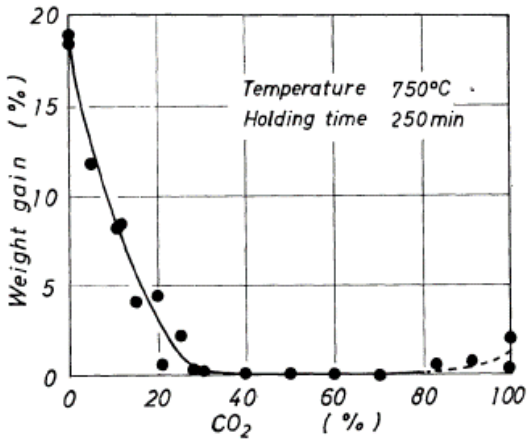

Fig. 2.7: Mass gain as a function of CO_2 concentration mixed with air after heat treatment of an AlMg10 alloy at 750°C for 250 min. © 1979 Transactions of the Japan Institute of Metals, Haginoya and Fukusako[67].

The same inhibiting effect was confirmed by Stevens *et al.*[68], but they reported that 10% CO_2 mixed with synthetic air had a more significant inhibiting effect than 50% CO_2 when an Al-Mg alloy was heat treated at 800°C for 4 h. The inhibiting effect of the lower amount of CO_2 was later confirmed by Smith *et al.*[69] as they reported that 5% CO_2 mixed with synthetic air had the best inhibiting effect when compared with 20% and 50% CO_2 during heat treatment of an AlMg5 alloy at 750°C. In this connection, CO_2 was reported to retard the evaporation of Mg, inhibiting the oxidation rate and thereby influencing the oxide layer morphology.

Flue gas

The effect of flue gas, also known as recirculation gas with a chemical composition of CO_2, N_2 and water moisture, has also been investigated. Cochran *et al.*[66] investigated if flue gas had an inhibiting effect on the oxidation rate of AlMg alloys, reporting that its presence delayed the breakaway oxidation step but did not prevent it.

Water (H_2O)

Thiele[70] reported that the presence of water vapour inhibited the oxidation of pure Al (99.9%) when heated at 800°C, as the mass gain was significantly decreased compared to when heated in air. In the case of an AlMg alloy, *i.e.,* Al alloy 5052 (2.35 wt.% Mg), Cochran and Sleppy[47] reported that the presence of water vapour in the atmosphere during heat treatment prevented the Mg in the alloy from evaporating, resulting in an inhibiting effect of the oxidation rate of the alloy. It was also established by Impey *et al.*[71] that humid atmospheres stabilised the Al_2O_3 layer of AlMg alloys, which inhibited further oxidation.

It should, however, be noted that water vapour has also been established to have a prompting effect, increasing the oxidation rate of Al[72]. In regards to this, Schoenitz *et al.*[73] reported that when heat treating pure Al particles in an atmosphere of Ar mixed with steam, the oxidation process was completed at a lower temperature than when heat treating the same alloy in dry O_2, *i.e.*, at 1000°C compared to 1500°C.

Sulfur dioxide (SO_2)

Sulfur dioxide (SO_2) has also been studied as an inhibitor for the oxidation of Al and its alloys. Belitskus *et al.*[74] investigated the inhibiting effect of adding 10-100% SO_2 into the atmosphere during prolonged heat treatment (100 h) of a commercial aluminium alloy 5086 (AlMg4.0Mn0.45Cr0.10) at 750°C. It was reported that when comparing the outcome with the heat treatment of the same alloy in compressed air (<0.1 vol.% H_2O), the mass gain was significantly reduced. The presence of MgO on the top surface of the alloy, as well as small amounts of $MgSO_4$, was identified by X-Ray Diffraction (XRD) and believed to protect the alloy from further oxidation[74].

2.4 Oxidation at an industrial scale

There are several stages of metal handling during primary production of Al, and during each stage of the process, there is potential for oxidation of the molten Al metal to take place. As discussed above, oxidation will occur at any time when the molten metal surface is exposed to the atmosphere, which happens when the melt handling step disrupts the oxide surface. In addition to direct surface oxidation, metallic Al can also be entrained in the oxides, *i.e.*, when the metal is physically contained within the oxide itself, which happens during any turbulent event associated with melt handling, see Fig. 2.8. For example, during alloy additions or additions of primary produced Al in the casthouse furnace, the surface of the hot metal pool will be disrupted due to imposed turbulence, exposing the molten metal surface to the atmosphere. The metallic Al and the alloying elements will then oxidise, and other NMCs floating on top of the melt, as well as oxide films and gas bubbles in the bulk, form white dross.

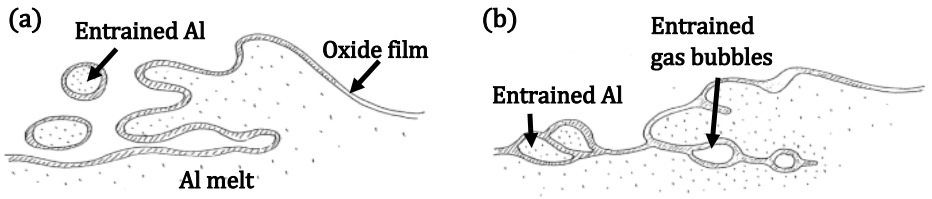

Fig. 2.8: An Al melt where (a) an oxide film has formed on top of the melt, and entraining Al lumps, and (b) entraining of Al and gas bubbles in the bulk of the melt. Reproduced from © 1991, 2003, Elsevier Science Ltd., J. Campbell[75].

To cast the Al bath, the dross and NMC mixture must be removed by skimming, see Fig. 2.9. The areas marked with white dotted lines in the figure show an uncleaned area covered in floating oxides/NMCs, and the areas marked with black dotted lines are the underlying molten metal surfaces being exposed to the atmosphere.

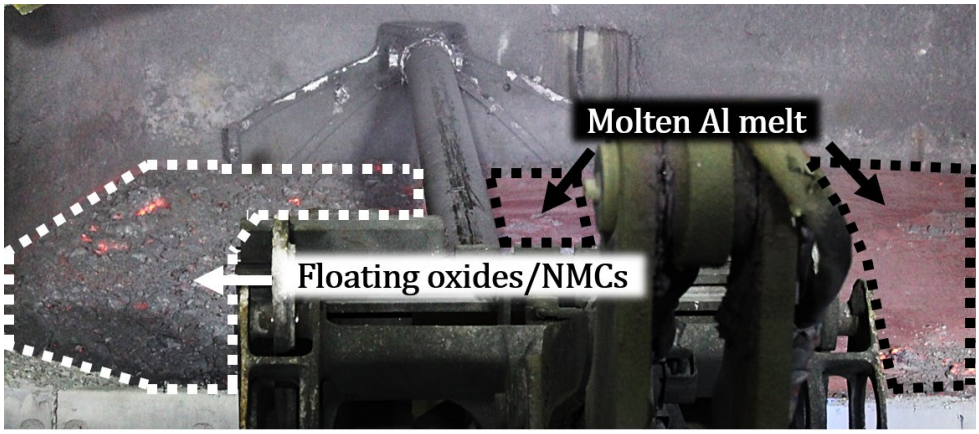

Fig. 2.9: Floating oxides/NMCs being removed (skimmed off) an Al melt. © 2019, Alcoa Mosjøen, Norway.

The formation of white dross and NMCs during primary production of Al is directly related to oxidation. Most of the oxides/NMCs are produced in the furnace itself, especially during the filling of the furnace, which is considered to be one of the primary sources of oxide formation. General furnace treatment, stirring, dross removal, alloying, scrap additions, and sludge removal are all metal handling steps associated with oxidation of the molten Al metal in one way or another. However, there is uncertainty as to which steps besides the filling of the furnace that is the most significant contributor.

To attempt to control and minimise oxidation and thereby dross formation, it is necessary to determine where and how the dross is produced. To address this problem, an understanding of the operational practices in a casthouse is important, as well as the underlying process of oxidation and dross formation. These topics will be discussed in detail in Chapter 4, which is entirely dedicated to dross formation.

Chapter 3 Oxidation at Laboratory Scale

The present chapter summarises the published work related to the parametric study of molten Al oxidation at the laboratory scale and the inhibiting effect of CO_2 on the rate of oxidation[76–79].

3.1 Summary of paper 1 – *Evaluation of the Effect of CO_2 Cover Gas on the Rate of Oxidation of an AlMgSi Alloy*

3.1.1 Introduction

The Mg content in the Al alloy and small additions of CO_2 in the cover gas has previously been reported to have an inhibiting effect on the rate of oxidation of AlMg alloys. Therefore, the present study aimed to investigate the impact of adding Si to the AlMg system and heat treating the alloy in different cover gases to investigate their effect on the rate of oxidation.

3.1.2 Experimental procedure

A master alloy with 6.77 wt.% Mg and 6.70 wt.% Si was tailored using an induction furnace. The Al (>99.999%, Alfa Aesar), Mg (>99.98%, Sigma Aldrich) and Si (>99.9999%, Wacker) particles were placed layer by layer in an Al_2O_3 crucible with a diameter of 45 mm and a height of 70 mm. The crucible was heated to 850°C and held at that temperature for 30 minutes to ensure homogenisation of the melt (isothermal step). A 5N (>99.999% pure) Ar atmosphere was applied during the heating-, isothermal-, and cooling steps when preparing the alloy. The Al sample was later retrieved from the crucible by crushing the crucible and grinding off the residues to ensure a clean sample. Following, the sample was cut into small discs with a diameter of 3-4 mm, and a thickness of 1-1.5 mm, sanded and polished using 1 μm of diamonds and stored in ethanol. Before the samples were analysed, the discs were removed from the ethanol and dried in air.

A DSC-TG instrument was used to monitor the mass change and heat flux as a function of time while heating the AlMgSi disc sample to 750°C and holding it at that temperature for 7 hours while being exposed to one of the following cover gases:

i. 80% synthetic air and 20% Ar,
ii. 99.999% Ar,
iii. 4% CO_2, 76% synthetic air and 20% Ar.

From here on, the three cover gases above will be referred to as synthetic air, Ar, and CO_2. To ensure reproducibility, three discs of the AlMgSi alloy were independently heat treated in the respective cover gases.

After the heat treatment, the surface morphology of the AlMgSi disc samples was investigated using Scanning Electron Microscope (SEM). The discs were also mounted in

epoxy resin, cut, and polished with 1 µm diamonds to map the cross-section using Electron Probe MicroAnalysis (EPMA). Furthermore, a Focused Ion Beam (FIB) was used to prepare lamella to evaluate the oxide layers and Energy Dispersive X-ray Spectroscopy (EDS) for elemental mapping.

3.1.3 Results and discussion

The DSC-TG measurements revealed a significant difference in the rate of oxidation for all three cover gases, and a comparison of the obtained mass change can be seen in Fig. 3.1 (a).

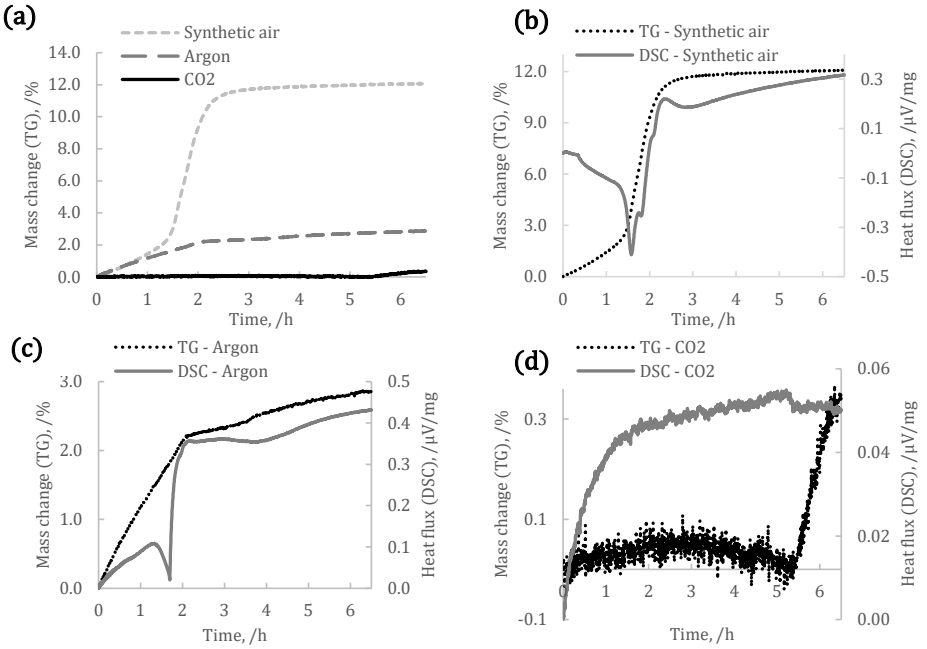

Fig. 3.1: Differential Scanning Calorimetry with Thermogravimetric Analysis (DSC-TG) results for AlMgSi disc samples heat treated at 750°C for 7 h. (a) TG result for disc samples heat treated in synthetic air (dotted grey graph), Ar (dashed grey graph), and 4% CO_2 (straight black graph). (b)-(d) The mass change (TG, dotted black graphs) and the heat flux (DSC, straight grey graphs) when heat treated in synthetic air, Ar, and 4% CO_2, respectively.

As can be seen from the figure, the mass decreased from 12.33% when heat treated in synthetic air (dotted grey graph) to 2.80% in Ar (dashed grey graph) and further down to 0.46% when 4% CO_2 was added to the cover gas (straight black graph). The heat flux identified for the synthetic air scenario (Fig. 3.1 (b)) also indicated that breakaway oxidation had occurred after ~1.5-2 h, having the classical S-shape for the mass gain as mentioned in section 2.2.3, where the oxidation of Mg and MgO occurred so quickly, that it was revealed as one mass gain step instead of two as reported by Haginoya *et al.*[50]. The oxidation rate also correlated well with the rates described by Jeurgens *et al.*[45]. This was further confirmed when looking at the cross-sectional area of the disc samples in Fig. 3.2 (a), as

well as the EPMA results presented in Fig. 3.3, where Al (a), O (d) and Mg (g) were all present in the oxide layer.

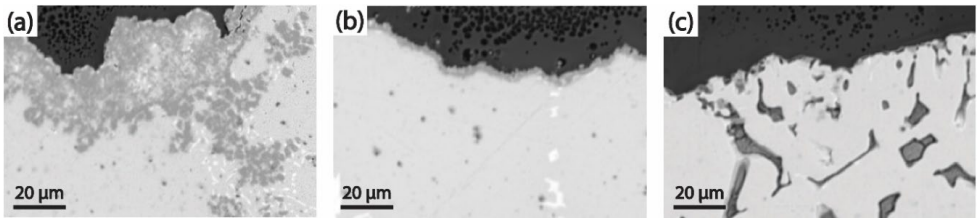

Fig. 3.2: Representative Scanning Electron Microscopy (SEM) images of the cross-section of oxidised AlMgSi disc samples after being heat treated in (a) synthetic air, (b) Ar, and (c) 4% CO_2. The dark grey/black area on the top of the disc samples is epoxy, the light grey is the Al bulk, and the grey layer in the middle of the epoxy and the Al in the bulk is the oxide.

Inhibition of the oxidation process for the AlMgSi alloy was confirmed when heat treated in pure Ar, which was further confirmed by the cross-sectional evaluation, as the oxide layer thickness had decreased significantly, see Fig. 3.2 (b). This was also confirmed by the EPMA results, see the middle column in Fig. 3.3. Even a thinner oxide layer was identified for the disc samples heat treated in the cover gas with 4% CO_2, but in this case, the cross-sectional investigations also identified a more porous structure, see the right column of Fig. 3.3.

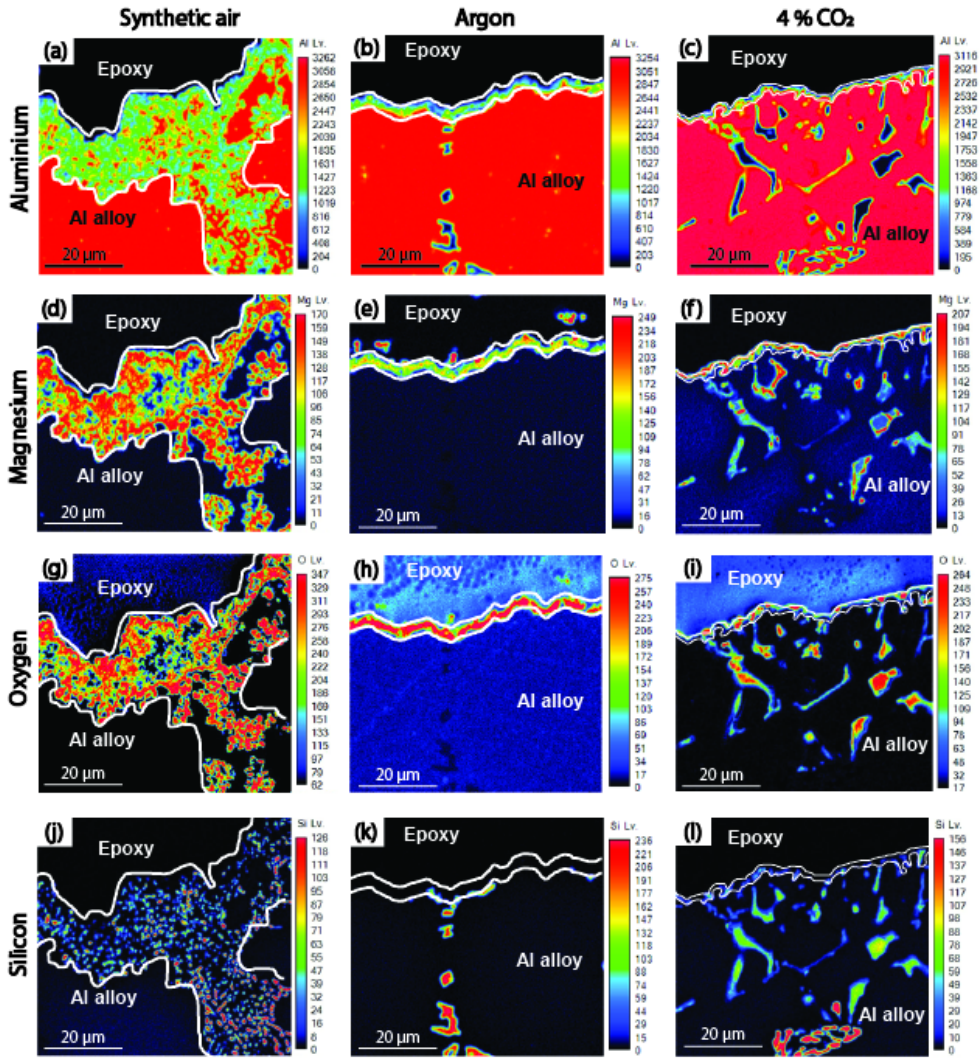

Fig. 3.3: Electron Probe Micro Analysis (EPMA) results of the cross-section of the AlMgSi disc samples presented in Fig. 3.2 after being heat treatment in the cover gases in question (x-axis) for the elements Al, Mg, O and Si (y-axis). The identified oxide layer can be seen between the epoxy and the Al alloy.

From the EDS analysis of the sample heat treated in 4% CO_2, depletion of Mg was revealed at the very top surface of the sample. Al, Mg, O and Si were all mapped by EDS, covering the lamella surface prepared by FIB, and it was observed that the sample surface was covered with a phase not containing Mg. It was, however, not possible to see from any of the analysis techniques applied, *i.e.*, EPMA, FIB and EDS, how the CO_2 had interacted/reacted with the AlMgSi alloy.

3.1.4 Conclusions and future work

It was concluded that additions of 4% CO_2 to the cover gas during heat treatment of an AlMgSi alloy influenced the oxidation rate of the material. By investigating the mass change and heat flux during heat treatment at 750°C, a dense oxide layer of 200-400 nm was identified, covering an additional ~2 µm thick granular oxide layer.

Future work will aim to identify how the Mg content in the Al alloy influences the oxidation rate of AlMg alloys when heat treated in the same three cover gases, *i.e.*, (i) synthetic air, (ii) Ar, and (iii) 4% CO_2. Further analysis will also be performed to identify how CO_2 influences the oxide layer characteristics to establish why CO_2 results in significant inhibition of the oxidation rate of these alloys.

3.2 Summary of paper 2 – *Influence of Mg Concentration on the Oxidation Rate of Al Alloys 5182 and 6016*

3.2.1 Introduction

A higher concentration of Mg in the Al alloy is known to enhance the oxidation rate, and CO_2 is reported to inhibit the oxidation rate, but it is unknown to what extent they influence the oxidation rate in view of a combination of those two parameters. The aim of the present study was, therefore, to investigate the inhibiting effect of small amounts of CO_2 in the cover gas when exposed to both the Al alloys 5182 (AlMg4.5Mn0.4) and 6016 (AlSi1.2Mg0.4), which is one alloy with higher and one with lower Mg concentration.

3.2.2 Experimental procedure

The disc samples investigated of the Al alloys 5182 and 6016 were supplied by Alcoa and used to calibrate the Optical Emission Spectroscopy (OES) apparatus in their casthouse. The chemical composition and trace element limits of these Al alloys can be seen in Tab. 3.1.

The present study followed the same experimental and analytical approach as in the case of the previous research by Solem *et al.*[76], see paragraph 3.1.2. In addition, the cross-sectional evaluation also included an EDS line scan analysis to investigate how the Al, O, Mg and C concentrations varied as a function of penetration depth through the oxide layers from the surface to the bulk.

Tab. 3.1: Chemical composition and trace element limits for Al alloys 5182 and 6016.

Alloy	Alloying elements, /wt.%							
	Al	Mg	Si	Mn	Fe	Cu	Cr	Ti
5182	Bal.	4.50-5.00	0.05-0.16	0.30-0.40	0.15-0.35	0.05-0.10	<0.03	<0.05
6016	Bal.	0.14-0.50	0.90-1.30	0.07-0.20	0.20-0.30	0.05-0.10	<0.05	<0.03

3.2.3 Results and discussion

The DSC-TG measurements of Al alloys 5182 and 6016 revealed similar behaviours as in the case of the AlMgSi alloy discussed in section 3.1.3. The mass gain decreased from 11.21% to -0.30% when adding 4% CO_2 to the cover gas of Al alloy 5182 and from 2.45% to 0.70% for Al alloy 6016, see Tab. 3.2.

Tab. 3.2: TG results from the DSC-TG measurements for Al alloy 5182 and 6016 heat treated in synthetic air, Ar and 4% CO_2.

Alloy	Mass change after being heat treated in		
	Synthetic air	Ar	4% CO_2
5182	11.21 wt.%	1.67 wt.%	-0.30 wt.%
6016	2.45 wt.%	1.61 wt.%	0.70 wt.%

The oxide layer thickness of the heat treated Al alloy 5182 followed a decreasing trend from 15-27 µm in synthetic air to only 200-400 nm in 4% CO_2, as seen in Tab. 3.3. This was not the case for the Al alloy 6016 as similar thicknesses of the oxide layers were obtained for the disc samples heat treated in synthetic air and 4% CO_2. Deviating from the trend, the thinnest oxide layer for the Al alloy 6016 was obtained when the disc samples were heat treated in Ar. This was, however, not the case for the Al alloy 5182 or the AlMgSi alloy discussed in section 3.1.

Tab. 3.3: Oxide layer thickness of the Al alloy discs heat treated in synthetic air, Ar and 4% CO_2.

Alloy	Oxide layer thickness after being heat treated in		
	Synthetic air	Ar	4% CO_2
5182	15-27 µm	14-17 µm	200-400 nm
6016	4-7 µm	~1-2 µm	3-5 µm

From the EPMA results, it was revealed that the cover gas had influenced the phases present in the oxide layer for the Al alloy 5182. It is believed that both oxidation and breakaway oxidation occurred when the disc samples were heat treated in synthetic air as the elemental mapping confirmed the presence of Al, Mg and O in the oxide layer, see left column of Fig. 3.4. Breakaway oxidation was, however, inhibited when the same alloy was heat treated in Ar, resulting in that only Mg and O was present in the oxide layer, see the mid-column of Fig. 3.4. For the disc samples heat treated in 4% CO_2 the dominating element present in the oxide layer was established to be Mg, see the right column in Fig. 3.4. Mg was also found to be present in the bulk, indicating that the oxidation of Mg had been hindered.

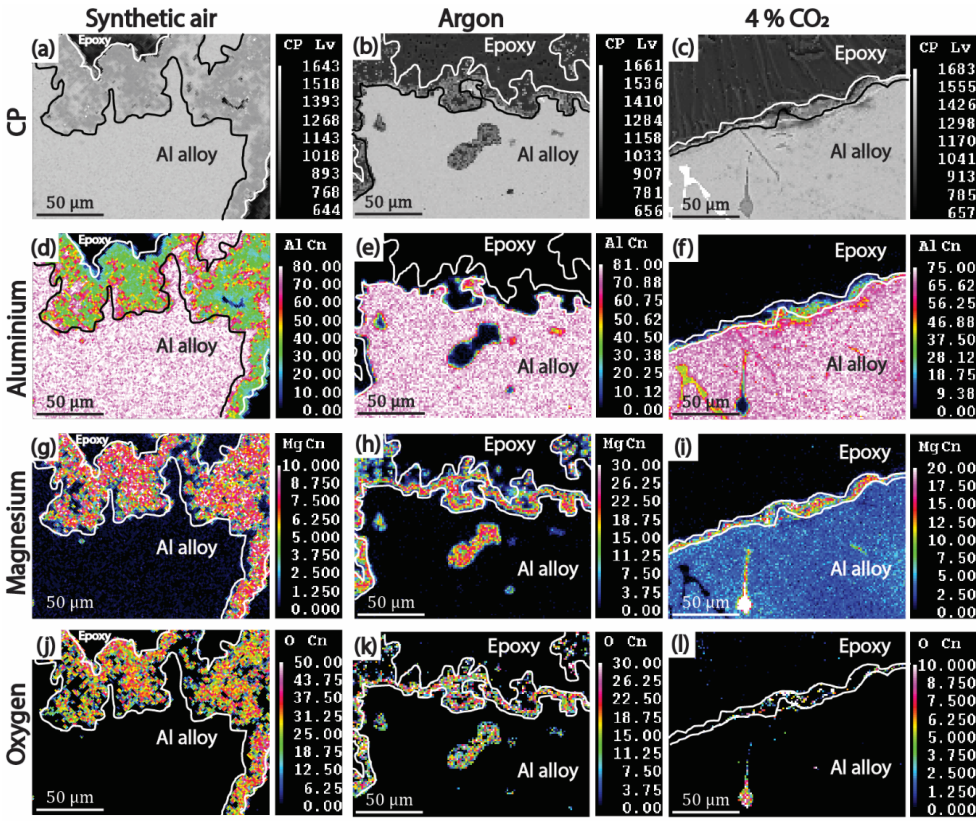

Fig. 3.4: EPMA results of the cross-sections of Al alloy 5182 after being heat treated in the cover gases in questions (x-axis) for the elements Al, Mg and O (y-axis). The layer between the epoxy and the Al alloy is the oxide layer, and CP images can be seen for each cross-section in (a) synthetic air, (b) Ar, and (c) 4% CO_2.

The EPMA results for the Al alloy 6016 revealed similar results for all three cover gases, as seen in Fig. 3.5, even though the TG results identified an apparent decrease in the mass gain when changing between the different cover gases. As seen from the figure, the Mg present in the alloy had diffused to the surface of the disc samples, leaving a bulk area depleted of Mg.

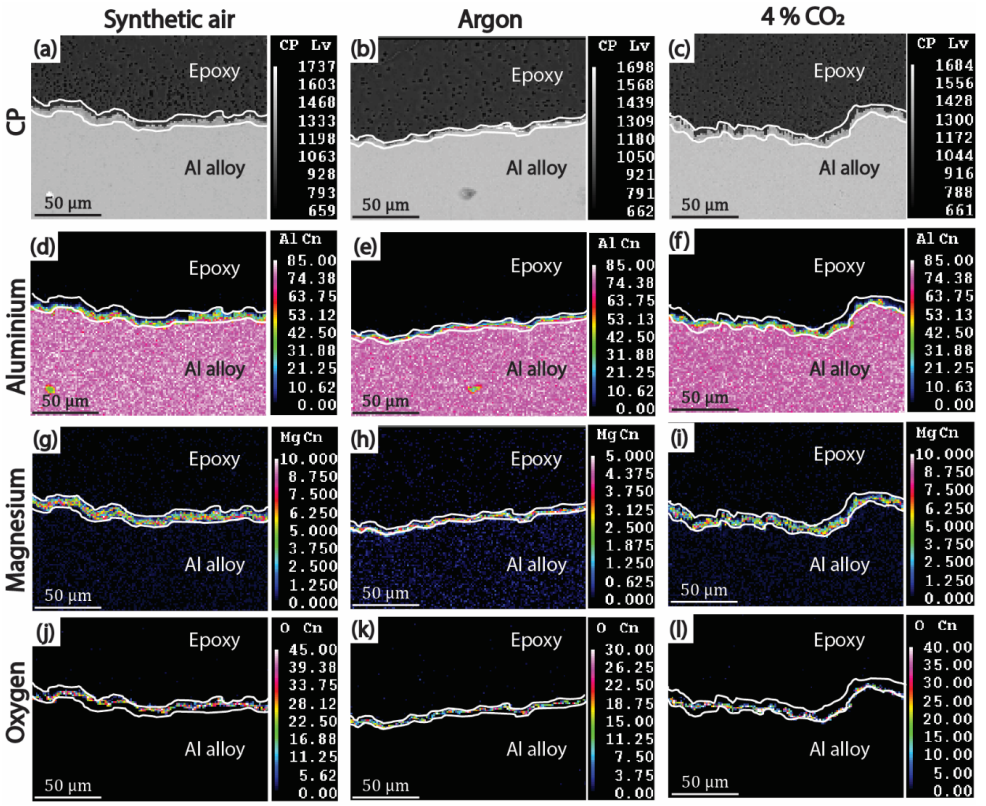

Fig. 3.5: EPMA results of the cross-sections of Al alloy 6016 after being heat treated in the cover gases in question (x-axis) for the elements Al, Mg and O (y-axis). The layer between the epoxy and the Al alloy is the oxide layer, and the CP images can be seen for each cross-section in (a) synthetic air, (b) Ar, and (c) 4% CO_2.

From the EDS line scans, it was, however, observed that a two-layered structure was obtained for the Al alloy 6016 disc samples heat treated in 4% CO_2, which is believed to explain why the oxide layer thickness seemed greater than when heat treated in Ar. The line scan of the same cross-section also revealed the presence of a string of particles close to the surface, as well as a layer of Al between the string of particles and the top surface. The two layers of Al and string of particles close to the surface created a total oxide layer thickness greater than the single string of particles for the sample heat treated in Ar, as these particles were identified as being at the very top surface of the oxidised disc samples.

3.2.4 Conclusions and future work

It was concluded that an addition of 4% CO_2 in the cover gas inhibits the rate of oxidation of both Al alloys 5182 and 6016. The mass gain for both Al alloys decreased when changing the cover gas from synthetic air to Ar and even further when adding 4% CO_2 to the cover gas.

A correlation between the Mg concentration and the oxide layer thickness was observed for the disc samples heat treated in synthetic air and Ar with the lower Mg concentration resulting in a thinner oxide layer. The morphology of the oxide layer for the disc samples heat treated in 4% CO_2 proved to change for both alloys, being a dense nanometer-thin continuous oxide layer for the Al alloy 5182 and a two-layered structure for the Al alloy 6016.

Future work will aim to identify how the added CO_2 in the cover gas interacts with the Al alloys 5182 and 6016, as well as how the oxidation rate is inhibited. The morphology of the oxide layer will be further investigated by analysing the disc samples heat treated in 4% CO_2 by Transmission Electron Microscopy (TEM).

3.3 Summary of paper 3 – *Heat Treatment of Mg-Containing Aluminum Alloys 5182 and 6016 in an Oxidizing Atmosphere with 4% CO_2*

3.3.1 Introduction

To identify the influence that the addition of 4% CO_2 to the cover gas had on the morphology of the oxide layers formed on Al alloys 5182 and 6016, respectively, further analysis was needed. XRD and TEM were therefore carried out on the relevant disc samples.

3.3.2 Experimental procedure

Disc samples of Al alloys 5182 and 6016 heat treated in synthetic air, Ar, and 4% CO_2 were analysed by XRD without any sample preparation. Some Al alloy 5182 disc samples, heat treated in 4% CO_2, were coated with a Pt-Pd coating using a FIB to improve the conductivity. This was not necessary for the Al alloy 6016 as the conductivity seemed sufficient without the Pt-Pd coating. Furthermore, both the Al alloys were exposed to a precursor gas with $C_{10}H_8$ (naphthalene) to ensure an adequate Z-contrast when analysed using a High Angle Annular Dark Field Scanning Transmission Electron Microscopy (HAADF STEM) unit.

3.3.3 Results and discussion

The HAADF STEM results for both the Al alloys 5182 and 6016 revealed a layer-by-layer structure from the bulk to the top surface of the disc samples heat treated in 4% CO_2, *i.e.*, an amorphous C-C layer was observed on top of a nanocrystalline MgO layer. It was believed that the naphthalene in the precursor gas made it possible to distinguish the amorphous C-C layer on top of the MgO layer from the C originating from the sample preparation step. Low Angle Annular Dark Field (LAADF) STEM images of the cross-section showing the layer-by-layer structure for both alloys are presented in Fig. 3.6. As can be seen from the figure, the MgO layer was thicker for the Al alloy 5182 than for the Al alloy 6016 with the lower concentration of Mg.

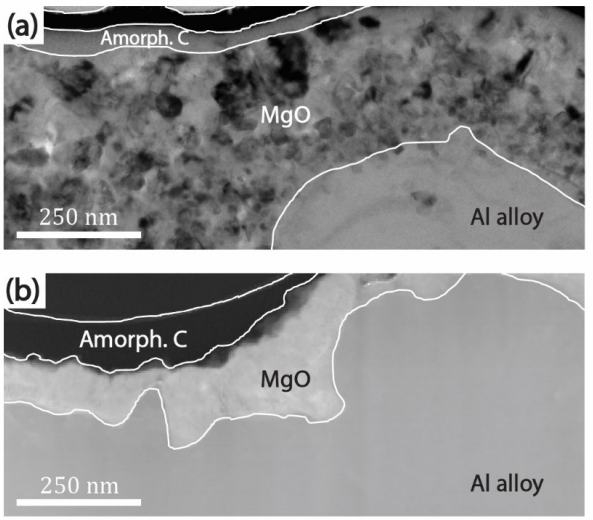

Fig. 3.6: Low Angle Annular Dark Field Scanning Transmission Electron Spectroscopy (LAADF STEM) image of the cross sections of disc samples heat treated in 4% CO_2. (a) Al alloy 5182 and (b) Al alloy 6016. An amorphous C layer can be seen on top of a MgO layer.

The XRD analysis of the Al alloy 5182 disc samples heat treated in synthetic air identified the presence of both MgO and $MgAl_2O_4$ in the top surface layer of the discs, indicating that breakaway oxidation had taken place. However, when analysing the disc samples heat treated in 4% CO_2, only the MgO phase was identified, which correlates well with earlier results based on microscopic analysis[77]. The TEM EDS Electron Energy Loss Spectroscopy (EELS) analysis also confirmed this observation, strengthening the theory that breakaway oxidation had been inhibited in the presence of CO_2.

For the Al alloy 6016 disc samples heat treated in synthetic air, the XRD analysis revealed that complete breakaway oxidation had occurred as no MgO was identified to exist. When heat treated in 4% CO_2, both MgO and $MgAl_2O_4$ were recognised by XRD and TEM EDS-EELS, indicating that breakaway oxidation had partly been inhibited. It is believed that the $MgAl_2O_4$ layer was formed as a discontinuous layer of 0.5-3 µm sized particles between the bulk and the MgO layer. It was, however, later also recognised as a continuous layer at the interphase between the MgO layer and the bulk, see Fig. 3.7.

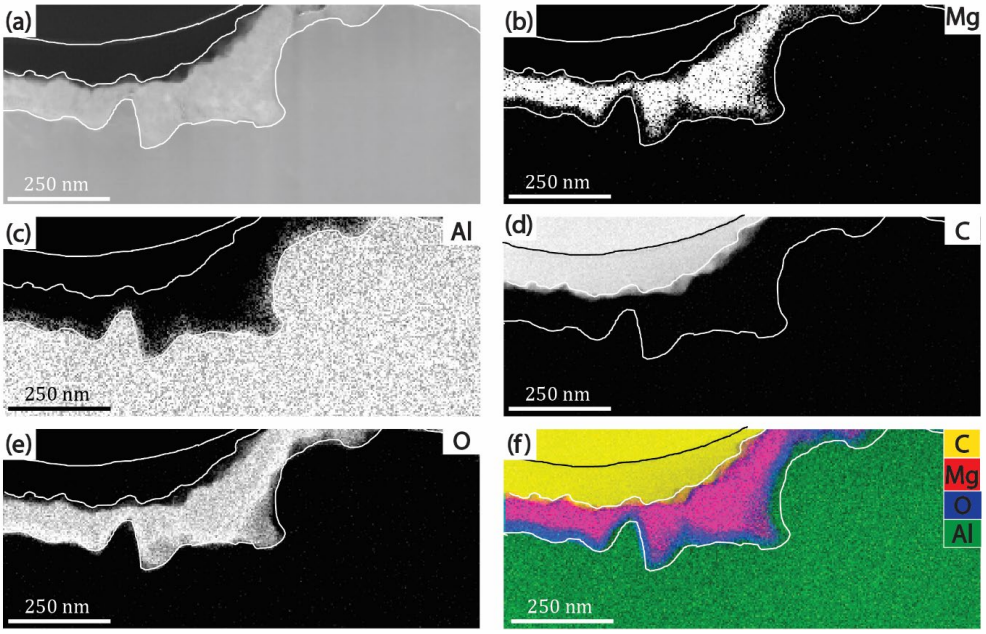

Fig. 3.7: LAADF STEM Energy X-ray Dispersive Spectroscopy (EDS) and Electron Energy Loss Spectroscopy (EELS) analysis of Fig. 3.6 (b), where (a) is an overview of the sample from the bulk to the top surface, (b) the presence of Mg, (c) the presence of Al, (d) the presence of C, (e) the presence of O, and (f) the presence of Mg, Al, C and O in the layer-by-layer structure.

3.3.4 Conclusions and future work

It was concluded that adding small amounts of CO_2 in the cover gas inhibited the oxidation rate for both Al alloys 5182 and 6016. An amorphous C-C layer was formed on top of a MgO layer, inhibiting further oxidation of Mg and breakaway oxidation of MgO. A clear layer-by-layer structure was revealed for both alloys, confirming the previous observations made by EPMA reported in section 3.2.

Future work will continue the TEM analysis of the Al alloy 6016. X-ray Photoelectron Spectroscopy (XPS) will also be carried out for both Al alloys 5182 and 6016 to facilitate the identification of C as a function of depth from the surface through the established layers.

3.4 Summary of paper 4 – *The Role of CO_2 on the Oxidation-Protection of Mg-Containing Aluminum Alloys*

3.4.1 Introduction

Additions of 4% CO_2 have proven to inhibit the oxidation rate of both Al alloys 5182 and 6016. An amorphous C-C layer has been established to exist, and it is believed that this layer inhibits the oxidation of Mg and the breakaway oxidation of MgO. However, how the presence of C influences this layer-by-layer structure has never been investigated. Therefore, the present study aimed to use XPS to identify how the C from the CO_2 inhibited the oxidation rate of these alloys.

3.4.2 Experimental procedure

The same disc samples as those produced in the study in section 3.3, *i.e.*, Al alloys 5182 and 6016 disc samples heat treated in 4% CO_2, were further analysed by XPS to investigate the binding energies of the elements at the very top of the oxide layers with a particular focus on C.

3.4.3 Results and discussion

The elements identified to exist by XRD and TEM EDS-EELS in the earlier study (section 3.3) for the disc samples heat treated in 4% CO_2 were also confirmed by XPS. High-resolution XPS depth profiling proved the presence of a C gradient that decreased from the top surface towards the bulk. The top surface peak for both alloys revealed binding energies for C-C and C-O, confirming the presence of a C-rich layer on the very top surface of both alloys.

The thickness of the MgO layer was established to be influenced by the Mg concentration in the Al alloy, as a higher Mg concentration resulted in a thicker MgO layer. Due to the high Mg concentration of Al alloy 5182, it was believed that breakaway oxidation was completely inhibited when adding 4% CO_2, but because of the low Mg concentrations of the Al alloy 6016, breakaway oxidation took place regardless of the presence of CO_2. However, it should be noted that breakaway oxidation was partly inhibited, confirmed by the presence of the MgO phase, which was not the case with the disc samples heat treated in synthetic air from the previous study discussed in section 3.3.3. It is therefore believed that the amorphous C-C layer inhibited the oxidation rate for both alloys, but to a slightly different degree due to the Mg concentration, forming an amorphous C-C layer according to Eq. 3.1, having a negative Gibbs Free Energy for all potential temperatures.

$$CO_2\,(g) + 2\,Mg\,(g) = 2\,MgO\,(s) + C\,(s) \qquad \text{Eq. 3.1}$$
$$\Delta G^0_{750°C} = -650.86\ kJ$$

3.4.4 Conclusions and future work

It is concluded that CO_2 plays a vital role in the inhibition process of the oxidation rate for both high and low Mg-containing Al alloys.

Further work will continue at an industrial scale to investigate if the inhibiting effect of CO_2 can be recognised during dross formation. A tool for collecting dross samples will be designed and used together with a step-by-step procedure for securing reproducible sampling of dross from different locations in the casthouse holding furnace. Both high and low Mg-containing Al alloys cooled in protective atmospheres will be investigated, aiming to reduce oxidation at an industrial scale, *i.e.*, dross formation.

Chapter 4 Dross Formation

Dross is classified as hazardous waste and originates from the production of Al either from the primary production route (white dross) or the secondary route (black dross). The chemical composition of the dross floating on top of the molten metal is a combination of oxidised Al and metallic Al entrained in the oxides, *i.e.*, a mass of solid impurities, where the ratio between the metallic Al and the oxides/NMCs contents varies depending on the production route[80–82].

4.1 Dross formation mechanism

As mentioned in section 2.4, dross is generated when liquid metal is in contact with the surrounding oxidising atmosphere. The mechanisms behind the dross formation are reported to be similar for both Al and AlMg alloys but result in different oxides[83]. For a pure Al melt, the formation of Al_2O_3 is the initiating dross formation step, and for an AlMg melt, it is a MgO oxide layer that is formed, as illustrated in Fig. 4.1[83].

Hiraki *et al.* studied *in-situ* dross formation during the melting of an AlMg10 alloy and documented the evolution of the oxide layer during heat treatment at 800°C[84]. The proposed mechanism was divided into three main steps: (i) a volume increase followed by a slow weight increase, (ii) a volume increase followed by a drastic weight increase, and (iii) a constant volume while the weight still increases[84].

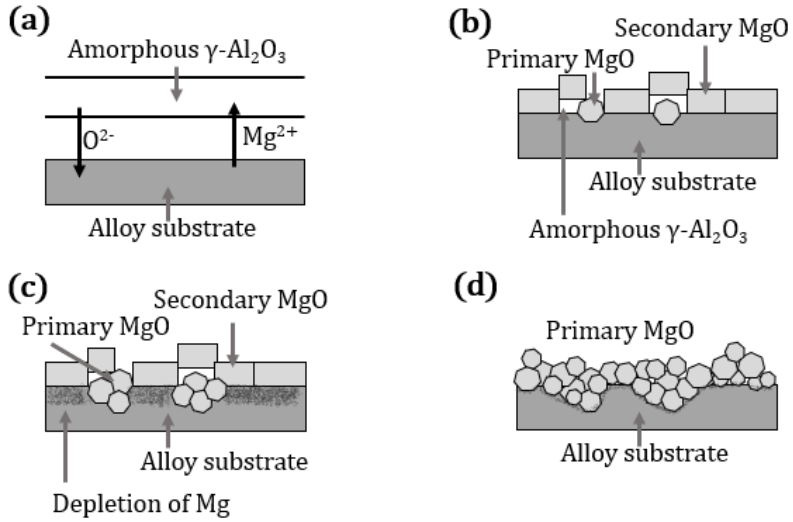

Fig. 4.1: Mechanism behind dross formation of an AlMg alloy, reproduced from Impey[83].

4.2 Dross types

4.2.1 White dross

The primary production of Al generates white Al dross as a waste stream during skimming of the melt just before casting, which results in a heterogeneous mixture of metallic Al, large flakes, lumps, smaller particles, and dust, as seen in Fig. 4.2.

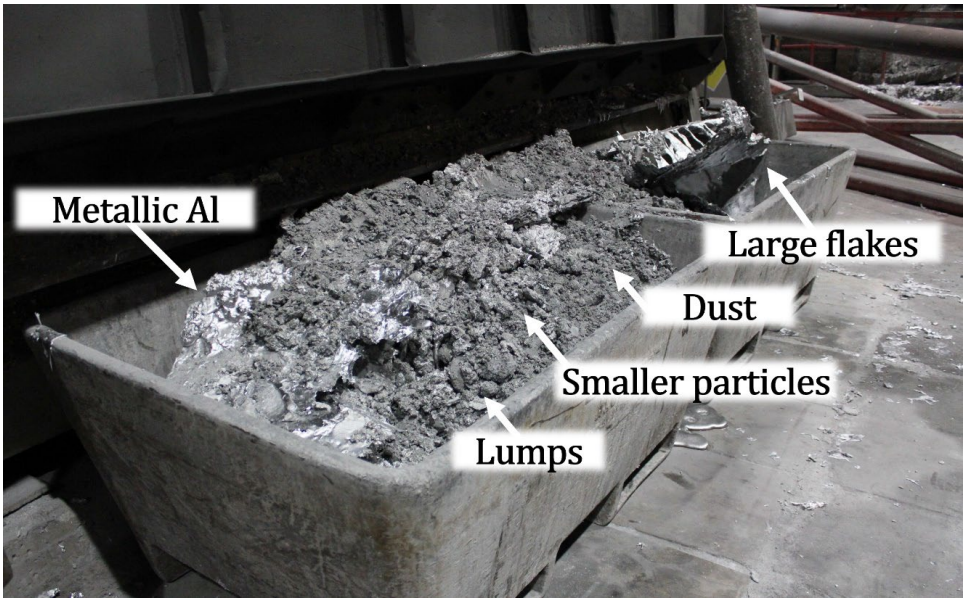

Fig. 4.2: Skimmed Al white dross collected in a dross bin at Alcoa. © 2019, Alcoa Mosjøen, Norway.

Skimming is one of the most critical steps when generating white dross[85]. In most cases, this is usually done manually by a furnace operator, as illustrated in Fig. 4.3, and the dross formation is influenced by the care taken by the operator while using a rake to collect and remove the oxide layer floating on top of the molten metal bath.

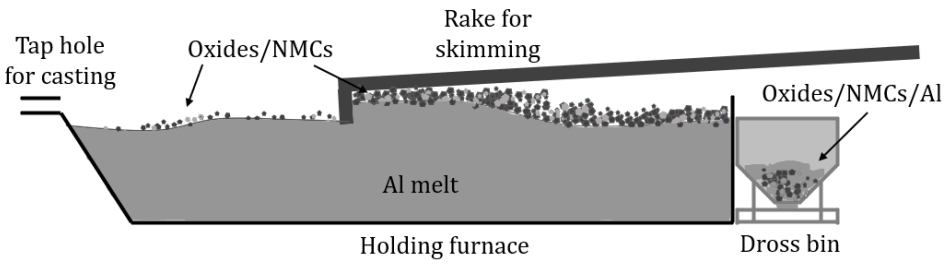

Fig. 4.3: Illustration of the skimming process, where floating oxides/NMCs are skimmed off by a rake and collected in a dross bin.

The white dross is also known as “wet dross” as it contains a high concentration of metallic Al giving the dross a “wet look”. The chemical composition of white dross does, however, vary, and the metallic Al concentration is reported to be <80 wt.% (see Tab. 4.1)[10, 85–90]. This is also why the white dross is of particular interest in view of dross recycling, as the potential recovery rate of the metallic Al is higher than for any other dross type.

Tab. 4.1: Various metallic Al content in white dross reported in the literature.

Metallic Al content in white dross	Reference
~50 wt.%	Drouet *et al.*[91]
30-70 wt.%	Kevorkijan[92]
55.70 wt.%	Capuzzi and Timelli[10]
74.08 wt.%	Meshram *et al.*[89]
15-80 wt.%	Peterson[85]

4.2.2 Black dross

Black dross, also known as “dry dross”, Fig. 4.4, originates from the secondary production route of Al, where it is generated by skimming the remelted EOL products and other post-consumed scrap before casting[80]. A typical chemical composition of black dross ranges from 10-20 wt.% metallic Al, 40-55 wt.% salt, and 20-50 wt.% Al_2O_3[93, 94]. The salt is added to reduce the concentration of Al_2O_3 as much as possible, enhancing the coalescence of the Al[80, 95].

Fig. 4.4: Black dross. © Aadli AS[96].

4.2.3 Salt cake

A salt cake is a waste from remelting dross when recovering the metallic Al[97]. The metallic Al content is even lower than for black dross and can be as low as 2-7 wt.%[10, 98]. It also contains up to 65 wt.% of other compounds, such as AlN, Al_2O_3, $MgAl_2O_4$, Al_4C_3, and up to 55% salts (NaCl, KCl)[87, 98, 99].

Fig. 4.5: Salt cake formed inside a rotary furnace. © International Mining 2022[100].

4.3 Casthouse furnace operations

The quality of the Al-based metal produced depends on several parameters, such as the furnace practice and temperature, which in turn will influence the turbulence in the molten metal bath. Even the surrounding atmosphere and location inside the holding furnace have proven to have an impact[101, 102].

The state-of-the-art furnace operations when preparing an Al melt for being cast typically include the following steps[103–105]:

- Cleaning the holding furnace for any previous melt.
- Adding cold in-house scrap.
- Preheating and melting in-house scrap.
- Pause.
- Adding primary produced Al from the electrolysis by injecting it from crucibles transporting the molten Al to the casthouse.
- Pause.
- Stirring of the melt.
- Skimming of the melt.
- Adding potentially other alloying elements.
- Control the melt's chemical composition by sampling two discs for testing the melt.
- Adjustments of the chemical composition if needed.
- Second stirring and skimming.
- Pause.
- Casting.

Mainly two different furnace practices are used today at the primary Al plants in Norway. The main difference is that in the first method, the melt is prepared in the same furnace as it is cast from, *i.e.*, one-furnace practice, and in the second method, the melt is transferred from the holding furnace to the casting furnace, *i.e.*, two-furnace practice.

4.3.1 One-furnace practice

The one-furnace practice operates with only one furnace, *i.e.*, all furnace operations are carried out in the same furnace (from melting in-house scrap to casting). The different steps are, therefore, more critical in view of the melt quality and the dross characteristics.

Transferring the primary produced Al from the electrolysis to the casthouse holding furnaces is one of the main steps, and pouring the melt from the crucible to the furnace contributes to the dross formation. As seen in Fig. 4.6, the metal is injected from the side of the furnace, and the height of the injected melt decreases as the holding furnace is filled up.

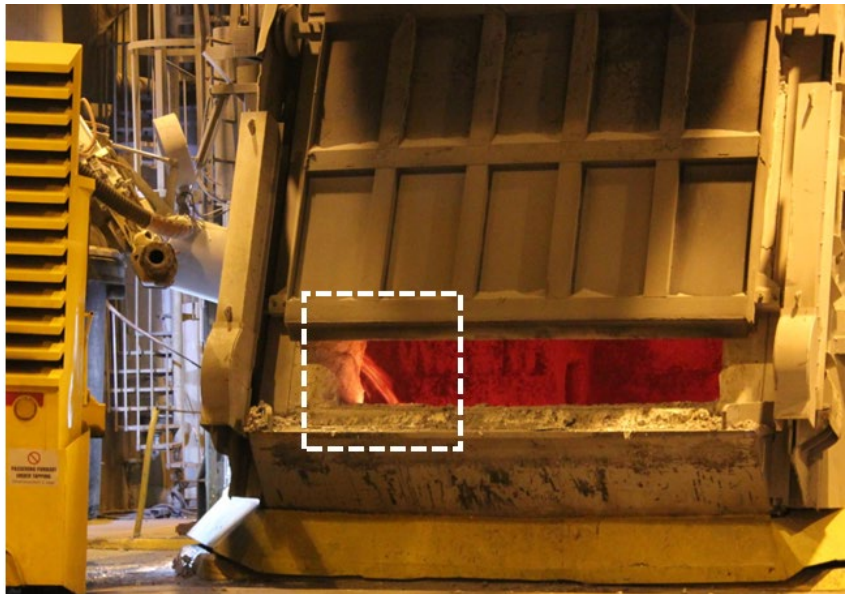

Fig. 4.6: Primary produced Al from the electrolysis poured into a casthouse holding furnace. © 2018, Hydro Karmøy, Norway.

It is impossible to avoid that this stream of injected Al breaks the oxide film on top of the hot pool of Al. The turbulence caused by the injected Al also enhances the dross formation[106]. The pouring height is largest at the beginning of the injection, and this is also causing the oxide film surface to break, allowing oxidation of the unreacted liquid Al to occur. It is also reported that the pouring height also results in air bubbles and other oxides/NMCs impurities being submerged in the bulk of the molten melt[75]. Dross rings, *i.e.*, rings formed in the melt caused by the injection of the primary produced metal, is also

a result of the injection of the primary produced Al and contributes to dross formation, as the injection of liquid Al contributes to entrain oxides and air in the melt, see Fig. 4.7. Moreover, the steps listed above in section 4.3 are carried out in the same holding furnace.

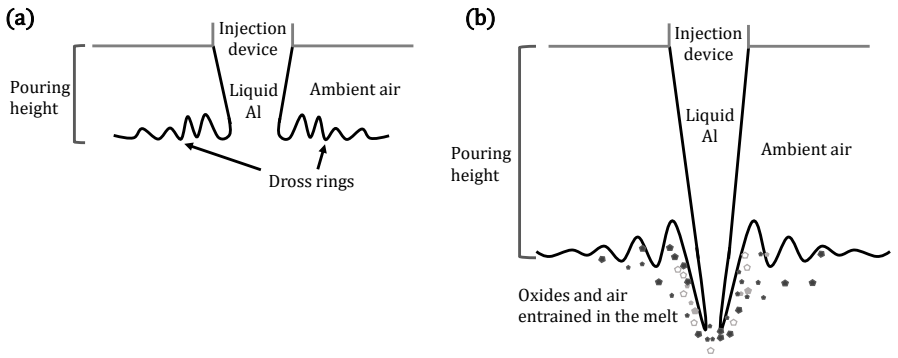

Fig. 4.7: Injection of primary produced Al to the casthouse holding furnace causing (a) dross rings and (b) entrained oxides and air into the melt due to the pouring height. Reproduced from © 1991, 2003, Elsevier Science Ltd., J. Campbell[75].

4.3.2 Two-furnace practice

When operating with two-furnace practice, the same preparation steps are carried out as for the one-furnace practice until the first skimming step. After the skimming step, the melt is transferred to a holding furnace through the tap hole at the centre back of the furnace. The melt is then injected from the first furnace's tap hole into the second furnace's tap hole. Halfway through the transfer, the additions of Mg are added to the second furnace before continuing the transfer to avoid increased concentrations of Na and Ca in the melt, originating from the bath in the pot lines where cryolite is used[107].

4.4 Dross recycling

Dross processing is essential in the Al production cycle, as the dross contains elemental Al metal. In Fig. 4.8 a flow sheet of typical dross processing methods is presented for white and black dross. As seen from the flow sheet, regardless of which dross and processing method, there will always be some waste/residues[108].

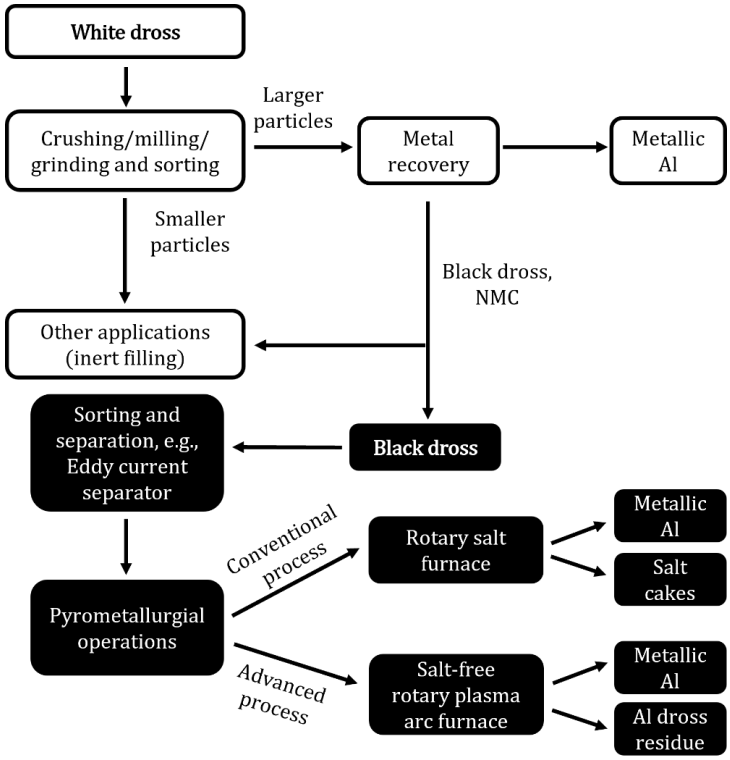

Fig. 4.8: Typical Al dross processing methods for white and black dross. Reproduced from © 2017 Elsevier B.V., Meshram and Singh[108].

In 2017, the worldwide dross generation was about 3 million tonnes, including the downstream activities, *e.g.*, cut-off residues from the forming, recycling, and primary Al sectors, see Fig. 4.9.

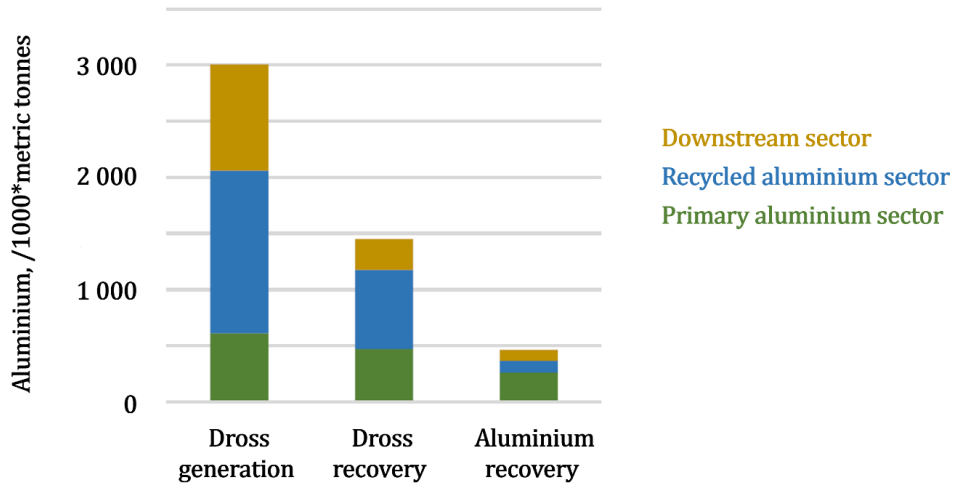

Fig. 4.9: Worldwide dross generation, dross recovery and overall Al recovery based on numbers from 2017[20].

From Fig. 4.9, it can be seen that it is the primary produced Al that has the highest metallic Al recovery rate[20]. The white dross has, over the years, had several treatment operations, both in-house at the plant and out-house at external treatment facilities. Some of these approaches will be discussed below in the coming sections.

4.4.1 In-house - floor cooling

One approach has been to reduce the dross formation by decreasing the temperature of the dross as quickly as possible, reaching low enough temperatures to hinder further oxidation. By doing so, the heat and energy in the dross itself would not contribute to oxidising the metallic Al entrained within the dross any further. It was, however, not found efficient as it required a large area for distribution of the dross on the floor[32]. Due to the gases generated during cooling, it was also not desirable to have the dross on the floor inside. As reactions between the dross and potential rain/water would allow the generation of the gases even quicker, distributing the dross outside was not found to be a viable alternative.

4.4.2 In-house - Ar covers

In the 1970s, a cover was suggested to prevent the oxygen from reacting with the glowing hot dross surface[109]. The approach was further developed, and today there are inert dross cooling apparatuses available in several casthouses. The dross bins with the skimmed-off dross are placed under heavy steel covers purged with Ar to inhibit the oxidation of the remaining metallic Al entrained in the white dross[17, 110, 111], see Fig. 4.10.

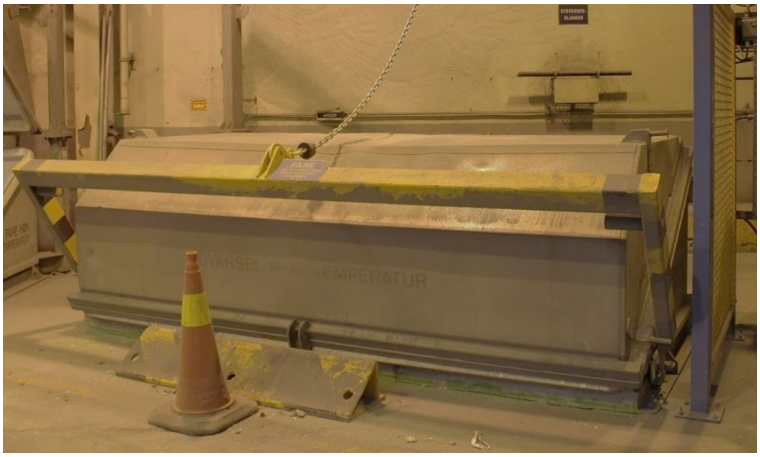

Fig. 4.10: Ar cover protection during cooling of skimmed-off dross at Hydro. © 2018 Hydro Karmøy, Norway.

4.4.3 In-house - dross pressing

After skimming the melt into specially designed dross bins in front of the holding furnace, the bins are moved to a dross press. The press instrument applies pressure from above, using the dross bin as a counterpart, pressing out as much metallic Al as possible while the metallic Al is still molten/soft[112]. The metallic Al is then pressed through holes in the bottom of the dross bin and recovered before the remaining dross is shipped off for external treatment[111].

Fig. 4.11: Dross press with the metallic Al collected under the dross bin after the white dross has been pressed. © ALTEK[113].

4.4.4 Out-house - re-melting

All primary Al plants in Norway ship off their dross to an external treatment facility, *e.g.*, Real Alloy, where the dross is re-melted. Salts and other fluxes are added to hinder further oxidation of the metallic Al, as well as some of the Al that has already oxidised.

The conventional process of re-melting uses a rotary salt furnace, where the dross and salts (~50% of the weight of the dross) are fed into the furnace[15]. The salt floats on top of the molten metal and hinders the metal from being in contact with the oxidising atmosphere, as well as extracts the metal and agglomerates the oxides and salts into a salt cake on top of the melt[15].

One of the more advanced processes is using a plasma arc furnace, which is a salt-free process. The salt-free process prevents the unwanted salt cake from forming but is left with other residues that might end up as landfill[97, 114].

4.5 Commercial application of Al dross

There are several suggestions for different applications where Al dross is used with the aim of utilising the waste. Soós *et al.*[115] experimentally tested using Al dross as a filler when producing asphalt, replacing the limestone ($CaCO_3$), which gave promising results. Li *et al.*[116] investigated the use of Al dross as a component to produce lightweight concrete, which revealed that a lower density concrete was obtained following a reaction between the dross and OH^- generating H_2 bubbles in the material. Other studies on Al dross incorporated in concrete and cement have also given promising results resulting in higher stiffness of the product[117, 118].

Generation of different gases, *e.g.*, H_2, NH_3 and CH_4, can also be a result when the dross is in contact with water, as these are all exothermic reactions[108]. A novel utilisation process also studies the use of Al dross as a reductant to produce Si alloys[119, 120].

Another application for Al dross is in the production of calcined alumina by mixing limestone and non-metallic residues from the dross, forming a calcium aluminate ($CaAl_2O_4$) phase suitable to use as a reductant for the iron and steel industry[121].

There are, in other words, many applications for the dross to be utilised within, however, it is important not to justify the generation of the waste when looking at the downsides and consequences of dross generation.

4.6 Environmental and economic benefits from dross recycling

In 2009 it was estimated that about 1.1% of the greenhouse gases (GHG) on a global level were caused by the Al industry. The most significant contribution to GHG originates from

the electrolysis and the Hall-Hèroult process, however, to lower the Al industry's emissions, there is a need to evaluate all contributions.

The emissions related to dross formation are directly correlated to the metallic Al losses and the transportation of the dross material for further treatment (recycling). As the dross is to be treated at an external treatment facility, the CO_2 emissions from transport to the facility and back can be a substantial contribution that must be considered.

Decreasing the masses sent to landfills is also an environmental and economic benefit resulting from dross recycling. It is also essential to remember that metals, in general, are not renewable materials as natural resources and that recycling is the most important tool used to prolong the lifetime of such resources[122].

From a Circular Economy (CE) scenario, Van der Voet *et al.*[9] predicted the GHG emissions from the Al industry based on the Al supply given in section 1.1. Based on this, the primary production will peak around 2050, followed by a decrease as the demand for primary produced Al decreases. First, by 2100, the GHG emissions will be lower than today[9].

The economic benefits of reducing the dross formation are linked to the metallic Al yield profits. An increased metallic Al yield in-house, reducing the waste and side-streams, will add a significant (<10%) contribution to the annual production[11]. Transportation costs will also decrease with decreasing out-house waste, influencing CO_2 emissions and, hence, the carbon tax, *i.e.*, a tax set by the government, which is the price that emitters must pay for each tonne of GHG emissions emitted. Norway, together with the other Nordic countries, was the first to introduce a carbon tax in the early 1990s, trying to reduce CO_2 and other fossil fuel-related emissions and limit global warming[123].

The benefits of reducing the dross formation are today motivated by increasing the profit and reducing the GHGs and CO_2 and other emissions globally[124]. To face these challenges, it is believed that all contributions can make a difference and, in the long run, reduce the negative environmental impact caused by the industry.

Chapter 5 Dross Formation at Industrial Scale

5.1 Summary of paper 5 – *Sampling Procedure, Characterization, and Quantitative Analysis of Industrial Al White Dross*

5.1.1 Introduction

As white dross is a heterogeneous mixture of metallic Al, oxides/NMCs, large flakes, smaller particles, lumps, and dust, collecting representative Al dross samples is challenging. Not only is the physical appearance of the dross varying from charge to charge, but the metallic Al concentration in the dross has also been reported to range from 40 wt.% to >75%[85, 90].

Several parameters will influence the dross formation, such as the chemical composition of the melt, the furnace practice and operations, as well as the location inside the holding furnace[104]. Numerous studies report on the characterisation of dross morphologies, but it is unclear where the dross originates from or how the dross has been collected. Therefore, the present study aimed to design, develop, and validate a sampling tool, as well as a step-by-step sampling procedure for collecting, pulverising and analysing representative dross samples directly from the holding furnace in the casthouse.

5.1.2 Experimental procedure

A sampling tool was designed and made of a stainless steel sieve with holes having a diameter of ¼ inch (6.35 mm) and a perforation of 33%. The sieve was connected to a 2-meter-long handle to allow the dross to be reached directly from the furnace gate.

The Al melt was prepared following standard furnace operation before the sampling of the dross was carried out between the injection of the primary produced Al and the first skimming session. The sampling tool was flipped and submerged into the melt, breaking the initial dross layer floating on top of the melt. When the sieve was completely submerged into the melt, the sieve was flipped back and raised, collecting the floating oxides/NMCs. Before transferring the dross from the sieve to the tray for cooling, the sieve was gently shaken three times horizontally and vertically to drain off as much excess metallic Al entrained in the dross as possible. This procedure was repeated for four different locations inside the holding furnace, see Fig. 5.1. The collected dross samples were left to cool in the ambient air of the casthouse, as seen in Fig. 5.2, for one hour before being stored in air-sealed containers.

All the collected dross samples secured from the different locations were sieved into the three fractions <1.25 mm, 1.25-4.5 mm and >4.5 mm, and the two smallest fractions were further milled and quantitatively analysed by XRD.

Fig. 5.1: Collection of dross samples from Location 1 (closest to the injection point of the primary produced Al) to Location 4 (furthest away) in the holding furnace using the 2-meter-long dross sampling tool. © 2019, Hydro Karmøy, Norway.

Fig. 5.2: Collected dross samples left to cool in the ambient air of the casthouse from Location 1 to Location 4.

5.1.3 Results and discussion

The sampling tool proved efficient in collecting dross samples, but even with a 2-meter-long handle, it was challenging to reach the floating oxides/NMCs from Location 1 to Location 4. An adjustment to the furnace operation was therefore made, and a step was added where the casthouse operator carefully skimmed the floating oxides/NMCs towards the furnace gate without mixing it up, as seen in Fig. 5.3. The sampling procedure was then followed as previously presented.

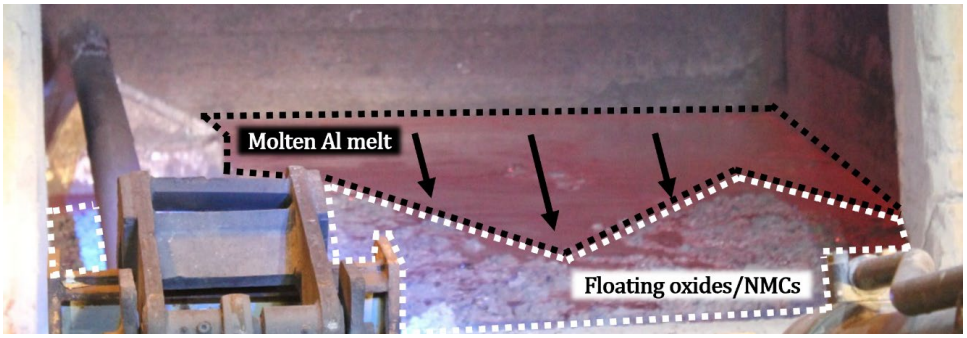

Fig. 5.3: Floating oxides/NMCs carefully skimmed towards the furnace gate for dross sampling. © 2018, Hydro Karmøy, Norway.

The sampling tool and procedure were validated by quantitatively characterising the dross morphology of the samples collected from the different locations. The smallest fraction (<1.25 mm) was pulverised using a ring mill, but the same technique was observed not to be successful in pulverising the mid fraction (1.25-4.5 mm), leaving the softer metallic Al particles deformed but not pulverised. Cryomilling was, therefore, introduced to make the metallic Al particles in the samples brittle enough to be crushed rather than only deformed. By cryomilling, aiming for a temperature of -196 °C using liquid N_2, it was seen that the method was successful in pulverising all the different parts of the dross.

The XRD analysis revealed that reproducible samples had been collected from the different locations in the holding furnace. Furthermore, Location 1 was established to have the highest metallic Al concentration and the lowest oxides/NMCs content, and in view of Location 2, Location 3 and Location 4, the metallic Al concentration gradually decreased while the oxides/NMCs content increased.

Collecting dross samples from several different Al melts showing the same sample characteristics from Location 1 to Location 4 (independently of the Al alloy or charged analysed) proved that the sampling tool and sampling procedure were an efficient way of collecting reproducible dross samples for further pulverisation and analyses.

5.1.4 Conclusions and future work

It was concluded that a sampling tool and a step-by-step sampling procedure had successfully been designed and developed, making it possible to secure reproducible dross samples despite the heterogeneity of the dross. Combined with suitable pulverisation and characterisation techniques, the approach can quantify the metallic Al concentration and the oxides/NMCs content present in the dross.

As it has been reported that small amounts of CO_2 have an inhibiting effect on the oxidation rate at a laboratory scale, it would be interesting to see if the same effect can be seen at an industrial scale. Future work will therefore aim to develop a set-up that allows for protective cooling of collected dross samples using a cover gas containing >5% CO_2 to investigate if the influence of CO_2 in the cooling atmosphere of the dross has an impact on the oxidation rate of AlMg alloys.

5.2 Summary of paper 6 – *Effect of (5%) CO_2 on the Oxidation Rate during Cooling of Industrial Aluminum White Dross*

5.2.1 Introduction

Small amounts of CO_2 have proven to inhibit the oxidation rate of AlMg alloys. It has also been reported in the literature that adding >4% CO_2 to an oxidising atmosphere significantly decreases the mass gain for Al alloys with as low as 0.4 wt.% Mg. However, the same inhibiting effect has not yet been seen on an industrial scale. Therefore, the present work aimed to investigate if adding small amounts of CO_2 in the atmosphere during cooling of the

skimmed dross would have the same inhibiting effect on the oxidation rate and thereby increase the metallic Al content of the dross.

5.2.2 Experimental procedure

To investigate the influence of CO_2 exposure during the cooling of the dross, a lid was designed that was connected to a premixed gas of 95% synthetic air and 5% CO_2 (the lowest CO_2 concentration available as a premixed gas). Individual lids were used to cover the dross trays. The complete set-up can be seen in Fig. 5.4, where the gas tubes are secured in an open cage connected to the lids by gas tubes.

The same sampling tool and procedure presented in section 5.1 were applied to collect the dross samples from Charge 1 (AlMg1.0Mn0.4) and Charge 2 (AlMg1.2Mn0.4). Two dross samples were collected at the same place from each location, *i.e.*, from Locations 1-4, where the first collected sample was transferred to a dross tray left to cool in ambient air, see the blue area in Fig. 5.4 and the second to another dross tray which was placed under a lid with protective atmosphere, see the red area in Fig. 5.4. All samples were left to cool for one hour and sieved into the same three fractions as in the earlier study, *i.e.*, <1.25 mm, 1.25-4.5 mm and >4.5 mm.

The samples from Charge 1, Location 1 to Location 4 for fractions <1.25 mm and 1.25-4.5 mm were cryomilled and analysed by XRD. From Charge 1 and Charge 2, Location 1 to Location 4, eight randomly selected dross pieces from the fractions 1.25-4.5 mm and >4.5 mm were mounted in epoxy and analysed by EPMA. The EPMA images were further quantified by deterministic image analysis.

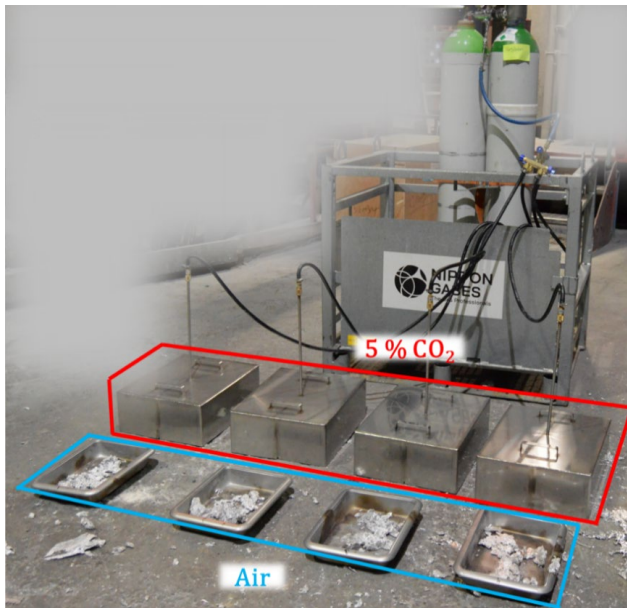

Fig. 5.4: Collected Al white dross samples, where one series of samples are cooled in ambient air and the second under a lid exposed to a cover gas with 5% CO_2.

5.2.3 Results and discussion

All dross samples analysed by XRD revealed a higher metallic Al concentration for the samples cooled under a lid exposed to a cover gas with 5% CO_2 than when cooled in ambient air. The XRD results also revealed that the metallic Al concentration was highest for Location 1 (closest to the injection point of primary produced Al) and lowest for Location 4 (furthest away). Simultaneously, a decreasing trend for the oxides/NMCs contents was also observed from Location 1 to Location 4. As seen from Tab. 5.1, this was the case for both the analysed fractions and for both series of samples, *i.e.*, for those cooled in ambient air and for those cooled under a protective atmosphere under a lid.

Tab. 5.1: XRD results for Charge 1, fractions <1.25 mm and 1.25-4.5 mm, Location 1 and Location 4 when cooled in ambient air and under a lid exposed to a cover gas with 5% CO_2.

	Fraction	Cooling atmosphere	Content, /wt.%	
			Location 1	Location 4
Metallic Al	<1.25 mm	Ambient air	73.8	70.9
		5% CO_2	78.5	72.5
	1.25-4.5 mm	Ambient air	88.5	81.5
		5% CO_2	91.2	82.4
Oxides/NMCs	<1.25 mm	Ambient air	26.2	29.2
		5% CO_2	21.5	27.5
	1.25-4.5 mm	Ambient air	8.8	17.7
		5% CO_2	11.5	18.5

From the EPMA and deterministic image analysis, it was revealed that the metallic Al concentration for the samples cooled in ambient air was 86.0 wt.%, while when cooled under a lid exposed to a cover gas with 5% CO_2, it had increased to 89.4 wt.% metallic Al. Even though an average (including both charges, fractions, and locations) followed the same trend as seen from the XRD results, the same decreasing trend from Location 1 to Location 4 for the metallic Al concentrations was not seen. This is believed to be due to the limited number of samples analysed by deterministic image analysis. A higher number of images is believed to have given a more accurate result.

5.2.4 Conclusions and future work

Based on the obtained results, it was concluded that adding 5% CO_2 to the cover gas during the cooling of the dross had an inhibiting effect on the oxidation rate of AlMg alloys. The overall metallic Al concentration in the dross was higher for the samples protectively cooled under a lid than in the ambient casthouse air for both charges. The obtained XRD results were confirmed by EPMA and deterministic image analysis.

Future work will include continuing the industrial campaigns by implementing the sampling tool and procedure during normal operational conditions. Different concentrations of CO_2 mixed with synthetic air would also be of interest. The dross samples will also be investigated by TEM to see if the amorphous C-C layer is present even in the case of the industrial dross samples.

Chapter 6 Summary and Conclusions

The main focus of the present study has been to systematically investigate the oxidation of Al white dross collected from the holding furnace during casthouse operations. The impact of different process parameters on the oxidation rate of AlMg and AlMgSi alloys was first studied at a laboratory scale before implementing the experimental conditions at an industrial scale during normal process conditions. Special emphasis was put on identifying the parameters that inhibit the oxidation rate and thereby the formation of Al dross.

Based on the results from the laboratory work, it was concluded that additions of 4% CO_2 in an oxidising atmosphere significantly impacted the oxidation rate of both the AlMg and AlMgSi alloys. This was also seen for both low- and high Mg-containing Al alloys, but to a lesser extent for the low Mg-containing alloys. The small amount of CO_2 in the atmosphere proved to form a protective amorphous C-C layer on top of a MgO layer and prevented further evaporation of Mg from the thermally treated sample surface, as well as the diffusion of O_2 into the bulk of the sample. From the obtained results, it was concluded that inhibition of the oxidation rate of Mg and Al had taken place at a constant temperature of 750°C.

Several industrial campaigns were planned and carried out during the production of different AlMg alloys. A sampling tool for collecting reproducible samples from the holding furnaces in the casthouse was successfully designed, developed, and validated, together with procedures for sample collection and powder preparation for analysis. This allowed the heterogenous dross to be crushed into fine powders that were later analysed through chemical analyses and phase identification. Cryomilling was used to pulverise the collected dross samples and XRD for performing the quantitative analyses. EPMA and a novel deterministic image analysis method were also used to complement and verify the XRD results. It was concluded that the furnace practice, as well as the location inside the holding furnace, from where the dross samples were collected, had an impact on the dross characteristics. It was also established that protective cooling by adding 5% CO_2 to the cover gas had an apparent inhibiting effect on the oxidation of the skimmed dross. It was concluded that the results from the laboratory-scale oxidation trials could be reproduced at an industrial scale during normal process operations, verifying the influence that small amounts of CO_2 had an inhibiting effect on the oxidation rate of Mg and Al.

The designed dross collection tool and procedures, together with recommendations in view of successfully pulverising and analysing dross samples, are believed to give the industry improved possibilities to control the generation of Al dross through identifying specific parameters to be used to increase their total metallic Al yield.

Chapter 7 Future Work

There is still a lack of knowledge related to understanding the mechanisms behind the impact of small amounts of CO_2 in the cover gas on the rate of oxidation of Al white dross. The formation of an amorphous C-C layer, which in the present work has proved to take place and to have an inhibiting effect on the formation of dross, will also need to be studied in more detail to clarify the driving force for its initiation, formation, and further growth. Therefore, a comprehensive study of the different reactions and the system's overall stability is needed. The influence of variations in processing temperature should also be investigated, as well as the impact of the Mg concentration.

7.1 Future work at a global perspective

The conventional process for primary production of Al was already revolutionised 25 years ago by replacing the Sødeberg technology with pre-baked anodes[125], decreasing the direct current pr kg Al produced by ~ 30%. For further progressions in the field, it is, however, important that the industry does not settle with the solutions introduced 10-20 years ago.

Dross formation is one of the essential environmental concerns within the global Al market today, and it is believed that an improved understanding of dross initiation, formation and growth will enable the Al industry not only to maximise the metallic Al yield during production but also during dross recycling. By fully understanding how to inhibit dross formation during production, it will give the Al industry the best prospects to reach the zero-waste scenario through the optimisation of process operations, as well as by the design of new sustainable production methods for the recovery of Al from dross.

As already pointed out, there is an industrial need to keep moving forward. In view of this, an immerging question is: *"Can CO_2 go from being a waste to a solution for inhibiting dross formation in the future?"*.

Today, it exists several dross treatment processes, and they are continuously being improved, trying to reduce the amount of waste sent to be landfilled (which still is the conventional way of handling the dross in the greater part of the world), but as expressed by Clarence J. Moser[99]:

> *"I feel that no matter how sophisticated we become in the handling of drosses, we cannot lose sight of the fact that if the dross were not generated, to begin with, later processing would not be required."*

In other words, even if it has taken years for the global Al industry to get to where they are today, gaining a deeper understanding of what needs to be done and how is believed to be in sight.

References

1. Tangstad M (2013) Metal production in Norway. Akademika Publ, Oslo

2. Schlesinger ME (2013) Aluminum Recycling, Second Edition. CRC Press

3. Sverdrup HU, Ragnarsdottir KV, Koca D (2015) Aluminium for the Future: Modelling the Global Production, Market Supply, Demand, Price and Long Term Development of the Global Reserves. Resources, Conservation and Recycling 103:139–154. https://doi.org/10.1016/j.resconrec.2015.06.008

4. Mahinroosta M, Allahverdi A (2018) Hazardous Aluminum Dross Characterization and Recycling Strategies: A Critical Review. Journal of Environmental Management 223:452–468. https://doi.org/10.1016/j.jenvman.2018.06.068

5. Cullen JM, Allwood JM (2013) Mapping the Global Flow of Aluminum: From Liquid Aluminum to End-Use Goods. Environ Sci Technol 47:3057–3064. https://doi.org/10.1021/es304256s

6. Saevarsdottir G, Kvande H, Welch BJ (2020) Reducing the Carbon Footprint: Aluminium Smelting with Changing Energy Systems and the Risk of Carbon Leakage. In: Tomsett A (ed) Light Metals 2020. Springer International Publishing, Cham, pp 726–734

7. Liu G, Bangs CE, Müller DB (2013) Stock Dynamics and Emission Pathways of the Global Aluminium Cycle. Nature Climate Change 3:338–342. https://doi.org/10.1038/nclimate1698

8. He S, Zhang D, Zhang X, et al (2021) Rechargeable Al-Chalcogen Batteries: Status, Challenges, and Perspectives. Advanced Energy Materials 11:2100769. https://doi.org/10.1002/aenm.202100769

9. Van der Voet E, Van Oers L, Verboon M, Kuipers K (2019) Environmental Implications of Future Demand Scenarios for Metals: Methodology and Application to the Case of Seven Major Metals. Journal of Industrial Ecology 23:141–155. https://doi.org/10.1111/jiec.12722

10. Capuzzi S, Timelli G (2018) Preparation and Melting of Scrap in Aluminum Recycling: A Review. Metals 8:249. https://doi.org/10.3390/met8040249

11. Taylor JA, Prakash M, Pereira GG, et al (2010) Predicting Dross Formation in Aluminium Melt Transfer Operations. In: Materials Science Forum. https://www.scientific.net/MSF.630.37. Accessed 2 Nov 2018

12. Kevorkijan V, Kovačec U, Žist S (2020) Automatic Skimming Procedure for Reducing Aluminium Losses and Maintaining the Uniform Quality of the Molten Metal. In: Tomsett A (ed) Light Metals 2020. Springer International Publishing, Cham, pp 1137–1140

13. Bonner SJ, Taylor JA, Yao J-Y, Rhamdhani MA (2016) Oxidation of Commercial Purity Aluminum Melts: An Experimental Study. In: Sadler BA (ed) Light Metals 2013. Springer International Publishing, Cham, pp 993–997

14. Manfredi O, Wuth W, Bohlinger I (1997) Characterizing the Physical and Chemical Properties of Aluminum Dross. JOM 49:48–51. https://doi.org/10.1007/s11837-997-0012-9

15. Ünlü N, Drouet MG (2002) Comparison of Salt-Free Aluminum Dross Treatment Processes. Resources, Conservation and Recycling 36:61–72. https://doi.org/10.1016/S0921-3449(02)00010-1

16. Field DJ, Scamans GM, Butler EP (1987) The High Temperature Oxidation of Al-4.2 Wt Pct Mg Alloy. Metall Mater Trans A 18:463–472. https://doi.org/10.1007/BF02648807

17. Innus AB, Villeneuve M (1989) Dross cooling apparatus

18. Tsakiridis PE (2012) Aluminium Salt Slag Characterization and Utilization – A Review. Journal of Hazardous Materials 217–218:1–10. https://doi.org/10.1016/j.jhazmat.2012.03.052

19. Das BR, Dash B, Tripathy BC, et al (2007) Production of η-Alumina from Waste Aluminium Dross. Minerals Engineering 20:252–258. https://doi.org/10.1016/j.mineng.2006.09.002

20. Aluminium Dross Processing: A Global Review. In: alcircle. https://www.alcircle.com/specialreport/306/drossprocessing. Accessed 22 Oct 2020

21. Calder GV, Stark TD (2010) Aluminum Reactions and Problems in Municipal Solid Waste Landfills. Practice Periodical of Hazardous, Toxic, and Radioactive Waste Management 14:258–265. https://doi.org/10.1061/(ASCE)HZ.1944-8376.0000045

22. (2007) U.S. Energy Requirements for Aluminum Production: Historical Perspective, Theoretical Limits and Current Practices

23. Ryan V Introduction to Aluminium and its Properties. https://technologystudent.com/despro_3/aluminium1.html. Accessed 25 Aug 2022

24. Primary Aluminium Production. In: International Aluminium Institute. https://international-aluminium.org/statistics/primary-aluminium-production/. Accessed 8 Aug 2022

25. Thonstad J, Fellner P, Haarberg GM, et al (2001) Aluminium Electrolysis: Fundamentals of the Hall-Héroult Process, 3rd ed. Aluminium-Verlag, Düsseldorf

26. Aarhaug TA, Ratvik AP (2019) Aluminium Primary Production Off-Gas Composition and Emissions: An Overview. JOM 71:2966–2977. https://doi.org/10.1007/s11837-019-03370-6

27. Kvande H (2014) The Aluminum Smelting Process. J Occup Environ Med 56:S2–S4. https://doi.org/10.1097/JOM.0000000000000154

28. Haupin WE (1995) Principles of Aluminum Electrolysis. 9

29. Ratvik AP, Mollaabbasi R, Alamdari H (2022) Aluminium Production Process: from Hall–Héroult to Modern Smelters. ChemTexts 8:10. https://doi.org/10.1007/s40828-022-00162-5

30. Vallejo-Olivares A, Høgåsen S, Kvithyld A, Tranell G (2022) Effect of Compaction and Thermal De-coating Pre-treatments on the Recyclability of Coated and Uncoated Aluminium. Light Metals 2022 1029–1037. https://doi.org/10.1007/978-3-030-92529-1_134

31. Vallejo-Olivares A, Philipson H, Gökelma M, et al (2021) Compaction of Aluminium Foil and Its Effect on Oxidation and Recycling Yield. In: Perander L (ed) Light Metals 2021. Springer International Publishing, Cham, pp 735–741

32. Schmitz C (2006) Handbook of Aluminium Recycling. Vulkan-Verlag

33. Padamata SK, Yasinskiy A, Polyakov P (2021) A Review of Secondary Aluminum Production and Its Byproducts. JOM 73:2603–2614. https://doi.org/10.1007/s11837-021-04802-y

34. Beheshti R, Moosberg-Bustnes J, Akhtar S, Aune RE (2014) Black Dross: Processing Salt Removal from Black Dross by Thermal Treatment. JOM 66:2243–2252. https://doi.org/10.1007/s11837-014-1178-6

35. Gronostajski J, Matuszak A (1999) The Recycling of Metals by Plastic Deformation: an Example of Recycling of Aluminium and its Alloys Chips. Journal of Materials Processing Technology 92–93:35–41. https://doi.org/10.1016/S0924-0136(99)00166-1

36. Xiao Y, Reuter MA, Boin Udo (2005) Aluminium Recycling and Environmental Issues of Salt Slag Treatment. Journal of Environmental Science and Health, Part A 40:1861–1875. https://doi.org/10.1080/10934520500183824

37. Izman S, Abdul-Kadir MR, Anwar M, et al (2012) Surface Modification Techniques for Biomedical Grade of Titanium Alloys: Oxidation, Carburization and Ion Implantation Processes. IntechOpen

38. Lawless KR (1974) The Oxidation of Metals. Rep Prog Phys 37:231–316. https://doi.org/10.1088/0034-4885/37/2/002

39. FactSage 8.1

40. Osborn CJ (1950) The Graphical Representation of Metallurgical Equilibria. JOM 2:600–607. https://doi.org/10.1007/BF03399037

41. Huai X, Zhao S, Li W (2009) Corrosion Resistance of Al_2O_3 Coating on a Steel Substrate. Journal of Ceramic Processing Research 10:618–620

42. Reimers JH (1947) Aluminium. Johan Grundt Tanum, Oslo

43. Smeltzer WW (1956) Oxidation of Aluminum in the Temperature Range 400°–600°C. J Electrochem Soc 103:209. https://doi.org/10.1149/1.2430279

44. Gulbransen EA, Wysong WS (1947) Thin Oxide Films on Aluminum. J Phys Chem 51:1087–1103. https://doi.org/10.1021/j150455a004

45. Jeurgens LPH, Sloof WG, Tichelaar FD, Mittemeijer E (2002) Growth Kinetics and Mechanisms of Aluminum-Oxide Films Formed by Thermal Oxidation of Aluminum. Journal of Applied Physics, v92, 1649-1656 (2002) 92:. https://doi.org/10.1063/1.1491591

46. Callister Jr. WD, Rethwisch DG (2011) Materials Science and Engineering, Eighth edition. John Wiley & Sons, Ltd

47. Cochran CN, Sleppy WC (1961) Oxidation of High-Purity Aluminum and 5052 Aluminum-Magnesium Alloy at Elevated Temperatures. J Electrochem Soc 108:322–327. https://doi.org/10.1149/1.2428080

48. Bergsmark E, Simensen CJ, Kofstad P (1989) The Oxidation of Molten Aluminum. Materials Science and Engineering: A 120–121:91–95. https://doi.org/10.1016/0921-5093(89)90723-5

49. Surla K, Valdivieso F, Pijolat M, et al (2001) Kinetic Study of the Oxidation by Oxygen of Liquid Al–Mg 5% Alloys. Solid State Ionics 143:355–365. https://doi.org/10.1016/S0167-2738(01)00861-X

50. Haginoya I, Fukusako T (1983) Oxidation of Molten Al–Mg Alloys. Trans JIM 24:613–619. https://doi.org/10.2320/matertrans1960.24.613

51. Sindel M, Travitzky NA, Claussen N (1990) Influence of Magnesium-Aluminum Spinel on the Directed Oxidation of Molten Aluminum Alloys. Journal of the American Ceramic Society 73:2615–2618. https://doi.org/10.1111/j.1151-2916.1990.tb06736.x

52. Akbarifar M, Divandari M, Boutorabi SMA, et al (2020) Short-Time Oxidation of Al–Mg in Dynamic Conditions. Oxid Met 94:409–429. https://doi.org/10.1007/s11085-020-09999-y

53. Impey S, Stephenson DJ, Nicholls JR (1990) A Study of the Effect of Magnesium Additions on the Oxide Growth Morphologies on Liquid Aluminium Alloys. Proc Conf on Microscopy of Oxidation 1:238–244

54. Whitaker M, Heath AR (1953) The Oxidation of Aluminium-Magnesium Alloys by Steam: A Contribution to Research on Mould Reaction. J Inst Metals 82:

55. Glazoff MV, Rashkeev SN (2010) Beryllium Adsorption at Transition Aluminas: Implications for Environmental Science and Oxidation of Aluminum Alloys. J Phys Chem C 114:14208–14212. https://doi.org/10.1021/jp1044942

56. Smith N, Gleeson B, Kvithyld A, Tranell G (2017) Effects of 2 ppm Beryllium on the Oxidation of a 5XXX Aluminum Alloy at Temperatures Between 500 and 750 °C. In: Ratvik AP (ed) Light Metals 2017. Springer International Publishing, Cham, pp 1465–1474

57. Czerwinski F (2004) The Early Stage Oxidation and Evaporation of Mg–9%Al–1%Zn Alloy. Corrosion Science 46:377–386. https://doi.org/10.1016/S0010-938X(03)00151-3

58. Drouzy M, Mascré C (1969) The Oxidation of Liquid Non-Ferrous Metals in Air or Oxygen. Metallurgical Reviews 14:25–46. https://doi.org/10.1179/mtlr.1969.14.1.25

59. Cooper RG, Harrison AP (2009) The Uses and Adverse Effects of Beryllium on Health. Indian J Occup Environ Med 13:65–76. https://doi.org/10.4103/0019-5278.55122

60. Yoon Y-O, Ha S-H, Yeom G-Y, et al (2016) Oxidation Behavior of Al_2Ca Added Al-5Mg Alloy in the Liquid State. In: Sadler BA (ed) Light Metals 2013. Springer International Publishing, Cham, pp 323–326

61. Ha S-H, Yoon Y-O, Kim SK (2014) Effect of Al_2Ca on Oxidation Resistance and Tensile Property of Al-5Mg Alloy. Journal of Korea Foundry Society 34:194–199. https://doi.org/10.7777/jkfs.2014.34.6.194

62. Yancey DD, DeYoung DH (1997) Calcium Contamination of Molten Al-Mg Alloys by Calcium Carbonate. In: Light Metals 1997. pp 1035–1041

63. Ozdemir O, Gruzleski JE, Drew RAL (2009) Effect of Low-Levels of Strontium on the Oxidation Behavior of Selected Molten Aluminum–Magnesium Alloys. Oxid Met 72:241. https://doi.org/10.1007/s11085-009-9158-x

64. Miresmaeili SM (2009) Effect of Strontium on the Oxidation Behavior of Liquid Al–7Si Alloys. Oxid Met 71:107–123. https://doi.org/10.1007/s11085-009-9136-3

65. Derin S, Aybarç U, Birol Y (2017) Effect of Strontium Addition on Microstructure and Mechanical Properties of AlSi7Mg0.3 Alloy. Inter Metalcast 11:688–695. https://doi.org/10.1007/s40962-016-0117-4

66. Cochran CN, Belitskus DL, Kinosz DL (1977) Oxidation of Aluminum-Magnesium Melts in Air, Oxygen, Flue Gas, and Carbon Dioxide. MTB 8:323–332. https://doi.org/10.1007/BF02657663

67. Haginoya I, Fukusako T (1979) Oxidation of Molten Al-Mg Alloy in Air-CO_2 Atmosphere. Journal of Japan Institute of Light Metals 29:285–290. https://doi.org/10.2464/jilm.29.285

68. Stevens D, Kvithyld A, Engh TA (2011) Oxidation of Rolled and Flash Anodized 3000 Aluminum in Air, Nitrogen, Oxygen, and Carbon Dioxide Atmospheres. Materials Science Forum 693:63–70. https://doi.org/10.4028/www.scientific.net/MSF.693.63

69. Smith N, Gleeson B, Saidi W, et al (2019) Effects of CO_2 Cover Gas and Yttrium Additions on the Oxidation of AlMg Alloys. In: Chesonis C (ed) Light Metals 2019. Springer International Publishing, Cham, pp 1025–1032

70. Thiele W (1962) Die Oxydation von Aluminium-und Aluminiumlegierungs-Schmelzen. Aluminium part 1:707–715

71. Impey S, Stephenson DJ, Nicholls JR (1993) The Influence of Surface Preparation and Pretreatments on the Oxidation of Liquid Aluminium and Aluminium-Magnesium Alloys. Proc Conf on Microscopy of Oxidation 2:323–337

72. Blackburn PE, Gulbransen EA (1960) Aluminum Reactions with Water Vapor, Dry Oxygen, Moist Oxygen, and Moist Hydrogen between 500° and 625°C. J Electrochem Soc 107:944. https://doi.org/10.1149/1.2427576

73. Schoenitz M, Chen C-M, Dreizin EL (2009) Oxidation of Aluminum Particles in the Presence of Water. J Phys Chem B 113:5136–5140. https://doi.org/10.1021/jp807801m

74. Belitskus DL (1971) Oxidation of Molten Al-Mg Alloy in Air, Air-SO_2, and Air-H_2S Atmospheres. Oxid Met 3:313–317. https://doi.org/10.1007/BF00614625

75. Campbell J (2003) Castings. Elsevier

76. Solem CKW, Ekstrøm KE, Tranell G, Aune RE (2020) Evaluation of the Effect of CO_2 Cover Gas on the Rate of Oxidation of an AlMgSi Alloy. In: Tomsett A (ed) Light Metals 2020. Springer International Publishing, Cham, pp 1141–1147

77. Solem CKW, Solberg E, Tranell G, Aune RE (2021) Influence of Mg Concentration on the Inhibiting Effect of CO_2 on the Rate of Oxidation of Aluminum Alloys 5182 and 6016. Light Metals 2021 742–750. https://doi.org/10.1007/978-3-030-65396-5_97

78. Solem CKW, Vullum PE, Tranell G, Aune RE (2022) Heat Treatment of Mg-Containing Aluminum Alloys 5182 and 6016 in an Oxidizing Atmosphere with 4% CO_2. In: Eskin D (ed) Light Metals 2022. Springer International Publishing, Cham, pp 587–593

79. Solem CKW, Vullum PE, Ebadi M, et al (2022) The Role of CO_2 in the Oxidation-Protection of Mg-Containing Aluminum Alloys. Metall Mater Trans B. https://doi.org/10.1007/s11663-022-02524-3

80. Hu K, Reed D, Robshaw TJ, et al (2021) Characterisation of Aluminium Black Dross Before and After Stepwise Salt-Phase Dissolution in Non-Aqueous Solvents. Journal of Hazardous Materials 401:123351. https://doi.org/10.1016/j.jhazmat.2020.123351

81. Maropoulos S, Kountouras D, Voulgaraki X, et al (2011) A Characterization Method for Al Recovery from Dross Based on Compression at Elevated Temperatures. Advances in Tribology 2011:e395716. https://doi.org/10.1155/2011/395716

82. Steglich J, Friedrich B, Rosefort M (2020) Dross Formation in Aluminum Melts During the Charging of Beverage Can Scrap Bales with Different Densities Using Various Thermal Pretreatments. JOM 72:3383–3392. https://doi.org/10.1007/s11837-020-04268-4

83. Impey SA (1989) The Mechanism of Dross Formation on Aluminium and Aluminium Magnesium Alloys. Cranfield University

84. Hiraki T, Noguchi H, Maruoka N, Nagasaka T (2018) In Situ Observation of Dross Formation During Melting of Al–Mg Alloy. In: Martin O (ed) Light Metals 2018. Springer International Publishing, Cham, pp 1141–1146

85. Peterson RD (2011) A Historical Perspective on Dross Processing. Materials Science Forum 693:13–23. https://doi.org/10.4028/www.scientific.net/MSF.693.13

86. Abdulkadir A, Ajayi A, Hassan MI (2015) Evaluating the Chemical Composition and the Molar Heat Capacities of a white Aluminum Dross. Energy Procedia 75:2099–2105. https://doi.org/10.1016/j.egypro.2015.07.326

87. David E, Kopac J (2012) Hydrolysis of Aluminum Dross Material to Achieve Zero Hazardous Waste. Journal of Hazardous Materials 209–210:501–509. https://doi.org/10.1016/j.jhazmat.2012.01.064

88. Hwang J-Y, Huang X, Xu Z (2006) Recovery of Metals from Aluminum Dross and Saltcake. https://doi.org/10.4236/JMMCE.2006.51003

89. Meshram A, Gautam D, Singh KK (2020) Recycling of White Aluminium Dross: Production of Potash Alum. Trans Indian Inst Met 73:1239–1248. https://doi.org/10.1007/s12666-020-01973-1

90. Drouet MG, Handfield M, Meunier J, Laflamme CB (1994) Dross Treatment in a Rotary Arc Furnace with Graphite Electrodes. JOM 46:26–27. https://doi.org/10.1007/BF03220691

91. Drouet MG, LeRoy RL, Tsantrizos PG (2013) Drosrite Salt-Free Processing of Hot Aluminum Dross. In: Stewart DL, Daley JC, Stephens RL (eds) Recycling of Metals and Engineercd Materials. John Wiley & Sons, Inc., Hoboken, NJ, USA, pp 1135–1145

92. Kevorkijan V (2002) Evaluating the Aluminum Content of Pressed Dross. JOM 54:34–36. https://doi.org/10.1007/BF02701070

93. Tsakiridis PE, Oustadakis P, Agatzini-Leonardou S (2013) Aluminium Recovery During Black Dross Hydrothermal Treatment. Journal of Environmental Chemical Engineering 1:23–32. https://doi.org/10.1016/j.jece.2013.03.004

94. Li Y, Chen X, Liu B (2021) Experimental Study on Denitrification of Black Aluminum Dross. JOM 73:2635–2642. https://doi.org/10.1007/s11837-021-04771-2

95. Gökelma M, Meling I, Soylu E, et al (2019) A Method for Assessment of Recyclability of Aluminum from Incinerated Household Waste. In: Chesonis C (ed) Light Metals 2019. Springer International Publishing, Cham, pp 1359–1365

96. S Aadli A (2018) Aluminium Silicon Hypereutectic Alloys from 6063 Alloy's Black Dross Using Silicon Lumps and Flux. ECS 21–23. https://doi.org/10.33805/2641-7383.105

97. Jody BJ, Daniels EJ, Bonsignore PV, Karvelas DE (1991) Recycling of Aluminum Salt Cake. Argonne National Lab., IL (United States)

98. Huang X-L, Badawy AE, Arambewela M, et al (2014) Characterization of Salt Cake from Secondary Aluminum Production. Journal of Hazardous Materials 273:192–199. https://doi.org/10.1016/j.jhazmat.2014.02.035

99. Moser CJ (1976) Furnace Dross — Its Formation and Recovery. In: Leavitt SR (ed) Light Metals 1976. Springer International Publishing, Cham, pp 150–156

100. Moore P (2020) Rio Tinto signs up Ultromex to treat landfill aluminium salt slag. In: International Mining. https://im-mining.com/2020/11/16/rio-tinto-signs-ultromex-treat-landfill-aluminium-salt-slag/. Accessed 5 Sep 2022

101. Smith N (2019) Methods of Oxidation Inhibition for Al-Mg Alloys. Doctoral Thesis, NTNU, Norwegian University of Science and Technology

102. Dispinar D, Campbell J (2007) Effect of Casting Conditions on Aluminium Metal Quality. Journal of Materials Processing Technology 182:405–410. https://doi.org/10.1016/j.jmatprotec.2006.08.021

103. Johansen I, Strømhaug SI (2016) Energy Control in Primary Aluminium Casthouse Furnaces. In: Sadler BA (ed) Light Metals 2013. Springer International Publishing, Cham, pp 935–939

104. Belt C (2015) Current State of Aluminum Melting and Holding Furnaces in Industry. JOM 67:2690–2695. https://doi.org/10.1007/s11837-015-1599-x

105. Bui RT, Perron J (1988) Performance Analysis of the Aluminum Casting Furnace. Metall Mater Trans B 19:171–180. https://doi.org/10.1007/BF02654201

106. Prakash M, Pereira GG, Cleary PW, et al (2010) Validation of SPH Predictions of Oxide Generated during Al Melt Transfer. Progress in Computational Fluid Dynamics, an International Journal

107. DeYoung DH (1997) Na and Ca Pick-up from Hall Bath in Ingot Furnaces. In: Light Metals 1997. Springer International Publishing, Cham, pp 21–27

108. Meshram A, Singh KK (2018) Recovery of Valuable Products from Hazardous Aluminum Dross: A Review. Resources, Conservation and Recycling 130:95–108. https://doi.org/10.1016/j.resconrec.2017.11.026

109. Michel J (1978) Device and Process for Limiting Surface Oxidation of Glowing Hot Metal Dross

110. McMahon PJ, Spoel H, Mcginley J (1987) Dross cooler and processor

111. Peel A, Herbert J, Roth D, Collins MJ (2010) Dross Processing Technology. In: Materials Science Forum. https://www.scientific.net/MSF.630.53. Accessed 13 Mar 2019

112. Peel A, Herbert J, Connaughton R, Cotton H (2011) Preserving Metal Units Utilising the Latest Generation of Aluminium Dross Press. Materials Science Forum 693:33–43. https://doi.org/10.4028/www.scientific.net/MSF.693.33

113. Dross Press. In: Altek. https://www.altek-al.com/products/presses/dross-press. Accessed 15 Aug 2022

114. How LF, Islam A, Jaafar MS, Taufiq-Yap YH (2017) Extraction and Characterization of γ-Alumina from Waste Aluminium Dross. Waste Biomass Valor 8:321–327. https://doi.org/10.1007/s12649-016-9591-4

115. Soós Z, Géber R, Toth C, et al (2017) Utilization of Aluminium Dross as Asphalt Filler. Epitoanyag - Journal of Silicate Based and Composite Materials 69:89–93. https://doi.org/10.14382/epitoanyag-jsbcm.2017.15

116. Li X, Hwang J, Jeon H, Zhang Z (2010) Utilization of Aluminum Slag for the Expansion of Lightweight Concrete. pp 279–286

117. Elseknidy MH, Salmiaton A, Nor Shafizah I, Saad AH (2020) A Study on Mechanical Properties of Concrete Incorporating Aluminum Dross, Fly Ash, and Quarry Dust. Sustainability 12:9230. https://doi.org/10.3390/su12219230

118. Javali S, Chandrashekar AR, Naganna SR, et al (2017) Eco-Concrete for Sustainability: Utilizing Aluminium Dross and Iron Slag as Partial Replacement Materials. Clean Techn Environ Policy 19:2291–2304. https://doi.org/10.1007/s10098-017-1419-9

119. Philipson H, Solbakk GL, Wallin M, et al (2022) Innovative Utilization of Aluminum-Based Secondary Materials for Production of Metallurgical Silicon and Alumina-Rich Slag. In: Light Metals 2022. Springer International Publishing, Cham, pp 1038–1045

120. Philipson H, Wallin M, Einarsrud KE, Tranell G (2021) Kinetics of Silicon Production by Aluminothermic Reduction of Silica Using Aluminum and Aluminum Dross as Reductants

121. Geveci A, Aydemir O (2006) Usage of Aluminum Dross for Slag Treatment in Secondary Steelmaking to Decrease Amount of Reducible Oxides in Ladle Furnace. 7:351–357

122. Blomberg J, Söderholm P (2009) The Economics of Secondary Aluminium Supply: An Econometric Analysis Based on European Data. Resources, Conservation and Recycling 53:455–463. https://doi.org/10.1016/j.resconrec.2009.03.001

123. Lin B, Li X (2011) The Effect of Carbon Tax on Per Capita CO_2 Emissions. Energy Policy 39:5137–5146. https://doi.org/10.1016/j.enpol.2011.05.050

124. Polysykliske aromatiske hydrokarboner (PAH). In: Miljøstatus. https://miljostatus.miljodirektoratet.no/tema/miljogifter/prioriterte-miljogifter/polysykliske-aromatiske-hydrokarboner-pah/. Accessed 4 Sep 2022

125. Evans JW (2007) The Evolution of Technology for Light Metals over the Last 50 Years: Al, Mg, and Li. JOM 59:30–38

Supplements

Paper 1

Evaluation of the Effect of CO_2 Cover Gas on the Rate of Oxidation of an AlMgSi Alloy

Cathrine Kyung Won Solem, Kai Erik Ekstrøm, Gabriella Tranell, and Ragnhild E. Aune

Abstract

Small additions of beryllium (Be) to aluminum magnesium (AlMg) alloys have proven to decrease their oxidation rate during industrial liquid metal handling. As Be can cause respiratory health issues, it is desirable to evaluate alternative methods to inhibit the oxidation rate. Earlier work has revealed that small amounts of carbon dioxide (CO_2) to the surrounding atmosphere has a positive effect. In the present study the oxidation behavior of an aluminum magnesium silicon (AlMgSi) alloy has been investigated using a Differential Scanning Calorimetric (DSC) unit equipped with a Thermogravimetric Analyzer (TGA). Changes in both the heat flux and the mass have been monitored during exposer to 20% argon (Ar) and 80% *synthetic air*, 99.999% pure *Ar*, and a gaseous mixture of 20% Ar, 76% synthetic air and 4% CO_2 at 750 °C for 7 h. The results revealed a one-step mass gain when heated in *synthetic air*, giving a total mass gain of 12.33% and an oxide layer thickness of >15 µm. Pure *Ar* had a positive effect on the oxidation rate lowering the mass gain to 2.80% and a thickness of ~10 µm. A mass gain of only 0.46% and a continuous dense oxide layer of 200–400 nm, with an additional granular discontinuous oxide layer of ~2 µm underneath, was obtained during heating in 4% CO_2. This confirms that even in the case of the AlMgSi alloy, small amounts of CO_2 have a significant inhibiting effect on the oxidation rate.

Keywords

AlMgSi alloy • Oxidation • Breakaway oxidation • Ar • Synthetic air • CO_2

Introduction

Aluminum (Al) alloys are used in numerous applications such as transportation, packaging and building constructions [1]. During liquid processing, the Al alloys oxidize when exposed to oxidizing atmospheres, e.g. air [1–4], resulting in significant metal losses ranging from 1 to 10% of the melt [5].

Aluminum magnesium (AlMg) alloys is a common group of materials that are typically used in automotive applications, in maritime environments, and in beverage cans. Their frequent use is mostly due to their corrosion resistance.

Oxidation of AlMg Systems

Over the years, the oxidation of AlMg alloys has been extensively studied by several researchers, including the influence of atmosphere on the rate and product of oxidation [1, 3, 6–9]. The early work of Cochran and Sleppy [10] established that aluminum alloys containing Mg have a significantly higher mass gain than high-purity aluminum when exposed to air [10]. Further investigations monitoring the mass as a function of time and temperature while exposing it to different cover gases, e.g. air containing water vapor [10] and dried air [11], revealed that the mass gain of AlMg alloys is identified by a two-step mass gain process. Firstly, a linear mass gain is obtained due to the formation of a granular magnesium oxide (MgO) layer, and secondly, a rapid breakaway oxidation mass gain due to the formation of magnesium aluminate spinel ($MgAl_2O_4$) [2, 7, 11], characterized by nodules covering the surface, as well as "cauliflower" shaped topography [12, 13]. In Eqs. (1) and (2) the reactions occurring with respect to one mole O_2 (g), with a decrease in Gibbs Energy (ΔG^0), are presented [14].

$$2/3\,MgO + 4/3\,Al + O_2(g) = 2/3\,MgAl_2O_4 \qquad \Delta G^0_{750\,^\circ C} = -925.66\ kJ \tag{1}$$

C. K. W. Solem (✉) · K. E. Ekstrøm · G. Tranell · R. E. Aune
Department of Materials Science and Engineering, Norwegian University of Science and Technology (NTNU), Trondheim, Norway
e-mail: cathrine.k.w.solem@ntnu.no

A. Tomsett (ed.), *Light Metals 2020*, The Minerals, Metals & Materials Series,
https://doi.org/10.1007/978-3-030-36408-3_154

$$2\,Mg + O_2(g) = 2\,MgO$$
$$\Delta G^0_{750\,^\circ C} = -981.64\ kJ \quad (2)$$

Oxidation of AlMgSi Systems

Over the years it has been reported in literature that additions of Mn, Fe, Cu and Si to Al do not have a significant effect on the rate of oxidation in regard to binary Al systems [12]. However, for higher order systems, it is not well understood how these elements effect the oxidation rate, or what oxides that are formed in which order. Two different oxide formation processes have been suggested, i.e. the formation of (i) an Al–Mg–O oxide rich in MgO, and (ii) aluminum oxide (Al_2O_3) together with other oxides, but in both cases Si is only present as a trace element and not as a pure component in the oxide [12].

When looking at the formation of Mg_2Si at 750 °C, the ΔG^0 is significantly higher than for SiO_2, Mg_2SiO_4 and Al_2O_3. From a thermodynamic point of view, this indicates that Mg_2Si will not be favored at this temperature, see Eqs. (3)–(6) [14].

$$2\,Mg + Si = Mg_2Si$$
$$\Delta G^0_{750\,^\circ C} = -66.93\,kJ \quad (3)$$

$$Si + O_2(g) = SiO_2$$
$$\Delta G^0_{750\,^\circ C} = -726.17\ kJ \quad (4)$$

$$2\,MgO + Si + O_2(g) = Mg_2SiO_4$$
$$\Delta G^0_{750\,^\circ C} = -785.23\,kJ \quad (5)$$

$$4/3\,Al + O_2(g) = 2/3\,Al_2O_3$$
$$\Delta G^0_{750\,^\circ C} = -902.53\,kJ \quad (6)$$

In Fig. 1a and b the Al–Mg–O_2–Si phase diagram is presented as a function of the partial pressure of O_2 with respect to the activity of Mg and Al in the melt, respectively [15]. As can be seen from the phase diagrams, there are several different oxides that may be formed at the temperature of interest, i.e. (i) depending on the activity of Mg in the Al melt, Al_2O_3 and $MgAl_2O_4$ (SPIN) are stable together with pure Si (s), (ii) at higher partial pressures, Mg_2SiO_4 is stable together with $MgAl_2O_4$, (iii) when the activity of Al in the melt is low, $MgAl_2O_4$ and Si (s) are stable, and (iv) there may be an equilibrium between Mg_2Si and MgO, with no Al present in neither of the phases.

Inhibition of the Oxide Layer

Small additions (2–200 ppm) of Be to AlMg alloys have proven to have an inhibiting effect on the formation of the oxide layer, and thereby also on the overall rate of oxidation during processing [1, 3, 13]. Smith et al. [13] reported recently that with an addition of 100 ppm Be to an AlMg5 alloy heated in air at 700 °C for 6 h, a granular MgO layer was formed on the surface of the material with an additional thin beryllium oxide (BeO) layer underneath. The BeO layer inhibited the transport of Mg from the bulk through the oxide, hence, limiting the oxidation and the formation of $MgAl_2O_4$, i.e. the second mass gain step was avoided. Be is, however, well-known for being hazardous, causing respiratory health

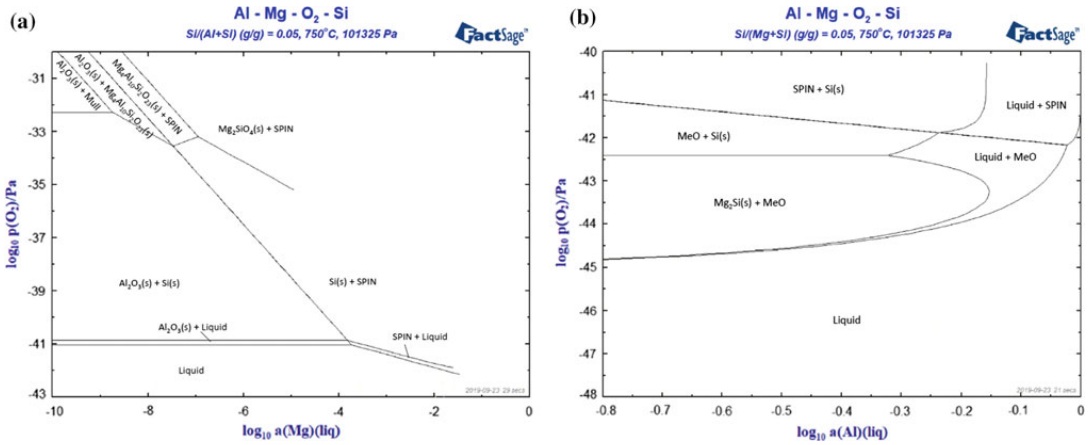

Fig. 1 Al–Mg–O_2–Si phase diagram as a function of the activity of the partial pressure of O_2 at 750 °C with respect to **a** the activity of Mg and **b** the activity of Al in the melt, where $MgAl_2O_4$, Al_2SiO_5 and MgO are referred to as Mull, SPIN and MeO, respectively [15]

issues, thus, it is desirable to evaluate alternative methods of inhibiting oxidation of AlMg-based alloys.

CO_2 has been investigated as a protective cover gas for AlMg alloys, both as pure gas and in gaseous mixtures with air, water vapor and Ar. Additions of small amounts of CO_2 have proven to have an inhibiting effect on the onset of breakaway oxidation [2, 4], limiting the evaporation of Mg from the bulk metal through the formed MgO oxide layer. In the case of AlMg5, concentrations as low as 5% CO_2 in the cover gas gave a pronounced protective effect (comparable to 20% CO_2 in both Ar and air), which resulted in a mass gain <0.5% when heated at 750 °C for 7 h. The thin oxide layer formed on the alloy contained carbon, where the ratio between O and C was found to decrease towards the oxide-alloy interface as a result of Mg reducing the CO_2 gas [2].

While the oxidation behavior of the AlMg system is partly understood, there is still a lack of knowledge in regards to the oxidation of higher order AlMg-based systems. Therefore, in the present study, the oxidation of an AlMgSi alloy will be investigated through Differential Scanning Calorimetry (DSC) equipped with a Thermogravimetric Analyzes (TGA). Special attention will be given to the effect that silicon (Si) has on the morphology and composition of the oxide layer, as well as the overall rate of oxidation during exposure to different cover gases, i.e. (i) 20% Ar and 80% synthetic air, (ii) pure Ar, and (iii) a gaseous mixture of 20% Ar, 76% synthetic air and 4% CO_2.

Experimental

Sample Preparation

The AlMgSi alloy investigated was tailored from 99.999% pure Al (Alfa Aesar), 99.98% pure Mg (Sigma Aldrich) and 99.9999% pure Si (Wacker). The elements were placed layer by layer in an Al_2O_3 crucible with an inner diameter of 45 mm, i.e. the bottom was covered by a layer of Al, followed by a layer of Mg and Si and finished off with another layer of Al. The crucible was later placed in a vacuum induction furnace in an inert atmosphere of 99.999% pure Ar, heated to 850 °C and held for 30 min to ensure homogeneous distribution of the elements in the alloy (theoretical melting temperature is 556 °C [15]). After the isothermal segment, the furnace was turned off and the alloy was naturally cooled to ambient temperature inside the furnace. The alloy was separated from the crucible and milled to remove any residues securing a clean metal surface. In Table 1 the trace elements present in the master alloy, as well as the quantitative data from the chemical analysis performed with a Nu Instrument Astrum Glow Discharge Mass Spectrometry (GDMS), is presented.

The alloy was then cut into 1.5 mm thick plates, which later were cut into small discs having a diameter of ~3–4 mm, before being polished to 5 µm grid. After polishing, the samples were stored in ethanol until the experiments were carried out in a Simultaneous Thermal Analyzer (STA).

Differential Scanning Calorimetry with Thermogravimetric Analysis (DSC-TG)

A NETZSCH Simultaneously Thermogravimetric Analyzer (STA) model 449 F Jupiter apparatus having a Differential Scanning Calorimetric (DSC) set up was used to monitor the heat flux and mass change of the discs as a function of time and temperature. Three parallel experiments for each cover gas, i.e. (i) 99.999% pure Ar (from here on referred to as Ar), (ii) 20% pure Ar and 80% synthetic air (from here on referred to as synthetic air), and (iii) a gaseous mixture of 20% pure Ar, 76% synthetic air and 4% CO_2 (from here on referred to as 4% CO_2) were carried out to confirm reproducibility of the results. The DSC-TG trials were conducted with a heating and cooling rate of 10 °C/min and a dwell time of 7 h at 750 °C using Al_2O_3 crucibles with an inner diameter of 6 mm. The typical operating temperature used in cast houses during production of Al is ~750 °C and therefore the temperature chosen for the isothermal sections during the DSC-TG trials.

Microscopy

A Zeiss Ultra 55 Limited Edition Secondary Electron Microscope (SEM) was used to investigate the surfaces of the discs after the DSC-TG analyzes, and a FEI Helios NanoLab Dual Focused Ion Beam (FIB) was used to visualize the cross sections, i.e. the oxide layers, for further evaluation. The cross sections were also investigated using Energy Dispersive Spectroscopy (EDS) for elemental mapping.

Table 1 Chemical analyses given in weight percentage (wt%) of the AlMgSi alloy based on Glow Discharge Mass Spectrometry (GDMS) analysis

	Al	Mg	Si	Fe	Cu	Ca	Mn
AlMgSi (wt%)	Balance	6.7670	6.6933	0.0087	0.0087	0.0003	0.0002
Std. dev. (%)	–	0.1786	0.1650	0.0001	0.0002	0.0000	0.0000

Results and Discussion

The mass gain (TGA) of the AlMgSi discs heated at 750 °C for 7 h in the three different cover gases investigated in the present study, i.e. synthetic air, Ar, and 4% CO_2, is presented in Fig. 2a. As can be seen from the figure, a significant increase in the mass was obtained for the discs heated in synthetic air (dotted gray graph), resulting in an average of 12.33% having a standard deviation of 0.22%. An inhibitition of the rate of oxidation was obtained when heating the discs in Ar resulting in a mass gain of 2.80% with a standard deviation of 0.08%, and even greater for 4% CO_2 resulting in an increase of only 0.46% with a standard deviation of 0.11%.

In Fig. 2b the mass gain and the heat flux for the AlMgSi discs heated in synthetic air are presented. As can be seen from the figure, a significant mass gain is observed after ~2 h, confirmed by deep negative heat fluxes indicating that exothermic reactions had taken place, e.g. through Eqs. (1) and (2). It can be noted that even though the mass gain is only in one step and not two well-defined separated peaks as reported in the literature, the heat flux consists of several peaks indicating that more than one reaction had occurred. The microscopic analysis of the surface morphology reveals the formation of granular MgO particles on the surface of the heated discs, see Fig. 3a, similar to the cauliflower shaped nodulus recognized from literature. The cross section of the oxide layer presented in Fig. 4a reveals the existence of an oxide layer (light gray areas), where the density of the oxide layer decreases with increasing depth in the sample. The total thickness of the layer is, however, believed to be thicker than what is visible in the figure, i.e. >15 µm. The EDS results reveals that Al, Mg and O is present in the oxide layer closest to the surface of the heated discs, a Si rich area deeper in the oxide layer, and high concentrations of Al in the lowest area of the cross section. This indicates the formation of MgO and $MgAl_2O_4$, and a phase containing Si, O and Mg closest to the bulk metal, e.g. Mg_2SiO_4. Although the oxide layer was established to be thicker when heating the discs in synthetic air than in Ar, the discs had less charging in SEM, implying a higher conductivity in the case of these dicsc. This may be explained by the smooth areas in between the granular oxide layer, see Fig. 3a, resulting in a thinner oxide layer increasing the

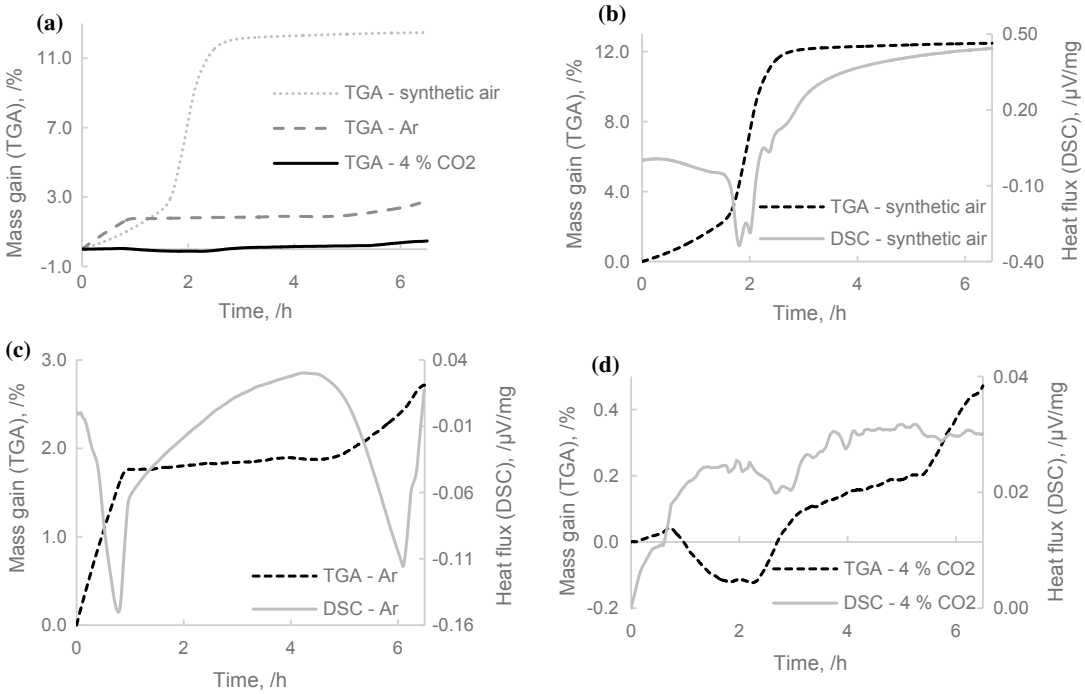

Fig. 2 DSC-TG results for AlMgSi discs heated at 750 °C for 7 h. **a** The mass gain (TGA) of the discs when heated in synthetic air (dotted gray graph), Ar (dashed gray graph), and 4% CO_2 (straight black graph). **b–c** The mass gain (TGA, dashed black graphs) and the heat flux (DSC, straight gray graphs) when heated in synthetic air, Ar and 4% CO_2. All graphs have been plotted from the time the temperature had stabilized at 750 °C, and negative heat flux peaks represent exothermic reactions

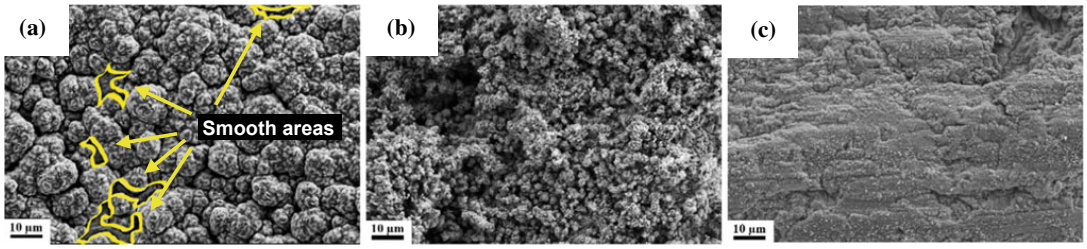

Fig. 3 Secondary Electron Microscopy (SEM) images with a magnification of 1000X of AlMgSi discs heated at 750 °C for 7 h in **a** synthetic air where the surface is covered by granular oxide with some smooth areas in between (see yellow areas). **b** Ar where the surface is covered by granular oxide, and **c** 4% CO_2 where the surface is covered by fine particles and a rougher horizontal structure/texture with some smooth areas in between

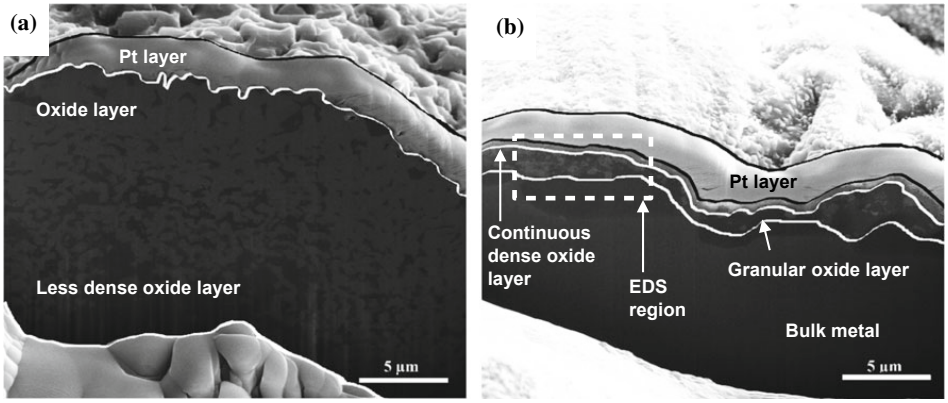

Fig. 4 The cross sections of the AlMgSi discs heated at 750 °C for 7 h with a magnification of 5000X based on SEM images obtained using a Focused Ion Beam (FIB) instrument, where **a** shows a disc heated in synthetic air where the oxide (light gray) is partly integrated in an Al matrix (dark gray), and **b** a disc heated in 4% CO_2 revealing a thin continuous dense oxide layer with an additional granular oxide layer underneath. The dashed rectangular shows the region where the Energy Dispersive Spectrometry (EDS) analysis was performed

conductivity of the electron beam. In addition, these areas may be the result of breakaway oxidation, i.e. the formation of $MgAl_2O_4$, which partly occurs simultaneously with the formation of MgO.

In Fig. 2c the mass gain and the heat flux for the AlMgSi discs heated in Ar are presented. As can be seen from the figure, a two-step mass gain is obtained for the heated discs, where the first linear mass gain stabilizes after ~50 min, before increasing again after ~5 h. This is also identified by the heat flux, revealing two exothermic (negative) peaks, which indicates that there are stable oxides spontaneously generated on the surface of the heated discs, e.g. through Eqs. (1) and (2). When looking at the surface morphology in Fig. 3b, a homogeneous layer consisting of small nods similar to those obtained for the discs heated in synthetic air is obtained. The EDS analysis of the cross section reveals the formation of an oxide layer with a total thickness of ~10 µm. The presence of Mg and O in the oxide layer is confirmed, indicating that the formation of MgO had taken place, which justifies the rapid linear mass gain seen from the dashed black graph in Fig. 2c. For the second mass gain step seen in the same figure, hardly any Al was detected, implying the absence of $MgAl_2O_4$, which is identified to be the product of the second mass gain for AlMg alloys when exposed to oxidizing atmospheres. However, the initial stage of the second mass gain after ~5 h, indicates that the formation of $MgAl_2O_4$ may not be finalised as the mass was still increasing after 7 h. No indication of Mg_2SiO_4 was detected in this sample.

When adding 4% CO_2 in the cover gas, a significantly drop in the mass gain of the heated discs is observed, see Fig. 2d. A total mass change of only 0.46% is measured for the isothermal segment, and only one well-defined negative heat flux peak is identified after ~3 h. However, the peak is

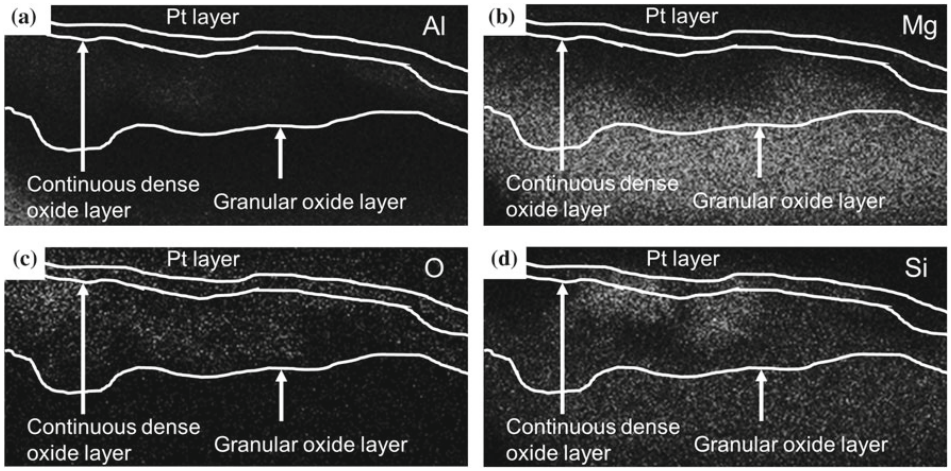

Fig. 5 EDS analysis of the AlMgSi discs heated at 750 °C for 7 h in 4% CO_2 of **a** Al, **b** Mg, **c** O and **d** Si, showing a dense oxide layer of Al, O and partly Si, and a Mg rich granular oxide layer with Al, O and Si

not as significant as the peaks obtained in the case of the discs heated in synthetic air and Ar. Through the microscopic evaluation the existence of a clear texture and cracks on the surface of the heated discs become visible at a magnification of 1000×, see Fig. 3c. The cross section seen in Fig. 4b reveals a two-layered oxide region consisting of a 200–400 nm thick continuous dense oxide layer with an additional ~2 µm granular oxide layer underneath. The region at which the EDS analysis was performed is marked with a dashed white rectangular in Fig. 4b, and the results reveal the presence of Al, Mg, O and Si in the oxide layer. The elemental mapping seen in Fig. 5a–d, confirms the presence of Al, O and Si in the upper region of the cross section, i.e. close to the continuous dense oxide layer, which may be due to formation of Al_2O_3 and Si (s). This occurs locally creating a high Si concentration, which allows precipitation of Si crystals during solidification as a consequence of low activity of Mg in the melt. An increase of Mg as a function of depth into the granular oxide layer is observed, and a region with higher concentration of Mg and Si is identified to exist. According to the phase diagram, Mg_2Si may be formed as a result of the lower activity of Al at the interface between the granular oxide layer and the bulk metal. This also correlates with the low heat flux detected after ~3 h (Fig. 2d), compared to the more negative peaks measured for synthetic air (Fig. 2b) and Ar (Fig. 2c) generating MgO, $MgAl_2O_4$ and Mg_2SiO_4, i.e. lower ΔG^0 values causing deeper heat flux peaks than for Mg_2Si. As a result, the 200–400 nm thin oxide layer formed on the surface of the heated AlMgSi discs is comparable with the findings of a similar layer established to exist for Al_5Mg when heated in a cover gas containing small amounts of CO_2, retarding the evaporation of Mg towards the surface and the overall formation of the oxide layer [2]. Further investigations are, however, needed to verify the results using Transmission Electron Microscope (TEM) and X-ray Photoelectron Spectroscopy (XPS).

Conclusion

An AlMgSi alloy has been investigated using a DSC-TG apparatus at 750 °C for 7 h in three different cover gases, i.e. (i) 20% pure Ar and 80% synthetic air, (ii) 99.999% pure Ar, and (iii) a gaseous mixture of 20% pure Ar, 76% synthetic air and 4% CO_2. The rate of oxidation has been monitored in regards of mass gain (TGA) and heat flux (DSC), and further evaluation have been carried out by microscopic analyses. A decrease in the mass gain from 12.33% to 2.80% was measured when changing the cover gas from synthetic air to pure Ar. The thickness of the oxide layer also decreased from >15 µm to ~10 µm, where the phases present in the oxide layers changed from MgO, $MgAl_2O_4$ and Mg_2SiO_4 to only MgO. A cover gas containing 4% CO_2 proved to have a significant inhibiting effect on the rate of oxidation, resulting in a mass gain of only 0.46%. In this case a continuous dense oxide layer with a thickness of 200-400 nm, covering an additional ~2 µm thick granular oxide layer, were identified to exist. The dense layer proved to consists of Al_2O_3 and Si (s), and the interface between the granular layer and the bulk of Mg_2Si and pure Si (s), which were the result of the low activity of Mg and Al, respectively.

Future Work

Future work will include investigations of the oxide layers formed during heat treatment of the AlMgSi discs during exposure to different cover gases, i.e. synthetic air, pure Ar and gaseous mixtures of Ar, synthetic air and CO_2. TEM and XPS will be used to confirm the mechanisms involved in the formation of the oxide layers by evaluating the chemical composition and morphology of the layers, as well as the overall behavior of Si. Experiments varying the relative concentrations of Mg and Si in the alloy will also be carried out to get a more comprehensive understanding of how the chemical composition and cover gas affect the oxidation rate. The holding time of the isothermal segment will be increased, to allow for the evaluation of any breakaway oxidation for the AlMg-, AlSi- and AlMgSi-based alloys.

Acknowledgements The authors would like to thank the Department of Materials Science and Engineering at the Norwegian University of Science and Technology (NTNU), Trondheim, Norway, the Centre for Research-Based Innovation (SFI Metal Production), and the Research Council of Norway (NFR Project number 237738) for funding the project.

References

1. K. Surla, F. Valdivieso, M. Pijolat, M. Soustelle, and M. Prin, "Kinetic study of the oxidation by oxygen of liquid Al–Mg 5% alloys," *Solid State Ionics*, vol. 143, no. 3, pp. 355–365, Jul. 2001.
2. N. Smith, B. Gleeson, W. A. Saidi, A. Kvithyld, and G. Tranell, "Mechanism behind the Inhibiting Effect of CO_2 on the Oxidation of Al–Mg Alloys," *Ind. Eng. Chem. Res.*, vol. 58, no. 3, pp. 1434–1442, Jan. 2019.
3. D. L. Belitskus, "Oxidation of molten Al-Mg alloy in air, air-SO_2, and air-H_2S atmospheres," *Oxid Met*, vol. 3, no. 4, pp. 313–317, Jul. 1971.
4. G. Wightman and D. J. Fray, "The dynamic oxidation of aluminum and its alloys," *MTB*, vol. 14, no. 4, pp. 625–631, Dec. 1983.
5. N. Ünlü and M. G. Drouet, "Comparison of salt-free aluminum dross treatment processes," *Resources, Conservation and Recycling*, vol. 36, no. 1, pp. 61–72, Jul. 2002.
6. N. Smith, "Methods of oxidation inhibition for Al–Mg alloys," Ph. D. Thesis, NTNU, Norwegian University of Science and Technology, Trondheim, 2019.
7. C. N. Cochran, D. L. Belitskus, and D. L. Kinosz, "Oxidation of aluminum-magnesium melts in air, oxygen, flue gas, and carbon dioxide," *MTB*, vol. 8, no. 1, pp. 323–332, Mar. 1977.
8. H. Venugopalan and T. DebRoy, "Kinetics of directed oxidation of Al-Mg alloys into $A1_2O_3$ preforms," *Materials Science and Engineering: A*, vol. 232, no. 1, pp. 39–46, Jul. 1997.
9. C. Blawert, N. Hort, and K. U. Kainer, "AUTOMOTIVE APPLICATIONS OF MAGNESIUM AND ITS ALLOYS," *TRANS. INDIAN INST. MET.*, vol. 57, no. 4, p. 12, 2004.
10. C. N. Cochran and W. C. Sleppy, "Oxidation of high-purity aluminum and 5052 aluminum-magnesium alloy at elevated temperatures," *J. Electrochem. Soc.*, vol. 108, no. 4, pp. 322–327, Apr. 1961.
11. I. Haginoya and T. Fukusako, "Oxidation of molten Al–Mg alloys," *Trans. JIM*, vol. 24, no. 9, pp. 613–619, 1983.
12. J. Steglich, C. Matthies, M. Rosefort, and B. Friedrich, "Behavior of Mg–Si-rich phases in aluminum can sheets and their impact on metal oxidation during industrial thermal pre-treatment," in *Light Metals 2018*, 2018, pp. 1123–1130.
13. N. Smith, A. Kvithyld, and G. Tranell, "The mechanism behind the oxidation protection of high Mg Al alloys with beryllium," *Metall and Materi Trans B*, vol. 49, no. 5, pp. 2846–2857, Oct. 2018.
14. *HSC Chemistry 9*. Outotec Technologies.
15. *FactSage Version 7.1*.

Paper 2

Influence of Mg Concentration on the Inhibiting Effect of CO_2 on the Rate of Oxidation of Aluminum Alloys 5182 and 6016

Cathrine Kyung Won Solem, Egil Solberg, Gabriella Tranell, and Ragnhild E. Aune

Abstract

Oxidation of aluminum alloys during production is a well-known problem and contributes to significant metal losses. As small additions of CO_2 in the oxidizing atmosphere has proven to inhibit the oxidation rate for high-Mg($\geq$5wt%) aluminum alloys, the present study has aimed at evaluating its effect on alloys with varying Mg concentration in combination with other alloying elements (Si and Mn), i.e. Al alloys 5182 (AlMg4.6Mn0.4) and 6016 (AlSi1.2Mg0.4). Experiments were performed by DSC-TG (Differential Scanning Calorimetry–Thermogravimetric Analysis) using three different cover gases, i.e. (i) 80% *synthetic air* and 20% argon, (ii) 99.999% *argon,* and (iii) *4% CO_2*, 20% argon and 76% synthetic air while monitoring the mass change and heat flux at 750 °C for 7 h. A significant inhibiting effect was observed for alloy 5182 during exposure to *CO_2*, with a mass loss of -0.3%, when compared to the results obtained for *synthetic air* and *argon* having mass gains of 11.21% and 1.67%, respectively. The thickness of the oxide layer was also influenced and decreased stepwise from *synthetic air*, to *argon* and *CO_2*. A similar effect was observed to a lesser extent for alloy 6016 due to the lower Mg concentration, decreasing the mass gain from 2.45% when heated in *synthetic air* to 1.61% in *argon* and 0.7% in *CO_2*. The thickness of the oxide layer decreased in *argon* and increased to almost similar thicknesses in *synthetic air* and *CO_2*. The lower mass gain in *CO_2* proves that CO_2 has an inhibiting effect on the oxidation rate even for low-Mg alloys.

Keywords

Aluminum • Oxidation • TGA • DSC • Synthetic air • Argon • CO_2

Introduction

Oxidation of aluminum (Al) and its alloys is a well-known problem, generating an aluminum dross. The aluminum dross typically contains up to 70% metallic Al, causing severe losses up to 10% metallic Al [1]. To prevent and reduce these losses, several studies have over the years been performed by different research groups with the aim to inhibit the oxidation rate of Al alloys [2–5].

Behavior of Mg at Elevated Temperatures

The aluminum–magnesium (AlMg) system has been given special attention, as the Mg concentration has proven to influence the rate of oxidation of Al alloys [6–8]. As early as in 1961, Cochran and Sleppy [7] reported a significantly higher mass gain for an AlMg alloy with 2.35 wt% Mg compared to high-purity Al, and their results were later confirmed by other studies [9–11].

Mg is frequently used in Al alloys to maintain the already low weight of Al, which is attractive to the transportation and packaging industry. During the production of Al alloys with Mg as one of the most important alloying elements, challenges during the processing of the liquid melt may occur due to its high affinity to oxygen [12]. Significant fractions of the added Mg are lost due to oxidation and evaporation, as the melt is often processed at elevated temperatures, e.g. 750 °C, causing generation of oxides, e.g. MgO (magnesium oxide) and $MgAl_2O_4$ (spinel, magnesium aluminum oxide) [13, 14]. Formation of oxides was revealed by monitoring the mass gain, as the oxides, i.e. MgO (ρ_{MgO}

C. K. W. Solem (✉) · G. Tranell · R. E. Aune
Dept. of Materials Science and Engineering, Norwegian University of Science and Technology (NTNU), Trondheim, Norway
e-mail: cathrine.k.w.solem@ntnu.no

E. Solberg
Alcoa Norway ANS, Mosjøen, Norway

L. Perander (ed.), *Light Metals 2021*, The Minerals, Metals & Materials Series,
https://doi.org/10.1007/978-3-030-65396-5_97

$_{(liq)}$ = 3.58 g/cm^3) and $MgAl_2O_4$ ($\rho_{MgAl2O4(liq)}$ = 3.58 g/cm$_3$) have higher densities than both Mg ($\rho_{Mg(liq)}$ = 1.6 g/cm$_3$) and Al ($\rho_{Al(liq)}$ = 2.4 g/cm^3) [15]. However, evaporation of Mg has been demonstrated to be hindered when adding small amounts of CO_2 in the atmosphere, inhibiting the oxidation rate of the alloy [14].

The $AlMgSiO_2$ Systems

A body of work exists for the AlMg system, and an extension of the system, adding a third element, i.e. Si, has also been performed to investigate the influence on the oxidation rate [12]. In an earlier study by some of the current authors, it was reported that the AlMgSi alloy having >6 wt% Mg and >6 wt% Si oxidized rapidly in synthetic air, while a reduction in the oxidation rate was observed in an inert cover gas, i.e. in Ar [12]. When adding $\geq$5 wt% CO_2 to the atmosphere, an inhibiting effect was identified, decreasing the mass gain and the oxide layer thickness [12]. The oxide layer morphology and chemical composition had similar features as the oxides formed on an AlMg alloy, where the oxidation had been limited by CO_2 being absorbed onto the initial MgO layer, hindering further evaporation and oxidation of the alloy [12, 14]. MgO and $MgAl_2O_4$ were revealed to be the main compounds in the oxide layers. Some Mg_2Si (s) (magnesium silicide) was found to form where the activity of Al was sufficiently low [12].

The $AlMgMnO_2$ System

The AlMn alloy system is frequently used as the Mn contributes to a hardening of the alloy, making it suitable for several applications, e.g. cans and pipes. The amount of Mn added does usually not exceed 1.5 wt% as the alloy becomes too fragile, and fractures will easily arise. To increase the hardening of the alloy even more, the AlMn is alloyed with Mg. The stability diagrams for the $AlMgMnO_2$ system as a function of the O_2 (g) partial pressure and the activity of Mg (liq) and Al (liq) can be seen in Fig. 1a and b, respectively. As can be seen in Fig. 1a MgO will co-exist with AlMn, and from Fig. 1b that with an increase in the partial pressure of O_2 a phase transition of MgO to SPIN ($MgAl_2O_4$) together with AlMn-containing phases will occur at higher activities of Al (liq).

There is still a lack of knowledge in regard to the inhibiting effect obtained having small amounts of CO_2 in the atmosphere for low-Mg Al alloys containing even other alloying elements such as Si and Mn.

Experimental Procedure

In the present study, the influence of alloy composition and the inhibiting effect of CO_2 on the oxidation rate of Al alloys 5182 and 6016 (provided by Alcoa Norway ANS), i.e. AlMg4.5Mn0.35 and AlSi1.2Mg0.35, respectively, have been investigated. The samples were cut, sanded to 5 µm grid, and stored in ethanol following the same procedure as earlier reported by Solem et al. [12]

Monitoring of Mass Gain

A NETZSCH Simultaneous Thermogravimetric Analyzer (STA) model Jupiter 449 F (a DSC-TG unit) was applied to monitor the mass change and heat flux as a function of time and temperature. The polished disc samples were removed from the container with ethanol and dried in air for 30 s before heated from 25 to 750 °C with a heating rate of 10 °C/min, followed by an isothermal segment at 750 °C for 7 h, and cooled to 25 °C at the same rate (10 °C/min). Three parallels were run for each Al alloy in three different cover gases, i.e. (i) 80% *synthetic air* (20% O_2 and 80% N_2) and 20% argon, (ii) 99.999% *argon,* and (iii) 76% synthetic air (20% O_2 and 80% N_2), 20% Ar, and 4% CO_2 (from here on referred to as *synthetic air*, *argon,* and CO_2, respectively).

Surface Morphology and Elemental Mapping of Cross Section

The heat-treated disc samples from the DSC-TG experiments were further analyzed in microscope. A Zeiss Ultra model 55LE Scanning Electron Microscopy (SEM) was applied to investigate the surface morphology of the disc samples. Subsequently, the samples were mounted in epoxy, cut, and sanded to evaluate the cross sections, i.e. the oxide layer, as well as the bulk alloy. A JEOL JXA-6500F Field Emission Electron Probe Microanalyzer (EPMA) was later used to conduct elemental mapping of the cross sections, and a Zeiss Supra model 55VP SEM to perform Energy-Dispersive Spectroscopy (EDS) line scans through the oxide layer from the surface into the bulk.

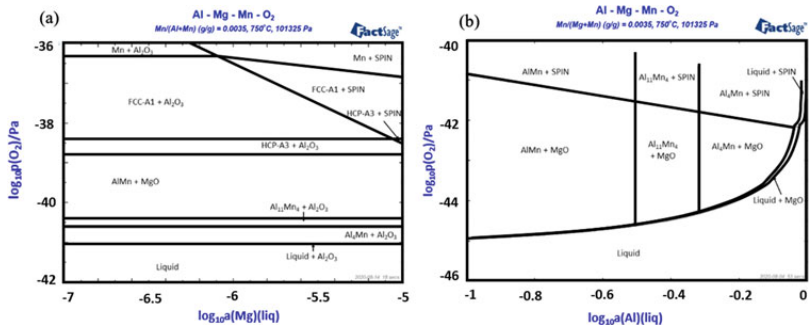

Fig. 1 Al–Mg–Mn–O_2 stability diagrams calculated as a function of the partial pressure of O_2 and the activity of **a** Mg(liq) and **b** Al(liq), respectively. Calculations were performed by the use of the FactSage 7.1 software [15]

Results

Surface Morphology

The heat-treated aluminum disc samples investigated by SEM at a magnification of 5000X showed a clear difference in surface morphologies for different alloys and cover gases, see Fig. 2. From Fig. 2a–c, it is seen, as previously reported [12], that the Al alloy 5182 revealed a granular cauliflower-shaped morphology when exposed to *synthetic air*, a finer cubic-shaped structure when exposed to *argon*, and a horizontal structure/texture when exposed to CO_2.

For the Al alloy 6016, a cauliflower-shaped surface morphology was obtained for the chosen magnification of 5000X for all three cover gases, see Fig. 2d–f.

Mass Gain (TG)

When looking at the thermogravimetric (TG) analyses from the DSC-TG experiments, seen in Fig. 3, both alloys revealed the highest mass gain when exposed to *synthetic air*. The Al alloy 5182 presented in Fig. 3a had an average mass gain (over the three parallels) of 11.21% (dotted light gray graph), 1.67% (dashed dark gray graph) and −0.30% (straight black graph) when exposed to *synthetic air*, *argon* and CO_2, respectively. The same trend in regards to a decreasing mass gain was observed for the Al alloy 6016 as well, having a mass gain in *synthetic air* of 2.45% (dotted light gray graph), in *argon* 1.61% (dashed dark gray graph), and in CO_2 0.7% (straight black graph), see Fig. 3b.

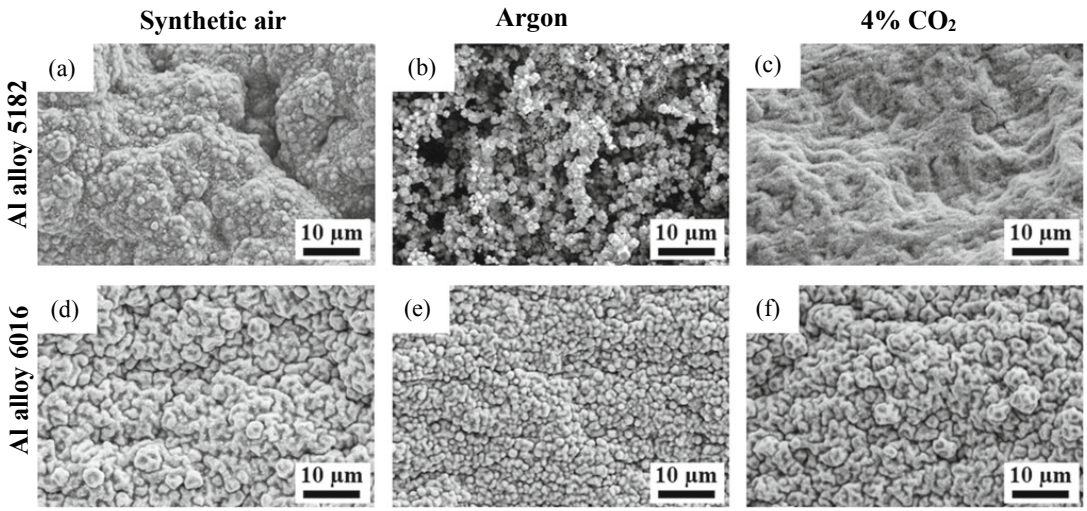

Fig. 2 Scanning Electron Microscopy (SEM) images (Mag = 5000X) of the Al alloy 5182 showing the surface morphology after heat treated at 750 °C for 7 h exposed to **a** synthetic air, **b** argon, and **c** CO_2, showing a clear difference in the surface morphology; and the heated Al alloy 6016 in **d** synthetic air, **e** argon, and **f** CO_2

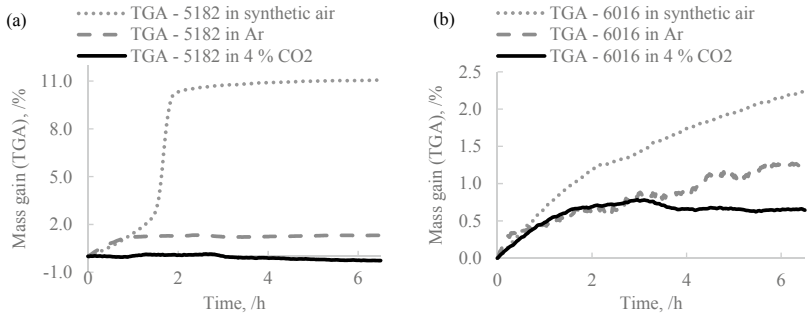

Fig. 3 The mass gain results from the DSC-TG (Differential Scanning Calorimetry–Thermogravimetric Analysis) experiments where disc samples were heated at 750 °C for 7 h in synthetic air (dotted gray graphs), Ar (dashed darker gray graphs) and 4% CO_2 (black straight graphs) for **a** Al alloy 5182 and **b** Al Alloy 6016

Cross-Sectional Evaluation

Figure 4 presents SEM images of the cross section of the resulting oxide layer in the case of heated disc samples of Al alloys 5182 and 6016 taken at a magnification of 400X. The thickness of the oxide layer in regards to the Al alloy 5182 disc samples decreased from 15–27 µm, to 14–17 µm, and 200–400 nm when the cover gas was changed from *synthetic air* to *argon* and later CO_2, see Fig. 4a–c, respectively. Phases within the bulk alloy having higher concentrations of heavier elements, e.g. Mn, were also detected. The thickness of the oxide layer in the case of the low-Mg Al alloy 6016 disc samples was determined to be 4–7 µm when exposed in *synthetic air*, ~1–2 µm in *argon,* and 3–5 µm in CO_2, respectively, see Fig. 4d–f.

Disc samples of both alloys heated in the three different cover gases were mapped by EDS from the surface through the oxide layer and into the bulk material, see Fig. 5. The line scans revealed the presence of four main elements in all samples, i.e. Al (straight white graph), O (dotted light gray graph), Mg (dashed light/dark graph), and C (long-dashed black/dark gray graph). The dashed white lines in the figure (black in Fig. 5a) have diamond ends which mark out where the line scans through the oxide layer were carried out. The general trend is that the concentration of Al decreases when the O and Mg concentrations increase. A rapid decrease

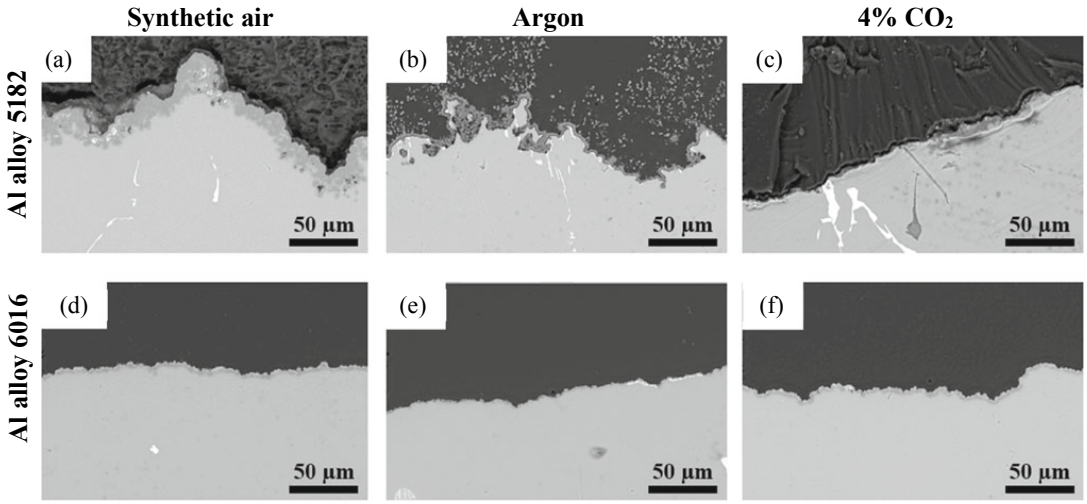

Fig. 4 SEM images (Mag = 400X) showing the oxide layer thickness (cross section) after heat treated at 750 °C for 7 h of of Al alloy 5182 in **a** synthetic air, **b** Ar, and **c** CO_2, and Al alloy 6016 in **d** synthetic air, **e** Ar, and **f** CO_2. The dark gray area is epoxy, the light area is the bulk alloy, and the interface in between is the oxide layer

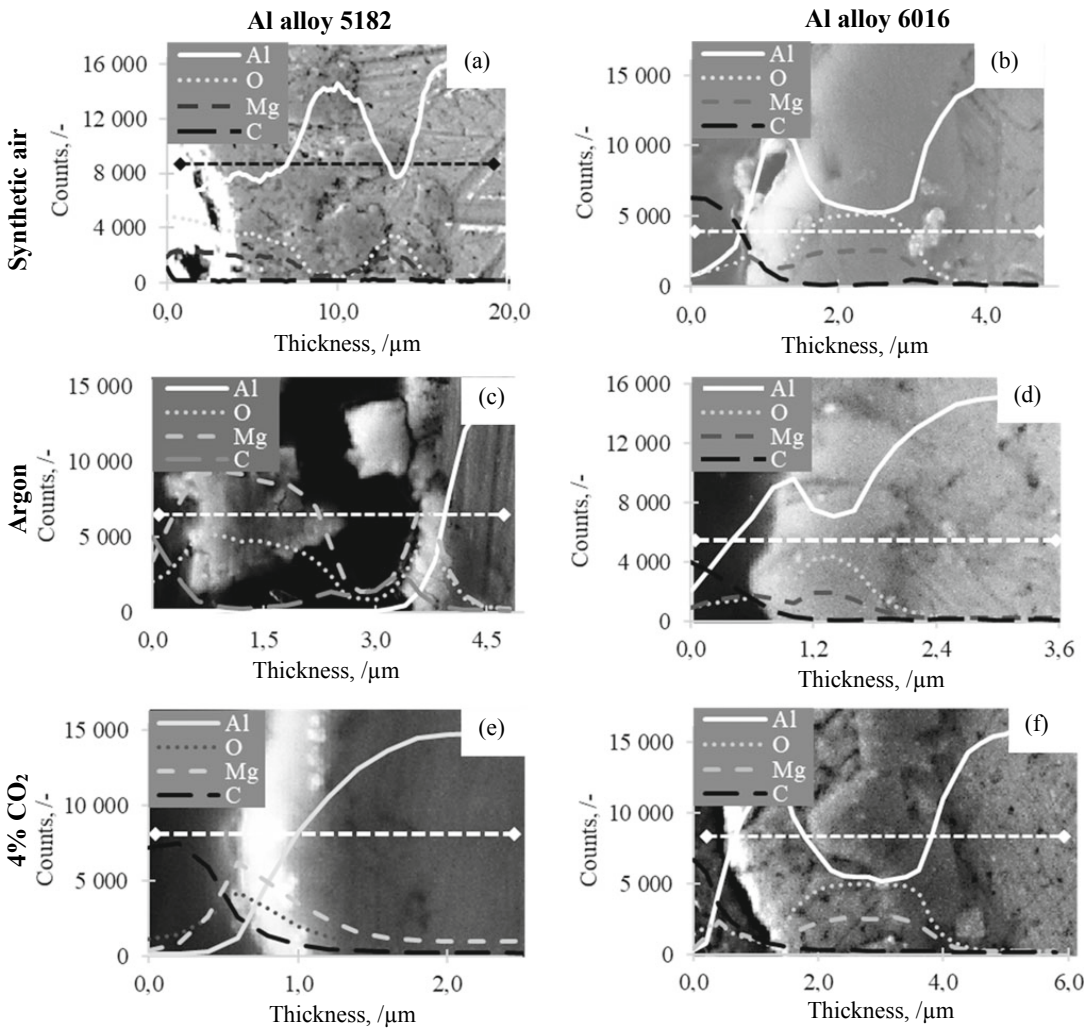

Fig. 5 Energy Dispersive Spectroscopy (EDS) line scans of the cross sections (dashed line with diamond edges) of disc samples heated at 750 °C for 7 h in **a** synthetic air (Al alloy 5182), **b** synthetic air (Al alloy 6016), **c** Ar (Al alloy 5182), **d** Ar (Al alloy 6016), **e** synthetic air and 4% CO_2 (Al alloy 5182), and **f** synthetic air and 4% CO_2 (Al alloy 6016)

from the surface through the oxide layer is also observed for C. No other elements were identified.

Each of the cross sections presented in Fig. 4 was further analyzed by EPMA. The elemental mapping of the areas presented in Fig. 4c and f can be seen in Fig. 6a and b, respectively, where special attention should be given to the differences in the scale bars for each element. The high-Mg containing Al alloy 5182 showed a homogeneous distribution of Al in the bulk metal except for in one area where no Mg and O, where found and at the sample surface where the concentrations of Mg and O again were detected. Mn was mapped to be in the bulk metal together with higher concentrations of Al, Si, and Fe (some of the elemental mappings are presented in Fig. 6a). The low-Mg containing Al alloy 6016 showed a lower concentration of Al at the sample surface together with higher concentrations of Mg and O. The Si was mapped to be homogeneously distributed in the bulk together with the Al, except for in a concentrated area at the sample surface where the Si concentration was significantly higher, see Fig. 6b.

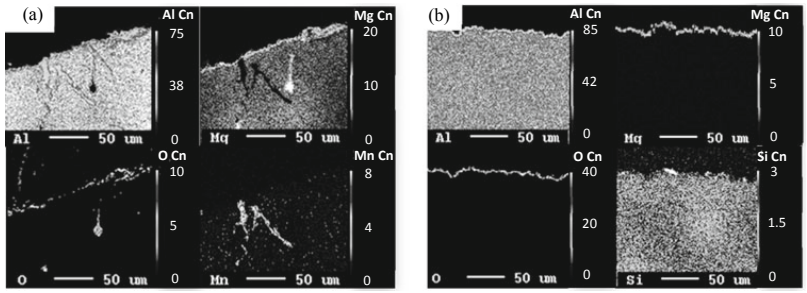

Fig. 6 Electron Probe Micro Analyses (EPMA) of the cross sections presented in Fig. 4c and f after being heat treated at 750 °C for 7 h in 4% CO_2. **a** elemental mapping of Al, Mg, O, and Mn in the case of the Al alloy 5182, where the Mn-rich phase also contains Fe and Si and **b** Al, Mg, O, and Si in the case of Al alloy 6016

Discussion

The Al Alloy 5182

The surface morphologies revealed in SEM for the Al alloy 5182 proved to be similar to what has been reported in literature for high-Mg containing Al alloys [12], i.e. a cauliflower-shaped structure, finer cubes, and a horizontal texture for the disc samples exposed in *synthetic air*, *argon*, and CO_2, respectively, as presented in Fig. 2a–c. This implies that the concentration of Mg had a stronger influence on the overall structure than the absence of Si and/or Mn in the alloy. Another similarity was found in the mass gain, as an inhibiting effect was observed for *argon* and even a greater effect for CO_2, see Fig. 3a. The same observation was also confirmed when the cross sections were investigated, as the thickness of the oxide layer decreased from 15–27 µm to 14–17 µm and to 200–400 nm when changing the cover gas from *synthetic air* to *argon* and CO_2, respectively, see Fig. 4a–c. The EDS line scan for the Al alloy 5182 confirmed the same decrease in the thickness of the oxide layer, as well as a decrease in the Al concentration through the oxide layer when the Mg and O concentrations increased for all three cover gases, however, differences in the concentrations of each of the elements presented in the mapping were found for all the three cover gases.

When exposed to *synthetic air*, the combination of Al, Mg, and O present in the oxide layer has earlier been reported as a two-step breakaway oxidation. This phenomenon could not be confirmed in the case of the disc samples exposed to *synthetic air*, however, a big one-step mass gain was revealed, see gray dotted graph in Fig. 3a. Due to the presence of Al, as can be seen in Fig. 5a, it is believed that the formation of MgO to $MgAl_2O_4$ has occurred as a result of the breakaway oxidation, resulting in one significant mass gain step of 11.21%. This assumption is strengthened even further when looking at the stability diagram of the system Al–Mg–Mn–O_2 presented in Fig. 1b, where the stable phase together with the liquid phase reacts from MgO to SPIN ($MgAl_2O_4$) when the partial pressure of O_2 increases. It is, however, not believed that the phases Al_4Mn, $Al_{11}Mn_4$, or AlMn are present, as no Mn was detected through the oxide layer by EPMA nor found by EDS.

When the Al alloy 5182 was heated in *argon*, the EDS line scan and element mapping revealed nearly no Al present in the granular oxide layer, presented as one big particle in Fig. 5c. The line scan indicated that there was only MgO present in the granular and dense oxide layers. The EPMA results supported these observations. Further oxidation from MgO to $MgAl_2O_4$ has therefore seemingly not taken place. This is confirmed by the dashed dark gray TG curve in Fig. 3a, where *argon* seems to have had a limiting effect on the mass gain, i.e. on the oxidation rate compared with *synthetic air*, lowering the mass gain to 1.61%.

The EDS line scan for the heated disc samples of the Al alloy 5182 in CO_2 revealed a rapid increase of Mg and O in the oxide layer, which linearly decreased as a function of depth into the sample. The concentration of Al increased slowly at first as the Mg and O concentrations increased quickly, followed by a rapid increase as a result of a decrease in the Mg and O concentration. The trends of Mg, O, and Al is confirmed by the EPMA results, where the oxide layer is depleted in Al and concentrated in Mg (continuous layer) and O (discontinuous layer), see Fig. 6a. It was also revealed by the EPMA results that the bulk had a homogeneous distribution of Mg, as well as mapping a concentrated Mg layer at the surface, revealing that the diffusion and evaporation of Mg must have been hindered, see Fig. 6a. From the TG results in Fig. 3a it is clear that small

additions of CO_2 in the cover gas has had a significant inhibiting effect, however, some of the Mg has evaporated from the surface as the average mass gain was found to be negative, i.e. a mass loss of 0.30%.

The Al Alloy 6016

The low-Mg containing Al alloy 6016 did not seem to be as affected by the different cover gases in regard to changes in the surface morphology as the high-Mg containing Al alloy 5182. The morphology of the heated disc samples revealed a cauliflower-shaped structure regardless of the cover gas, see Fig. 2d–f, respectively. Limited differences between the heated disc samples were again recognized when looking at the cross sections, revealing thicknesses of the oxide layers of 4–7, ~1–2, and 3–5 µm for *synthetic air*, *argon*, and *CO_2*, respectively, as presented in Fig. 4d–f. Key differences were first observed when looking closer at the TG results in Fig. 3b.

It was clear that this alloy had only oxidized to some extent during exposure to *synthetic air* (Fig. 3b, dotted gray graph), revealing a mass gain of 2.45%, explaining why the thickness of the oxide layer was identified to be only 4–7 µm. The EDS line scan in Fig. 5b revealed a higher concentration of Al at the surface, which decreased as the concentrations of O and Mg increased. When reaching the bulk metal, the Al concentration increased again, while the O and Mg concentrations decreased. The presence of Al and MgO at the surface of the disc samples are under the present conditions consistent with the observations made from the stability diagram of Al–Mg–O_2–Si [12]. When the partial pressure of O_2 increases in the oxide layer, as seen in Fig. 5b dashed gray graph, the MgO reacts to form $MgAl_2O_4$. Finally, when reaching the bulk, the concentrations of O and Mg decrease again. No Si was detected by the EDS line scan through the oxide layer, which later were confirmed by EPMA, showing a depletion of Si at the metal surface except for the formation of small clusters, and a homogeneous distribution in the bulk. As EPMA is conducted at a magnification of only 400X, it is believed that the EDS line scan has been carried out in an area depleted in Si.

It was established that *argon* had a limiting effect on the oxidation rate, decreasing the mass gain to 1.61%. Even though an inhibiting effect was identified, the Al alloy 6016 did not reach steady state for neither *synthetic air* nor *argon*, as the mass gain continued to increase even after an isothermal segment of 7 h. As previously mentioned, it was clear from the SEM images that the oxide layers were relatively equal in thickness, regardless of cover gas, and this was again confirmed by the EDS line scans analyzing a different area of the same disc sample. Figure 5d shows the elemental mapping through the line scan for the Al alloy 6016 disc sample heated in *argon*, and the same behavior was observed as for the sample heated in *synthetic air*, i.e. the concentration of oxygen first decreases, for later to increases and then decreases again from the surface through the oxide layer into the bulk. Stability diagrams from the literature [12] indicate the formation of MgO at the surface, followed by the formation $MgAl_2O_4$ before reaching the bulk where it is expected that the partial pressure of O_2 is close to zero. The EPMA confirms the behavior of Al, O, and Mg, as well as a depletion of Si at the surface, explaining why Si was not mapped by EDS.

An inhibiting effect on the oxidation rate was obtained when adding CO_2 to synthetic air in regards of mass gain, however, a thicker oxide layer was revealed when investigating the cross section by EDS, see Fig. 5f. The increase in the magnification identified the oxide layer to be around twice as thick as for the disc samples heated in *argon*, and the EDS line scan revealed a behavior more like the disc samples heated in *synthetic air*. When looking at the morphology revealed by the EDS line scan, it is observed that the oxide layer is divided into two different layers, i.e. a continuous layer on top of a layer of particles. This may be why the oxide layer is identified to be as thick, although, having a low mass gain, as the particles are only half the size of the particles identified in the oxide layer of the disc samples heated in *synthetic air*. As the density of Al (liq) is lower than the density of both MgO (liq) and $MgAl_2O_4$ (liq), it is believed that the CO_2 in the cover gas has had an inhibiting effect and thereby to some extent prevents evaporation of Mg and further oxidation, resulting in a lower mass gain of only 0.7%.

Overall Discussion

As expected, the high-Mg containing Al alloy 5182 had a higher rate of oxidation than the low-Mg containing Al alloy 6016. Due to the evaporation of Mg, and O having a higher affinity to Mg than Al, it was clear from the presently obtained results that the oxidation rate was faster when the concentration of Mg was higher. A slower oxidation rate was identified when the concentrations of Mg decreased, as steady state was not reached for the Al alloy 6016 neither when exposed to *synthetic air* nor *argon*. Even though the mass gain was 11.21% for the Al alloy 5182 and only 2.45% for the Al alloy 6016, the mass gain after 7 h in *argon* was relatively similar, i.e. 1.67% and 1.61%, respectively, indicating that the Mg concentration did not have a significant effect in an inert cover gas. An increase in the isothermal

segment may influence the mass gain, as the Al alloy 5182 disc samples reached a steady state for all cover gases in question, however, the Al alloy 6016 disc samples did not.

Diffusion of Mg towards the surface during heating was observed for all disc samples investigated in the present study, except for the Al alloy 5182 heated in CO_2 revealing a homogeneous distribution of Mg in the bulk, strengthening the theory that the Mg concentration together with the CO_2 has a significant role in obtaining an inhibition of the oxidation rate. However, as all of the Mg in the Al alloy 6016 had diffused from the bulk to the surface during heating in *synthetic air* and CO_2, and even then lowered the mass gain from 2.45 to 0.7%, it is believed that even a lower Mg concentration in combination with additions of small amounts of CO_2 in the cover gas had an inhibiting effect. Further investigations of the absorption of CO_2 on the oxide layer, e.g. MgO, is needed to evaluate how it behaves together with low- and high-Mg containing Al alloys, as it in the present study was challenging to distinguish between the C from the epoxy and the C adsorbed from the CO_2 present in the cover gas.

Conclusion

The influence of the Mg concentration and the inhibiting effect of CO_2 on the oxidation rate of aluminum has been investigated for Al alloys 5182 and 6016, by heating disc samples of the alloys to 750 °C and exposing them to three different cover gases during 7 h, i.e. (i) 80% *synthetic air* and 20% argon, (ii) 99.999% *argon*, and (iii) 76% synthetic air, 20% argon and 4% CO_2.

The present study confirmed that small additions of CO_2 to the oxidizing atmosphere had a significant inhibiting effect on the oxidation rate in the case of the high-Mg containing Al alloy 5182. The mass gain and thickness of the oxide layer decreased from 11.21% and 15–27 µm during exposer in *synthetic air* to −0.30% and 200–400 nm when additions of 4% CO_2 was added to the synthetic air. A phase transition from MgO and $MgAl_2O_4$ was identified to take place in the oxide layer inhibiting further evaporation of Mg. Mn was identified together with Al and Fe/Si as intermetallic phases in the bulk alloy, but not in the oxide layer.

A similar inhibiting effect of CO_2 was observed for the low-Mg containing Al alloy 6016, but to a lesser extent. In this case, the mass gain decreased from 2.45 to 0.7%, however, the thickness of the oxide layer itself did not decrease. A two-layered oxide deposit was identified, where the CO_2 together with the host metal had hindered further oxidation of the continuous MgO layer identified underneath the oxide layer. The Si clusters detected at the surface and the Si homogeneously distributed in the bulk alloy did not influence the oxidation rate.

Future Work

Future work includes the continuation of the analyses of the oxide layers, e.g. X-Ray Diffraction (XRD), to evaluate the phases generated as a result of exposing the disc samples to different cover gases. The isothermal segment will be increased with the aim of reaching steady state for all the cover gases in question in regard to mass gain. Moreover, different sample preparation and analysis methods will be tested to improve the mapping of C through the oxide layer.

Acknowledgements This publication has been funded by the SFI Metal Production (Centre for Research-based Innovation, 237738). The authors gratefully acknowledge the financial support from the Research Council of Norway and the partners of the SFI Metal Production.

References

1. Kos B (1995) Improvement of the metal recovery from dross by centrifuging of hot dross. In: Proceedings: Conference: 3. International Symposium on Reycling of Metals and Engineered Materials, Point Clear, AL (United States). ISBN 0-87339-318-X
2. Belitskus DL (1971) Oxidation of molten Al-Mg alloy in air, air-SO_2, and air-H_2S atmospheres. Oxid Met 3:313–317. https://doi.org/10.1007/BF00614625
3. Bergsmark E, Simensen CJ, Kofstad P (1989) The oxidation of molten aluminum. Materials Science and Engineering: A 120–121:91–95.https://doi.org/10.1016/0921-5093(89)90723-5
4. Smith N, Kvithyld A, Tranell G (2018) The Mechanism Behind the Oxidation Protection of High Mg Al Alloys with Beryllium. Metall and Materi Trans B 49:2846–2857.https://doi.org/10.1007/s11663-018-1340-6
5. Cochran CN, Belitskus DL, Kinosz DL (1977) Oxidation of aluminum-magnesium melts in air, oxygen, flue gas, and carbon dioxide. MTB 8:323–332.https://doi.org/10.1007/BF02657663
6. Surla K, Valdivieso F, Pijolat M, et al (2001) Kinetic study of the oxidation by oxygen of liquid Al–Mg 5% alloys. Solid State Ionics 143:355–365.https://doi.org/10.1016/S0167-2738(01)00861-X
7. Cochran CN, Sleppy WC (1961) Oxidation of High-Purity Aluminum and 5052 Aluminum-Magnesium Alloy at Elevated Temperatures. J Electrochem Soc 108:322–327.https://doi.org/10.1149/1.2428080
8. Do T, McIntyre NS, van der Heide PAW (1999) The oxidation kinetics of Mg-, Si- and Fe-implanted aluminum by using X-ray photoelectron spectroscopy. Surface Science 433–435:765–769. https://doi.org/10.1016/S0039-6028(99)00488-4
9. Schoenitz M, Dreizin E (2012) Oxidation Processes and Phase Changes in Metastable Al-Mg Alloys. Journal of Propulsion and Power.https://doi.org/10.2514/1.9024
10. Haginoya I, Fukusako T (1983) Oxidation of Molten Al–Mg Alloys. Trans JIM 24:613–619.https://doi.org/10.2320/matertrans1960.24.613
11. Hinton EM, Griffiths WD, Green NR (2013) Comparison of Oxide Thickness of Aluminium and the Effects of Selected Alloying Additions. MSF 765:180–184.https://doi.org/10.4028/www.scientific.net/MSF.765.180
12. Solem CKW, Ekstrøm KE, Tranell G, Aune RE (2020) Evaluation of the Effect of CO2 Cover Gas on the Rate of Oxidation of an AlMgSi Alloy. In: Tomsett A (ed) Light Metals 2020. Springer International Publishing, Cham, pp 1141–1147

13. Czerwinski F (2004) The early stage oxidation and evaporation of Mg–9%Al–1%Zn alloy. Corrosion Science 46:377–386.https://doi.org/10.1016/S0010-938X(03)00151-3
14. Smith N, Gleeson B, Saidi WA, et al (2019) Mechanism behind the Inhibiting Effect of CO2 on the Oxidation of Al–Mg Alloys. Ind Eng Chem Res 58:1434–1442. https://doi.org/10.1021/acs.iecr.8b04691
15. FactSage version 7.1 by Thermfact and GTT-Technologies

Paper 3

Heat Treatment of Mg-Containing Aluminum Alloys 5182 and 6016 in an Oxidizing Atmosphere with 4% CO_2

Cathrine Kyung Won Solem, Per Erik Vullum, Gabriella Tranell, and Ragnhild E. Aune

Abstract

Oxidation of liquid aluminum (Al) during processing is a widely known problem, and magnesium (Mg), as a common alloying element, increases the oxidation rate of the alloy. It has been established that small additions of CO_2 ($\geq$ 4%) in an oxidizing atmosphere have a significant inhibiting effect on the rate of oxidation of Al alloys 5182 (AlMg4.5Mn0.4) and 6016 (AlSi1.2Mg0.4) discs based on oxide layer thickness and mass gain when heat-treated at 750 °C for 7 h. The phases present in the oxide layers for each alloy have now been identified and compared with discs heated in synthetic air and argon (Ar) under the same experimental conditions. The XRD analyses revealed the presence of MgO for all Al alloy 5182 discs, in addition to $MgAl_2O_4$ and Al_2O_3 when heated in synthetic air, and Mg_2C_3 when heated in the mixed cover gas containing 4% CO_2. The low Mg-containing Al alloy 6016 revealed the presence of $MgAl_2O_4$ for all discs, in addition to MgO when heat-treated in the mixed cover gas containing 4% CO_2, as well as Al_2O_3 when heated in Ar. For both alloys, Transmission Electron Microscopy (TEM) combined with Energy Dispersive X-ray Spectroscopy and Electron Energy Loss Spectroscopy (EDS-EELS) analyses revealed that the mixed cover gas also resulted in a nanometer-thin amorphous C layer, never previously detected, on top of the thin nanocrystalline MgO layer, retarding the evaporation of Mg and inhibiting the oxidation rate for both alloys.

Keywords

Aluminum • Oxidation • MgO • CO_2

Introduction

Aluminum (Al) and its alloys are a necessity in modern society and as today's second most important metal, Al is on its road to becoming an even more sustainable and renewable material [1]. Challenges related to production and processing of Al, i.e. oxidation and metal loss, have been a topic of interest for over a century [2] and several studies have been carried out trying to understand the overall mechanisms of oxidation of Al and typical alloying elements like Mg [2–4]. Even the behavior and onset of breakaway oxidation leading to the formation of less protective phases such as spinel ($MgAl_2O_4$) in the case of Mg-containing Al alloys have been studied in detail [2–4].

Inhibition of Oxidation by CO_2

The literature contains several studies in regard to inhibition of the oxidation of Al, as well as how the rate of oxidation may be delayed and hindered [5–7]. Based on these studies, it has been established that the chemical composition and the oxidizing atmosphere are parameters influencing the system. An example is the case of Al–Mg alloys, where it has been established that the Mg content influences the rate and extent of oxidation, which may be inhibited if the oxidation step forming MgO is retarded [8–10].

It is a well-known fact that as the Gibbs energy of formation for MgO is lower than for Al_2O_3, the oxygen present in the atmosphere generates MgO as the stable phase. It was, however, demonstrated by Smith et al. in 2019 that small additions of CO_2 in the oxidizing atmosphere of Al–Mg systems had a significant influence in regards to the rate of

C. K. W. Solem (✉) · G. Tranell · R. E. Aune
Department of Materials Science and Engineering, Norwegian University of Science and Technology (NTNU), Trondheim, Norway
e-mail: cathrine.k.w.solem@ntnu.no

P. E. Vullum
Department of Physics, Norwegian University of Science and Technology (NTNU), Trondheim, Norway

P. E. Vullum
SINTEF Industry, Trondheim, Norway

D. Eskin (ed.), *Light Metals 2022*, The Minerals, Metals & Materials Series,
https://doi.org/10.1007/978-3-030-92529-1_77

oxidation [10]. It was observed in their study that the CO_2 in the cover gas was adsorbed on top of the MgO layer formed on the surface of the Al–Mg alloy, preventing further diffusion of Mg through the MgO layer, hence, inhibiting the rate of oxidation [10]. Similarly, CO_2 has been studied and found to have an important role in aqueous solutions, preventing oxidation and corrosion of Mg alloys due to the formation of insoluble products acting as a protecting film on the surface [11].

Several mechanisms on how the CO_2 and MgO surfaces interact have been proposed, and the behavior of CO_2 when physiosorbed, e.g. adsorbed to the surface by van der Waals forces at an already existing MgO surface, has also been investigated by Tosoni et al. [12]. Based on their findings, they suggest that a carboxylate complex or a carbonate, i.e. CO_2- or $CO_3{}^2-$, may be the compounds present on the MgO surface. Alkali earth metal oxides in general, e.g. MgO and CaO, have been reported to be suitable recipients to CO_2 [13], however, only for specific crystal orientations, e.g. orientation (100) in the case of MgO.

The present authors have previously studied the oxidation steps experienced by Al–Mg alloys in the casthouse during Al production, by exposing high and low Mg-containing alloys to different cover gases in controlled laboratory environments [9]. In this study, Al discs of the alloys 5182 (AlMg4.5Mn0.4) and 6016 (AlSi1.2Mg0.4) were heat-treated at 750 °C for 7 h in three different cover gases: (i) 80% synthetic air and 20% Ar, (ii) 99.999% Ar, and (iii) 4% CO_2, 76% synthetic air, and 20% Ar, referred to as synthetic air, Ar, and mixed cover gas containing 4% CO_2, respectively [9]. For each alloy, three parallel disc samples were heat-treated and later analyzed by Scanning Electron Microscope (SEM), Energy Dispersive X-ray Spectroscopy (EDS), and Electron Probe Micro Analyses (EPMA) to identify the surface morphology and the microstructure of the cross sections, as well as the chemical composition of the cross sections.

For the discs heat-treated in synthetic air, $MgAl_2O_4$ was established to have been formed in the case of the high Mg-containing Al alloy 5182, and MgO together with $MgAl_2O_4$ for the low Mg-containing Al alloy 6016. When heat-treated in pure Ar, however, a change in the elements present was observed for the Al alloy 5182 as only MgO was found to have been formed, however, both MgO and

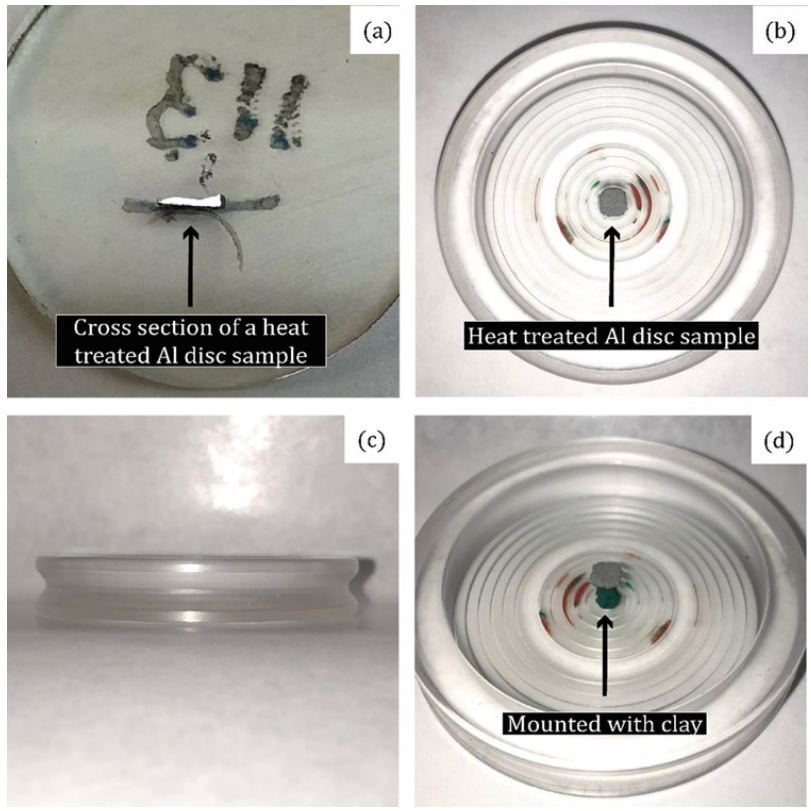

Fig. 1 Sample preparation of heat-treated Al alloy discs, where **a** shows a cross section of a disc mounted in epoxy resin, and **b**–**d** show a sample mounted by clay in a deep sample holder (inner diameter 45 mm), seen from above, the side, and at an angled view

$MgAl_2O_4$ for the Al alloy 6016 were still present. For the disc samples heat-treated in the mixed cover gas containing 4% CO_2, it was difficult to establish a clear interphase between then top layers. It was, however, revealed higher concentrations of Mg and O close to the surface, but not on the very top surface, for both alloys. Based on the analyses, it was confirmed that small additions of CO_2 in an oxidizing atmosphere had an inhibiting effect on the oxidation rate in regard to the mass gain, as well as for the oxide layer thicknesses. It was challenging to investigate the overall mechanism of the inhibiting effect of the CO_2 and where the C had deposited due to the C-bonded chemicals in the epoxy resin used during sample preparations, see Fig. 1a. In the present study, other characterization techniques will therefore be applied trying to study how the CO_2 behaves for both Al alloy systems.

Experimental Procedure

X-Ray Diffraction (XRD)

All heat-treated Al discs from previous work [9] of both alloys were examined by a D8 A25 DaVinci X-Ray Diffractometer (Bruker, Billerica, Ma, USA) to verify and confirm the previously obtained results by micrographic analyses. The oxidized discs were mounted in a deep sample holder with the use of clay, and it was made sure that the surface was parallel to the edge of the sample holder, see Fig. 1b–d. Monochromatic CuKα photons with a wavelength of $\lambda = 1.54060$ Å were used during the XRD scans. Each diffraction pattern was acquired with a step size of 0.013° and covered scattering angles 2θ over the range 10–85°. The TOPAS (v5, Bruker Billerica, Ma, USA) software was used for the refinement of the results, using the Powder Diffraction Files (PDFs) from the ICDD-4 + PDF-database.

Transmission Electron Microscopy (TEM)

The Al discs heat-treated in the mixed cover gas containing 4% CO_2, were further examined with the aim of identifying the role of CO_2 and its inhibiting effect on the rate of oxidation of Al alloys 5182 and 6016.

To avoid sample charging in the dual-beam Focused Ion Beam (FIB), a Cressington sputter coater was used to deposit a thin electrically conducting layer of Pt–Pd (80:20) on top of the Al alloy 5182 disc. No pre-coating was applied for the Al alloy 6016 disc sample. Subsequently, a Helios G4 UX FIB (FEI, Hillsboro, Or, USA) was used to prepare the TEM lamellae. The oxidized discs from both alloys were coated with two layers of C, of which the first layer was made by electron beam-assisted deposition, and the second by Ga^+ ion-beam-assisted deposition. An accelerating voltage of 30 kV was initially applied during the coarse thinning. Final thinning was first done at 5 kV, before decreasing the voltage stepwise to 2 kV of either side of the TEM lamellae to minimize surface damage. Due to the characteristics of the precursor gas used during the carbon deposition, i.e. Naphthalene ($C_{10}H_8$), the amorphous carbon–hydrogen composite layer is easy to distinguish from any pure C layer that may originate from the CO_2 atmosphere.

A double spherical aberration-corrected Cold FEG JEOL ARM200FC microscope (JEOL Ltd., Tokyo, Japan), operated at 200 kV was used for the TEM analyses. Energy Dispersive X-ray Spectroscopy (EDS) and Electron Energy Loss Spectroscopy (EELS) were applied simultaneously using the Scanning Transmission Electron Microscopy (STEM) mode. The light elements such as C and O were better detected by EELS, while the heavier elements such as Al gave better results using the EDS. All STEM images were taken using a High-Angle Annular Dark-Field (HAADF) mode to secure both precision and accuracy of the profiling.

Table 1 Phases identified by X-Ray Diffraction (XRD) of aluminum (Al) alloys 5182 and 6016 heat-treated in three different cover gases

Al alloy	Cover gas	Phases present					
		Al	MgO	$MgAl_2O_4$	$Mg_{0.388}Al_{2.408}O_4$	Al_2O_3	Mg_2C_3
5182	(i) 80% synthetic air, 20% Ar	x	x	x	x	x	
	(ii) 99.999% Ar	x	x				
	(iii) 4% CO_2, 76% synthetic air, 20% Ar	x	x				x
6016	(i) 80% synthetic air, 20% Ar	x		x			
	(ii) 99.999% Ar	x	x	x		x	
	(iii) 4% CO_2, 76% synthetic air, 20% Ar	x	x	x			

Results and Discussion

Characterization by XRD

A complete overview of the phases identified by XRD for both Al alloys 5182 and 6016 in the case of all three cover gases used in the present study is presented in Table 1. As can be seen from the table, the XRD analyses confirm the observations from previous analyses obtained by EDS and EPMA reported elsewhere by the present authors [9].

For the high Mg-containing Al alloy 5182 heat-treated in synthetic air, MgO (magnesium oxide) and $MgAl_2O_4$ (spinel), as well as $Mg_{0.388}Al_{2.408}O_4$ (defect spinel) and Al_2O_3 (aluminum oxide), were identified to have been formed, and cubic MgO crystals and Al when heat-treated in Ar. It is believed that for the disc sample heat-treated in Ar, the oxidation process of MgO reached steady-state conditions, as the partial pressure of O_2 was not sufficient to cause breakaway oxidation at 750 °C when the holding time was restricted to 7 h, as seen for the disc sample heat-treated in synthetic air. For the disc sample heat-treated in the mixed cover gas containing 4% CO_2, cubic MgO crystals were identified to have been formed by the XRD analysis, in addition to small amounts of Mg_2C_3 (magnesium carbide). It is in this case believed that a rougher surface with clear defects might have caused splitting of the CO_2 molecules and therefore caused Mg_2C_3 and O_2 to further react with the Mg vacancies present in the system forming other Mg, Al, and O containing phases. It was, however, not identified neither $MgAl_2O_4$, $Mg_{0.388}Al_{2.408}O_4$ nor Al_2O_3 by the XRD to have been formed, which is believed to be due to the formation of a protective C layer resulting from the CO_2 present in the cover gas, delaying any diffusion of O_2 and potential oxidation reactions.

For the low Mg-containing Al alloy 6016 heat-treated in synthetic air, only $MgAl_2O_4$ was identified to have been formed, which is believed to be due to complete breakaway oxidation, i.e. the MgO from the first oxidation step continues to oxidize with Al forming $MgAl_2O_4$. This correlates partly with previous findings, as no mapped areas with only Mg and O indicating the formation of MgO were reported from Solem et al. [9]. When heat-treated in Ar, however, MgO was detected together with $MgAl_2O_4$ and Al_2O_3, indicating that the breakaway oxidation has partly occurred. For the disc sample heat-treated in the mixed cover gas containing 4% CO_2, MgO and $MgAl_2O_4$ were identified to have been formed, revealing the absence of magnesium carbides. It is believed that all of the small amounts of Mg present in the alloy were oxidized and partly caused breakaway oxidation.

Due to the challenges with identifying the influence of CO_2, further analysis of both Al alloys 5182 and 6016 discs heat-treated in the mixed cover gas containing 4% CO_2 was Carried out to investigate the layers and phases present.

Microscopy Analyses through TEM

To further evaluate the phases present in the oxidized Al alloy discs 5182 and 6016 heat-treated in the mixed cover gas containing 4% CO_2, FIB followed by TEM and EDS-EELS analyses was carried out.

In Fig. 2a, the cross-section lamella made by FIB of the high Mg-containing Al alloy 5182 disc is presented. As can be seen from the figure, the deposited C layers, resulting from the sample preparation, were identified together with the Pt-Pd coating used to avoid sample charging. When looking further at the cross section of the sample itself, it is seen that there are MgO crystals (light gray crystals marked by purple box and arrows) present in the Al bulk (dark gray areas marked by green box). Closer to the surface, a dense, continuous nanocrystalline MgO layer can also be seen, confirming not only previously reported EDS and EPMA results [9, 10] but also the presently obtained XRD results.

On top of the nanocrystalline MgO layer, a thin continuous layer of amorphous C, which has never been previously observed, was detected, as seen in the TEM image in Fig. 2b, where the interface between the amorphous C layer and the nanocrystalline MgO layer is marked with a white solid line. The same C layer was found, but to a lesser extent for the low Mg-containing Al alloy 6016 disc. This correlates well with findings reported by the present authors and others, where it is believed that the CO_2 present in an oxidizing atmosphere may be absorbed on top of MgO crystals, and form a protective layer preventing further evaporation of the Mg and inhibiting the oxidation rate [10, 14].

STEM EDS-EELS analysis of the cross section was performed for both alloys to further evaluate the elements present in the oxide layers, as well as the C layer. A cross section of the Al alloy 5182 disc is presented in Fig. 3a, showing the HAADF STEM image of the Al bulk (bottom grey area), the nanocrystalline MgO layer covered by a continuous amorphous C layer, as well as the thin Pt-Pd coating (bright contrast layer on top of the amorphous C layer) and the protective C coating (black contrast due to the combination of the light elements of C and H). A combination of EDS and EELS analyses was used, where C, Mg, and O were mapped by EELS and Al by EDS.

Figure 3b–d shows the EDS-EELS results of the mapped elements of interest for the Al alloy 5182 disc. As can be seen in Fig. 3b from the mapping of C, a 40–100 nm continuous C layer is revealed close to and at the surface of the sample. As the HAADF STEM imaging procedure takes place with a contrast scale close to the atomic number

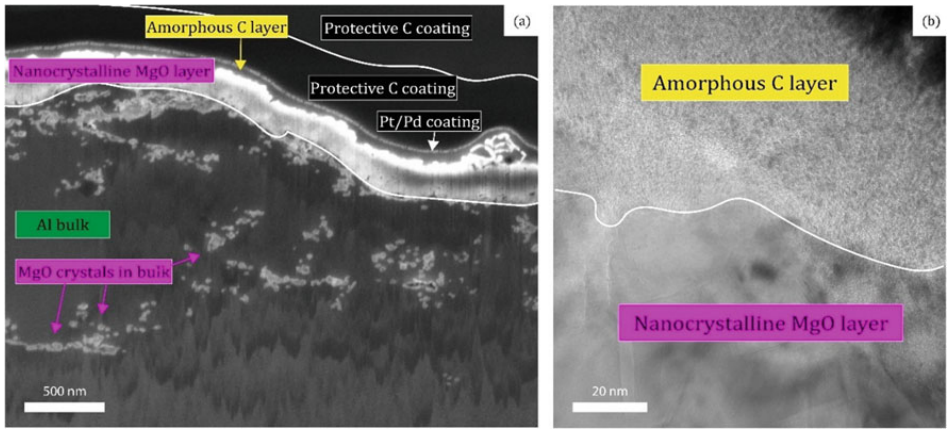

Fig. 2 Cross section of the Al alloy 5182 where **a** shows a Secondary Electron Microscopy (SEM) image of the disc sample after preparation by Focused Ion Beam (FIB), and **b** bright field Transmission Electron Microscopy (TEM) image of the interface between the amorphous C layer and the nanocrystalline MgO layer

squared, z_2 and the fact that the carbon protection layer consists of a mixture of hydrogen and carbon ($C_{10}H_8$), the deposited layer appears with a brighter contrast than the amorphous C layer that is originating from the sample surface itself. The EELS analyses of Mg and O presented in Fig. 3c and Fig. 3d, respectively, revealed the existence of a 200–400 nm thick layer of nanocrystalline MgO before reaching the Al bulk as seen in Fig. 3e. A heterogeneous distribution of MgO particles was also found to be present in the bulk of the disc sample.

With respect to the amorphous C layer on top of the nanocrystalline MgO layer, a similar layered structure was recognized for the low Mg-containing Al alloy 6016. A layer in the range of 15–120 nm of the thin amorphous C layer was identified on the top of a 160–200 nm thin nanocrystalline MgO layer. No individual MgO particles in the Al bulk were found to exist in the bulk of the disc sample, however, large (≤ 2 μm) $MgAl_2O_4$ particles were found by STEM-EELS-EDS close to the MgO layer as a discontinuous oxide layer.

Overall Discussion

Based on the presently obtained XRD and TEM results, it is believed that the amorphous nanometer-thin C layer, identified to exist for both Al alloy discs after heat-treated in a mixed cover gas containing 4% CO_2, has an inhibiting effect on the rate of oxidation of both Mg and Al. The overall Mg concentration is also believed to play a key role in this process, as it clearly influences the thickness of the oxide layer, as well as the phases eventually formed.

Figure 3f summarizes the mapping of the Al alloy 5182 disc by color, where C, Mg, O, and Al are represented by the colors yellow, red, blue, and green, respectively, giving MgO the color of purple. As can be seen from the figure, the presence of the nanocrystalline MgO layer, as well as the MgO particles in the bulk, correlates well with the XRD results for the same sample, as only MgO was identified to have formed during heat treatment in the mixed cover gas containing 4% CO_2. As for the Al alloy 6016 disc, $MgAl_2O_4$ was identified to have been formed by both XRD and TEM.

Moreover, the EELS analysis confirmed the formation of an amorphous nanometer-thin layer of C covering the nanocrystalline MgO layer. It is believed that the standard sample preparation technique applied and the use of epoxy resin containing C-bonded chemicals have made it difficult to identify the presence of the C layer during earlier investigations.

In the case of the Al alloy 6016, it is believed that the lower Mg concentration resulted in the formation of a thinner MgO layer. After reaching steady state conditions, the formation of $MgAl_2O_4$ took place, i.e. breakaway oxidation, before the amorphous C layer inhibited any further oxidation of MgO. As for the Al alloy 5182, the first oxidation step of Mg is believed not to have reached steady state before the inhibiting C layer was established, thus, no breakaway oxidation was identified to exist. Based on this, it is believed that for both Al alloys, the amorphous C layer formed on top of the MgO oxide layer seems to inhibit the evaporation of Mg, hence, delaying the overall rate of oxidation.

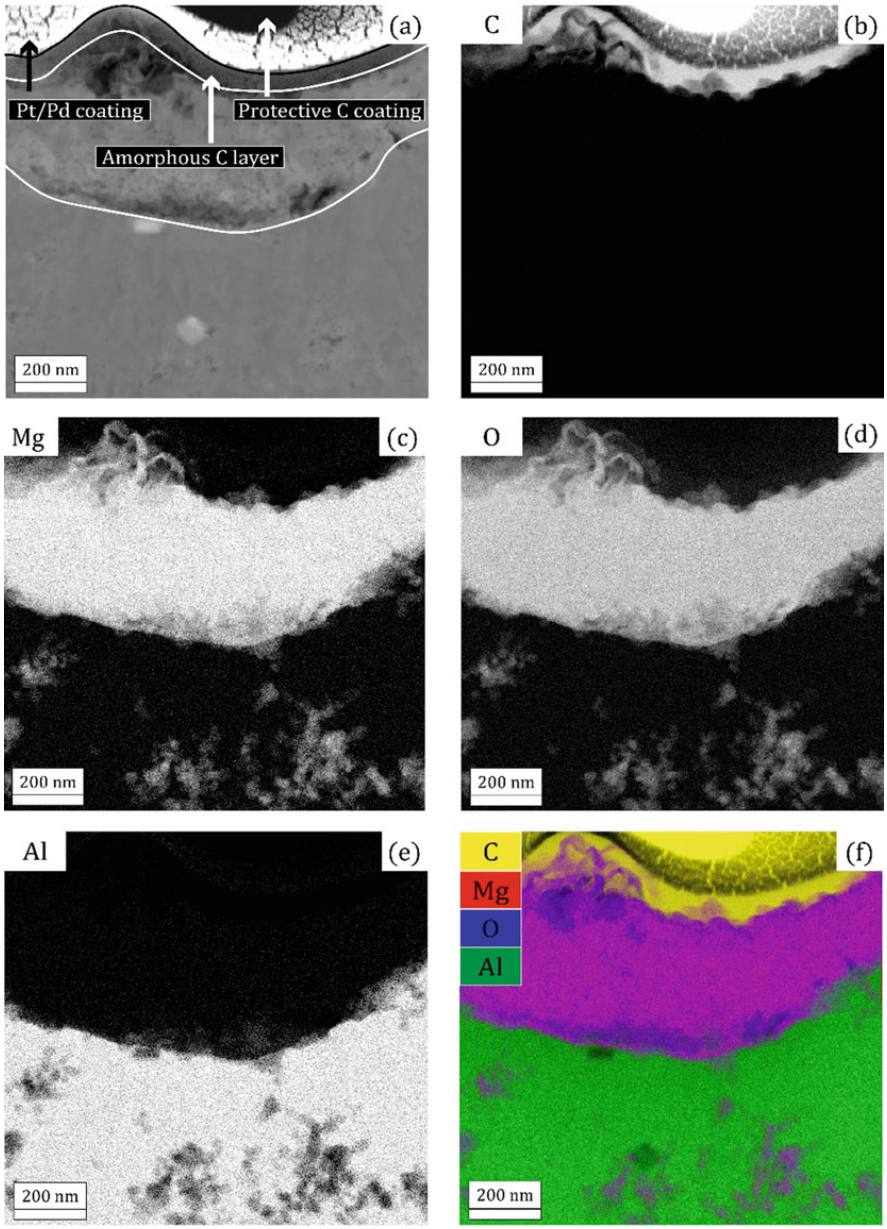

Fig. 3 **a** High-Angle Annular Dark-Field Scanning Transmission Electron Microscopy (HAADF STEM) image of the oxide layer of the Al alloy 5182 disc. The C **b**, Mg **c**, O **d**, and Al **e** mappings are made from the EELS-EDS spectroscopy maps. A combination of those various maps can be found in **f**

Conclusions

Oxidized discs of Al alloys 5182 (AlMg4.5Mn0.4) and 6016 (AlSi1.2Mg0.4), heat-treated in a gas mixture with 4% CO_2, 76% synthetic air, and 20% Ar at 750 °C for 7 h, have been analyzed by XRD and TEM to try to establish the inhibiting effect that CO_2 has on the oxidation process. The analyses revealed the presence of a 200–400 nm dense nanocrystalline MgO layer close to the surface of the high Mg-containing Al alloy 5182, covered by a 40–100 nm amorphous C layer. MgO crystals were also identified further into the Al bulk. Similar behavior was recognized for the low Mg-containing Al alloy 6016, having a nanocrystalline MgO layer of only 160–200 nm covered by a 15–120 nm-thin amorphous C layer. In this case, no MgO crystals were identified in the Al bulk of the disc sample, however, cubic $MgAl_2O_4$ crystals were found close to the MgO layer resulting in a discontinuous oxide layer in between the MgO layer and the Al bulk. In both cases, the amorphous C layer seems to hinder further evaporation of Mg delaying the rate of oxidation of Al and other alloying elements.

Future Work

The oxidized Al alloy 6016 discs will be further analyzed to clarify if there is a direct link between the Mg concentration and the thickness of the amorphous C- and nanocrystalline MgO layers, as indicated by the TEM results of the present study. X-Ray Photoelectron Spectroscopy (XPS) will also be used for both alloys, i.e. Al alloys 5182 and 6016, to construct a depth profile through the oxide layer towards the bulk. It is believed that this will allow a more detailed study of the C bonding in the amorphous layer, as well as the magnesium carbides identified for the high Mg-containing Al alloy 5182. Even further analysis and atomistic modelling will be performed to understand the mechanism of how the CO_2 interacts with the rough MgO surface.

Acknowledgements This work has been funded by the SFI Metal Production (Centre for Research-based Innovation, 237738). The authors gratefully acknowledge the financial support from the Research Council of Norway and the partners of the SFI Metal Production. The support from the Research Council of Norway to NORTEM (197405) and NorFab (245963/F50) is also acknowledged. Finally, the authors would also like to thank Egil Solberg from Alcoa ANS Mosjøen in Norway, for providing the Al alloy 5182 and 6016 samples.

References

1. Ingason HT, Sigfusson TI (2014) Processing of Aluminum Dross: The Birth of a Closed Industrial Process. JOM 66:2235–2242. https://doi.org/10.1007/s11837-014-1156-z
2. Gulbransen EA, Wysong WS (1947) Thin Oxide Films on Aluminum. J Phys Chem 51:1087–1103. https://doi.org/10.1021/j150455a004
3. More KL, Tortorelli PF, Walker LR, Hryn J, Krumdick G (2003) Microstructural Evaluation of Dross Formation on Mg- and Non-Mg-Containing Al Alloys from Industrial Furnaces. Materials at High Temperatures; Leeds 20:453. https://doi.org/10.3184/096034003782748838
4. Kim K (2015) Formation of Endogenous MgO and $MgAl_2O_4$ Particles and their Possibility of Acting as Substrate for Heterogeneous Nucleation of Aluminum Grains. Surface and Interface Analysis 47:429–438. https://doi.org/10.1002/sia.5726
5. Drieling H, Chesonis DC (2016) The Effect of Magnesium Supply on the Quality of Aluminum Melts. In: Grandfield J (ed) Light Metals 2014. Springer International Publishing, Cham, pp 1071–1075
6. Smith N, Kvithyld A, Tranell G (2018) The Mechanism Behind the Oxidation Protection of High Mg Al Alloys with Beryllium. Metall and Materi Trans B 49:2846–2857. https://doi.org/10.1007/s11663-018-1340-6
7. Cochran CN, Belitskus DL, Kinosz DL (1977) Oxidation of Aluminum-Magnesium Melts in Air, Oxygen, Flue Gas, and Carbon Dioxide. MTB 8:323–332. https://doi.org/10.1007/BF02657663
8. Solem CKW, Ekstrøm KE, Tranell G, Aune RE (2020) Evaluation of the Effect of CO_2 Cover Gas on the Rate of Oxidation of an AlMgSi Alloy. In: Tomsett A (ed) Light Metals 2020. Springer International Publishing, Cham, pp 1141–1147
9. Solem CKW, Solberg E, Tranell G, Aune RE (2021) Influence of Mg Concentration on the Inhibiting Effect of CO_2 on the Rate of Oxidation of Aluminum Alloys 5182 and 6016. Light Metals 2021:742–750. https://doi.org/10.1007/978-3-030-65396-5_97
10. Smith N, Gleeson B, Saidi WA, Kvithyld A, Tranell G (2019) Mechanism Behind the Inhibiting Effect of CO_2 on the Oxidation of Al–Mg Alloys. Ind Eng Chem Res 58:1434–1442. https://doi.org/10.1021/acs.iecr.8b04691
11. Qu Q, Ma J, Wang L, Li L, Bai W, Ding Z (2011) Corrosion Behaviour of AZ31B Magnesium Alloy in NaCl Solutions Saturated with CO_2. Corrosion Science 53:1186–1193. https://doi.org/10.1016/j.corsci.2010.12.014
12. Tosoni S, Spinnato D, Pacchioni G (2015) DFT Study of CO_2 Activation on Doped and Ultrathin MgO Films. J Phys Chem C 119:27594–27602. https://doi.org/10.1021/acs.jpcc.5b10130
13. Toda Y, Hirayama H, Kuganathan N, Torrisi A, Sushko PV, Hosono H (2013) Activation and Splitting of Carbon Dioxide on the Surface of an Inorganic Electride Material. Nat Commun 4:2378. https://doi.org/10.1038/ncomms3378
14. Haginoya I, Fukusako T (1983) Oxidation of Molten Al–Mg Alloys. Trans JIM 24:613–619. https://doi.org/10.2320/matertrans1960.24.613

Paper 4

The Role of CO_2 in the Oxidation-Protection of Mg-Containing Aluminum Alloys

CATHRINE KYUNG WON SOLEM, PER ERIK VULLUM, MAHSA EBADI, GABRIELLA TRANELL, and RAGNHILD E. AUNE

TEM EDS–EELS and XPS have been performed on disc samples of Al alloys 5182 (AlMg4.5Mn0.4) and 6016 (AlSi1.2Mg0.4) heat treated in an oxidizing atmosphere of 76 pct synthetic air, 20 pct Ar, and 4 pct CO_2. For both alloys, an amorphous C–C bonded layer on top of a nanocrystalline MgO layer was observed, which is believed to inhibit further oxidation of Mg for the 5182 alloy and breakaway oxidation for the 6016 alloy.

https://doi.org/10.1007/s11663-022-02524-3

SMALL additions (≥ 4 pct) of CO_2 in an oxidizing atmosphere have proven to have an immediate significant inhibiting effect on the rate of oxidation of the Al alloys 5182 (AlMg4.5Mn0.4) and 6016 (AlSi1.2Mg0.4), in regard to mass gain and oxide layer thickness.[1–3] The mechanism in which CO_2 inhibits the oxidation rate is, however, still unclear and under investigation.

Previous research[3] has established, through transmission electron microscopy (TEM) analyses, that after being exposed to small amounts of CO_2 at 750 °C, the Al alloy 5182 exhibited an amorphous carbon (C) layer with a thickness of 40 to 100 nm on top of a 200- to 400-nm-thick MgO layer, formed during heating of the alloy, according to Eq. [1].[3] The amount of C originating from the sample could easily be distinguished from the C deposited during sample preparation due to a Pt–Pd (80:20) electrically conducting layer between the two C layers. The Pt–Pd coating was originally applied due to poor conductivity caused by the dense, continuous nanocrystalline MgO oxide layer. It was concluded that further breakaway oxidation (see Eq. [2]) had been inhibited by the presence of a C layer, retarding further oxidization of the Mg and $MgAl_2O_4$ (spinel) formation.

A similar inhibiting effect has also been observed in earlier research by the present authors for low Mg-containing Al alloys.[1] Further investigations of the Al alloy 6016 (with 0.4 wt pct Mg) were hence carried out with the aim to identify if a small amount of CO_2 in the atmosphere even in this case enables the formation of an amorphous C layer protecting the alloy from further oxidation.

$$2Mg + O_2 = 2MgO \quad \Delta G^0_{750\,^\circ C} = -981.64\ \text{kJ} \qquad [1]$$

$$\frac{2}{3}MgO + \frac{4}{3}Al + O_2 = \frac{2}{3}MgAl_2O_4 \quad \Delta G^0_{750\,^\circ C} = -925.66\ \text{kJ} \qquad [2]$$

The Al alloy 6016 was examined by TEM using a double spherical aberration-corrected cold FEG JEOL ARM200FC microscope (JEOL Ltd., Tokyo, Japan), operated at 200 kV. No Pt–Pd coating was applied. The TEM lamellae were prepared by a Helios G4 UX FIB (FEI, Hillsboro, OR), and further investigations were carried out by a high-angle annular dark-field scanning transmission electron microscopy (HAADF STEM) combined with energy-dispersive X-ray spectroscopy (EDS) and electron energy loss spectroscopy (EELS) to secure that all elements of interest were mapped in the same way as in the previous study by the present authors.[3]

A Kratos Axis Ultra DLD X-ray Photoelectron Spectrometer (Kratos Analytical Ltd., UK) was applied to analyze the oxidized discs of Al alloys 5182 and 6016. The depth profiling was performed by Ar_n^+ clusters of ions at 4 kV. X-ray photoelectron spectroscopy (XPS) was performed with a monochromatic AlKα X-ray source operating at 11 mA and 11 kV (121 W). A pass energy of 160 eV was applied for the survey scans investigating an area of approximately 700 × 300 μm, and 20 eV for the high-resolution peaks. CasaXPS (Casa Software Ltd, Japan), version 2.3.24 was used to analyze the data.

Figure 1 presents the SEM and TEM results of the low Mg-containing Al alloy 6016 disc oxidized in an

CATHRINE KYUNG WON SOLEM, MAHSA EBADI, GABRIELLA TRANELL, and RAGNHILD E. AUNE are with the Department of Materials Science and Engineering, Norwegian University of Science and Technology (NTNU), 7491 Trondheim, Trøndelag, Norway. Contact e-mail: cathrine.k.w.solem@ntnu.no PER ERIK VULLUM is with the SINTEF Industry, 7034 Trondheim, Norway and also with the Department of Physics, NTNU, 7491 Trondheim, Trøndelag, Norway.

Manuscript submitted February 2, 2022; accepted April 6, 2022.

Published online: 24 April 2022

atmosphere of 76 pct synthetic air, 20 pct Ar, and 4 pct CO_2 at 750 °C for 7 hours. As can be seen from Figures 1(a) and (b), a dense, continuous nanocrystalline MgO oxide layer with a thickness of 160 to 200 nm was identified to exist on top of a discontinuous spinel ($MgAl_2O_4$) layer consisting of large crystals in the range of 0.5 to 3 μm. From Figure 1(b) a weak contrast line above the MgO layer can be seen, and when tuning the contrast of the apparatus, a bright line 15 to 120 nm above the MgO layer was identified as shown in Figure 1(c) (marked with a white dashed line) confirming the presence of an adsorbed C layer.

Figure 2 presents a HAADF STEM image and corresponding elemental mappings, deduced from the EDS and EELS spectrum images for the low Mg-containing Al alloy 6016. Mg, O, Fe, and Si were mapped by EDS, C, and Al by EELS. In Figure 2(a), the amorphous C layer can be seen on top of the nanocrystalline MgO layer, where the white arrows mark the top surface of the C layer, and in Figure 2(b) through (g) the individual mappings of C, Mg, O, Al, Fe, and Si can be seen. A color combination of the element maps of C (blue), Mg (red), Fe (yellow), and Al (green) is presented in Figure 2(h). In Figure 2(i), a combination of Mg (red), O (blue), and Al (green) is presented.

From Figure 1 it can be observed that the Mg content in the alloy had an influence on the oxidation steps during heating at 750 °C, as breakaway oxidation clearly had occurred forming a discontinuous layer of $MgAl_2O_4$ particles separating the MgO layer and the Al bulk in the case of the low Mg-containing Al alloy 6016, but not for the high Mg-containing Al alloy 5182.[3] The presence of the spinel phase was confirmed by the quantification of the ratio between Mg, Al, and O (approximately 1:2:4) by EDS and EELS. It is therefore believed that the amorphous C layer inhibited not only the oxidation of Mg, but also the breakaway oxidation of MgO as the sample heat treated in synthetic air without the small additions of CO_2 revealed only the presence of $MgAl_2O_4$, and no MgO.[3] The thickness of the MgO layer was thinner for the Al alloy 6016 than for the Al alloy 5182, but the influence of adding 4 pct CO_2 to the oxidizing atmosphere still applies, however, to a lesser extent, for the low Mg-containing alloy.

The HAADF STEM image confirmed the observation of an amorphous C layer as shown in Figure 2(a). Moreover, the EDS–EELS analyses verified the presence of a continuous MgO layer, based on a combination of Mg (red) and O (blue) in Figure 2(i), observed as a magenta-colored layer. The added amount of Al (green),

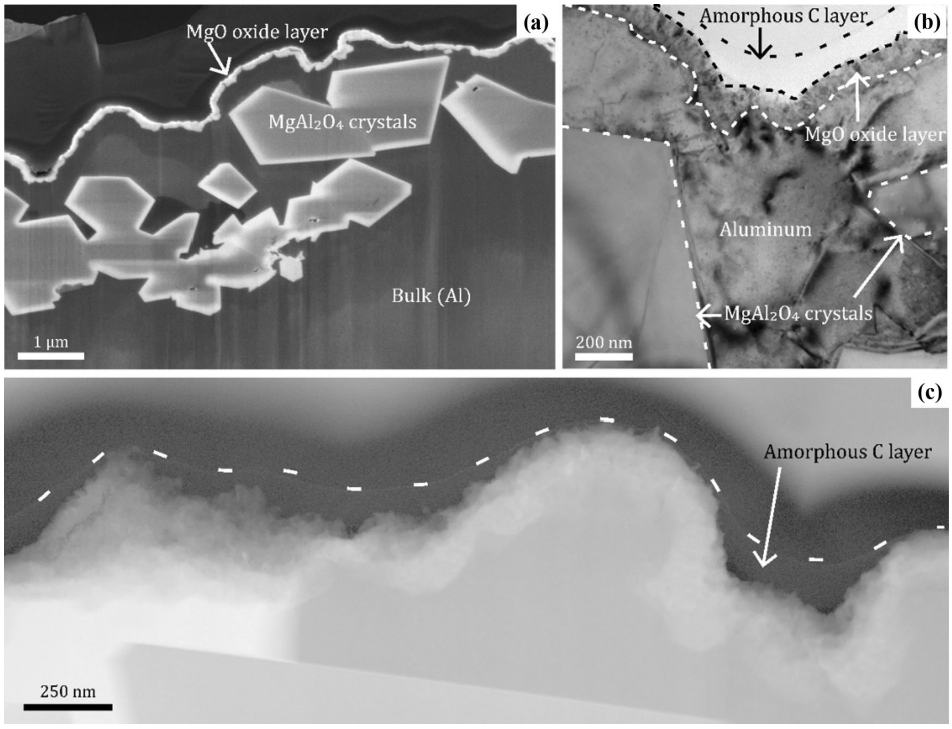

Fig. 1—Cross-section scanning and transmission electron microscopy (SEM and TEM) images of aluminum (Al) alloy 6016, where the SEM image in (*a*) shows the dense nanocrystalline MgO oxide layer on top of a discontinuous spinel ($MgAl_2O_4$) layer, the bright-field TEM image in (*b*) shows the amorphous C layer on top of the MgO layer, and in (*c*) the High-Angle Annular Dark-Field Scanning TEM (HAADF STEM) image shows a close up of the amorphous C layer on top of the MgO layer. A thin white continuous line is identified (white dashed line) at the interface between the inherent surface C layer and the protective C layer deposited in the FIB.

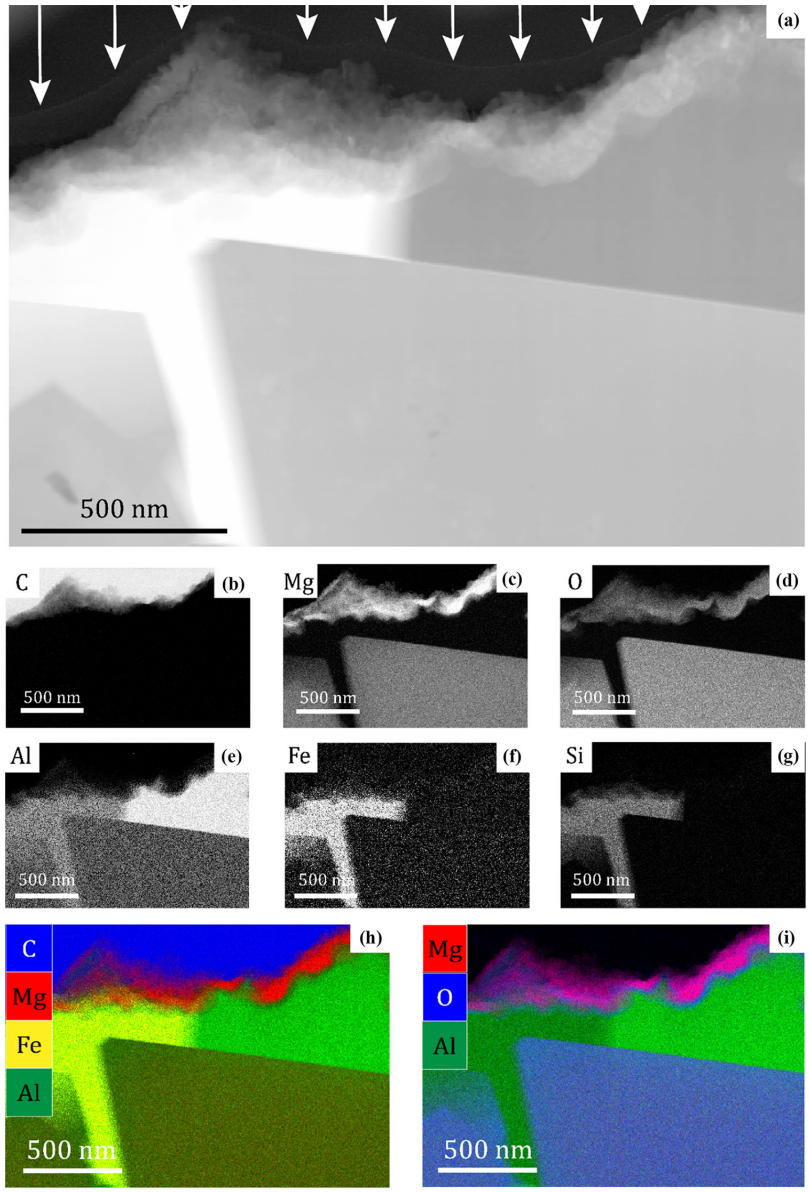

Fig. 2—(*a*) High-angle annular dark-field scanning transmission electron microscopy (HAADF STEM) image of the mapped cross-section area of the Al alloy 6016 disc heat treated in an oxidizing atmosphere with 4 pct CO_2, where energy-dispersive X-ray spectroscopy (EDS) and electron energy loss spectroscopy (EELS) applied for C (EELS), Mg (EDS), O (EDS), Al (EELS), Fe (EDS), and Si (EDS) are present in (*b*) through (*g*), respectively, and a combination of specific elements in (*h*) and (*i*).

observed as blue/violet-colored $MgAl_2O_4$ crystals, strengthened the theory of inhibited breakaway oxidation.

Fe and Si were also mapped and confirmed earlier findings for Al alloys containing Mg and Si, where clusters of Si were found at grain boundaries and close to the surface.[4]

Like in the case of the Al alloy 5182, the TEM analysis of the Al alloy 6016 confirmed that the C from the CO_2 had been adsorbed onto the sample surface, and the EDS–EELS analyses confirmed that it had been adsorbed onto a MgO surface. XPS analyses were subsequently carried out for both Al alloys in order to determine the bonding energies for C.

In Figure 3, the Mg1s, O1s, Al2p, and Mn2p peaks identified to be present in Al alloy 5182 are presented as a function of the binding energy for each sputtering time, and in Figure 4 the XPS spectra for Al alloy 6016, where Mg1s,

O1s, Al2p, and Si2p were identified to be present, are presented. The C1s peaks as a function of binding energy for the same sputtering times are presented for both alloys in Figure 5.

For Al alloy 5182 (4.5 wt. pct Mg), it was clear that the Mg had diffused towards the surface, as Mg1s was already recognized at values around 1304.0 eV after 50 seconds of etching (being very close to the top surface), having a concentration of 9.58 at. pct together with 32.12 at. pct for O1s. Very low concentrations of Al2p (< 3.53 at. pct) were observed by XPS after 1960 seconds (being closer to the bulk), strengthening the theory of no breakaway oxidation and thereby confirming the previous observations by TEM and EDS–EELS analyses (reported elsewhere[3]) as the Mg1s and O1s concentrations were identified to be 31.49 and 55.45 at. pct, respectively.

For Al alloy 6016, (0.4 wt. pct Mg), a concentration of 8.52 at. pct for O1s and 5.55 at. pct for Si2p were observed to be present at the very top surface of the Al sample. The XPS spectra of the Si2p strengthened the theory that Si clusters were present close to the Al disc sample surface, which thereby even in this case confirmed the previous observations by TEM and EDS–EELS analyses.[4] As for Al alloy 5182, the Al alloy 6016 revealed Mg1s identified for binding energies around 1304.5 eV after 350 and 750 seconds of etching, indicating the presence of MgO and carbonates.[5] A clear shift can, however, be seen in the Mg1s peak after 1960 seconds, as well as the appearance of an Al2p peak. The binding energies for these peaks correlate well, according to the performed TEM and EDS–EELS analyses, with the energies reported in the literature for $MgAl_2O_4$[6] which here was only observed for the low Mg-containing Al alloy 6016.

The inhibition of the oxidation rate for both Al alloys can be further evaluated by looking at the XPS spectra for C1s in Figure 5. As can be seen from Figure 5(a), the C1s spectra for Al alloy 5182 revealed a sharp peak at the very top surface of the Al disc sample, having C–C, C–O, C = O, and carbonates binding energies, and an atomic concentration of 71.42 at. pct.[7] This correlates well with the O1s peak observed in Figure 3(b) after 0 second of etching, as well as the amorphous C layer identified by TEM. The atomic concentration of C1s as shown in Figure 5(a) decreases, as a function of depth into the sample, to 56.23 at. pct after 50 seconds, and 26.59 at. pct after 350 seconds, with a changing distribution between C–C, C–O, C = O, and carbonates. This supports the results of Tosoni *et al.*[8] which found CO_2 to be adsorbed onto MgO (100) surfaces as carbonates. Furthermore, the presence of the Metal–Carbon (M–C) bonding strengthens the previous observations made by XRD where Mg_2C_3 was confirmed to exist for the high Mg-containing Al alloy 5182.[3] When reaching 350 seconds of etching there is a clear decrease in the atomic concentration of C1s (from 56.23 at. pct at 50 seconds to 26.59 at. pct at 350 seconds) as well as an increase in the case of Mg1s (from 9.58 at. pct at 50 seconds to 24.02 at. pct at 350 seconds) and O1s (32.12 at. pct at 50 seconds to 46.06 at. pct at 350 seconds). The changes in atomic concentration as a function of etching time and depth into the sample can be observed in Figure 6(a).

A similar observation was not seen at the very top surface in the case of the Al alloy 6016 at 0 second of etching. However, a decrease in the atomic concentration of C1s (from 97.58 at. pct at 50 seconds to 81.26 at. pct at 350 seconds) was observed at the same time as significant changes were observed in the XPS spectra for Mg1s and O1s (see Figures 4(a) and (b)). This observation corresponds well with the observation made previously for the high Mg-containing Al alloy 5182 (Figure 5). When looking at the distribution of the atomic concentrations based on the XPS spectra observed in Figure 6(b) an

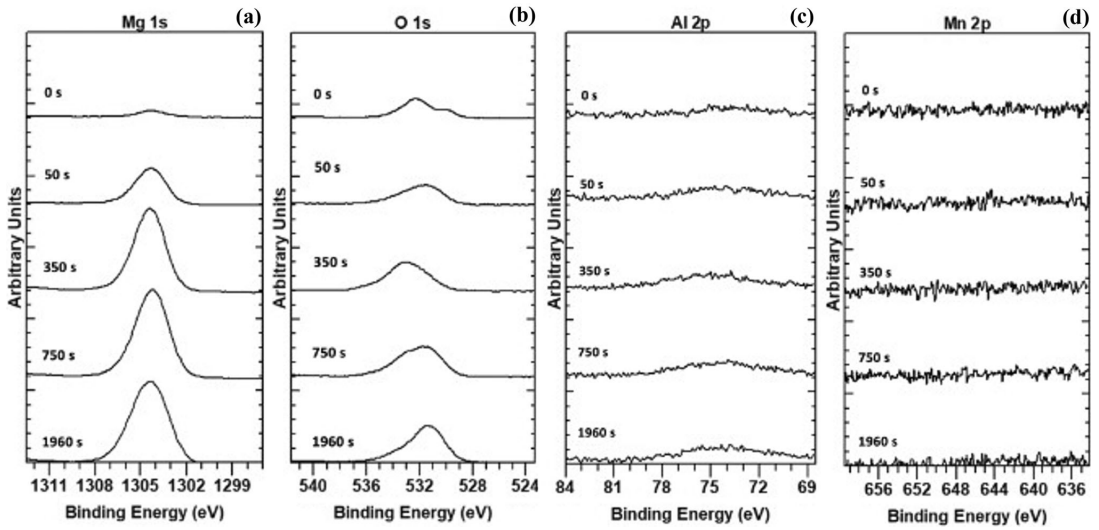

Fig. 3—X-ray photoelectron spectroscopy (XPS) spectra of Al alloy 5182 after being heat treated at 750 °C in 76 pct synthetic air, 20 pct Ar, and 4 pct CO_2. (*a*) Mg1s, (*b*) O1s, (*c*) Al2p, and (*d*) Mn2p.

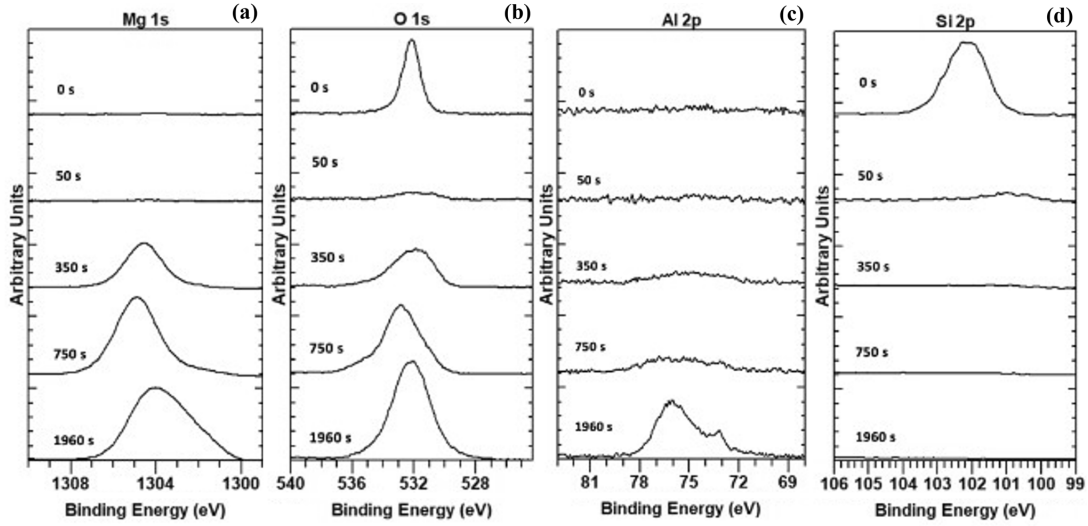

Fig. 4—XPS spectra of Al alloy 6016 after being heat treated at 750 °C in 76 pct synthetic air, 20 pct Ar, and 4 pct CO_2. (*a*) Mg1s, (*b*) O1s, (*c*) Al2p, and (*d*) Si2p.

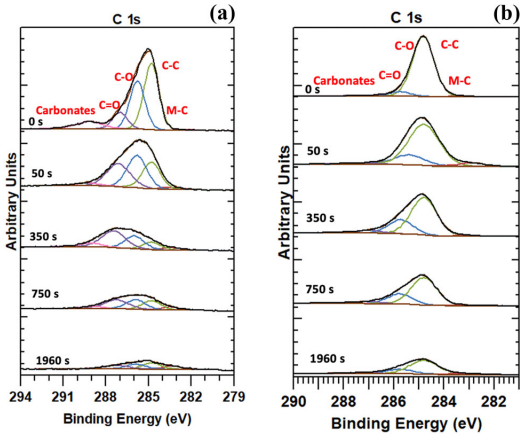

Fig. 5—XPS spectra of C1s after being heat treated in synthetic air with 4 pct CO_2. (*a*) Al alloy 5182 and (*b*) Al alloy 6016.

increase of the Mg1s (blue graph) and O1s (orange graph) concentrations can clearly be seen past 350 seconds of etching time, as well as a decrease of the C1s (gray graph). The significant increase of Al2p (green graph) after 1960 seconds was also confirmed (from 3.71 at. pct at 750 seconds to 12.32 at. pct 1960 seconds), strengthening the theory of breakaway oxidation.

As a result of the stability of MgO at 750 °C (see Eq. [1]), it is believed that Mg vapor may have diffused through cracks in the nanocrystalline MgO layer,[9] allowing it to react with the adsorbed CO_2 forming MgO and elemental, amorphous C (see Eq. [3]).[10] The elemental C formed on the inherent MgO surface as shown in Figure 1 is then believed to hinder further oxidation, as the amorphous C layer prevents O_2 to react with any Mg or Al thermodynamically, this scenario is supported by the highly negative $\Delta G^0_{750\,^\circ C}$ value of Eq. [3]. It is, however, necessary with further thermodynamic calculations as well as investigating the mechanism of the formation of the C layer to establish the stability of this layer.

$$CO_2\,(g) + 2Mg\,(g) = 2MgO + C \qquad \Delta G^0_{750\,^\circ C} = -650.86\ \text{kJ} \qquad [3]$$

In summary, based on the results presently secured through TEM EDS–EELS and XPS, it is established that CO_2 has an important role in the view of inhibiting the oxidation rate of AlMg alloys. The CO_2 in the oxidizing atmosphere is believed to react with Mg (g), forming an amorphous C–C bonded layer on top of a nanocrystalline MgO layer in the case of both the Al alloys 5182 and 6016 which is considered to inhibit further oxidation of Mg and thereby breakaway oxidation of MgO. The presence of Metal–Carbon bonding energies also strengthens the previously reported observations made in view of the presence of Mg_2C_3 for the high Mg-containing Al alloy 5182 and clusters of Si on the very top surface for the low Mg-containing Al alloy 6016.

Future work will include thermodynamic calculations and further evaluations of the observed amorphous C layer establishing the mechanism behind the formation of the layer.

The present work has been funded by the SFI Metal Production (Centre for Research-based Innovation, 237738). The authors gratefully acknowledge the financial support from the Research Council of Norway to NORTEM (197405), NorFab (245963/F50), and the partners of the SFI Metal Production.

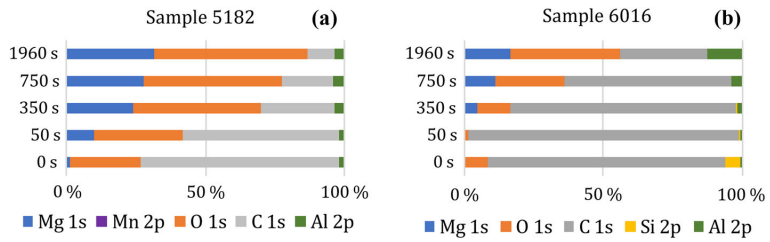

Fig. 6—Atomic concentrations from the XPS spectra for Mg1s (blue), O1s (orange), C1s (gray), Al2p (green) for Al alloys (*a*) 5182 and Mn2p (purple) and (*b*) 6016 and Si2p (yellow).

The authors declare that they have no conflict of interest.

FUNDING

Open access funding provided by NTNU Norwegian University of Science and Technology (incl St. Olavs Hospital - Trondheim University Hospital).

REFERENCES

1. C.K.W. Solem, E. Solberg, G. Tranell, and R.E. Aune: *Light Metals*, 2021, vol. 2021, pp. 742–50.
2. N. Smith, B. Gleeson, W.A. Saidi, A. Kvithyld, and G. Tranell: *Ind. Eng. Chem. Res.*, 2019, vol. 58(3), pp. 1434–42.
3. C.K.W. Solem, P.E. Vullum, G. Tranell, and R.E. Aune: *Light Metals.*, 2022, vol. 2022, pp. 587–93.
4. C.K.W. Solem, K.E. Ekstrøm, G. Tranell, and R.E. Aune: *Light Metals.*, 2020, vol. 2020, pp. 1141–47.
5. F. Khairallah and A. Glisenti: *Surf. Sci. Spectra.*, 2006, vol. 13(1), pp. 58–71.
6. D. E. Haycock, C. J. Nicholls, D. S. Urch, M. J. Webber, and G. Wiech; *J. Chem. Soc., Dalton Trans.*, 1978, no. 12, p. 1785–90. https://doi.org/10.1039/dt9780001785.
7. A. Roy, A.K. Mukhopadhyay, S.C. Das, G. Bhattacharjee, A. Majumdar, and R. Hippler: *Coatings*, 2019, vol. 9(9), 551. https://doi.org/10.3390/coatings9090551.
8. S. Tosoni, D. Spinnato, and G. Pacchioni: *J. Phys. Chem. C*, 2015, vol. 119(49), pp. 27594–27602.
9. B. Goldstein and J. Dresner: *Surf. Sci.*, 1978, vol. 71(1), pp. 15–26.
10. *FactSage 8.1*. ThermFact Inc & GTT-Technologies.

Paper 5

Sampling Procedure, Characterization, and Quantitative Analyses of Industrial Aluminum White Dross

Corresponding author: Cathrine Kyung Won Solem, cathrine.k.w.solem@ntnu.no, Department of Materials Science and Engineering, Norwegian University of Science and Technology (NTNU), Alfred Getz veg 2, 7034 Trondheim, Norway

Stefano Deledda, Department for Hydrogen Technology, Institute for Energy Technology (IFE), Instituttveien 18, 2007 Kjeller, Norway

Gabriella Tranell, Department of Materials Science and Engineering, Norwegian University of Science and Technology (NTNU), Alfred Getz veg 2, 7034 Trondheim, Norway

Ragnhild E. Aune, Department of Materials Science and Engineering, Norwegian University of Science and Technology (NTNU), Alfred Getz veg 2, 7034 Trondheim, Norway

Graphical abstract

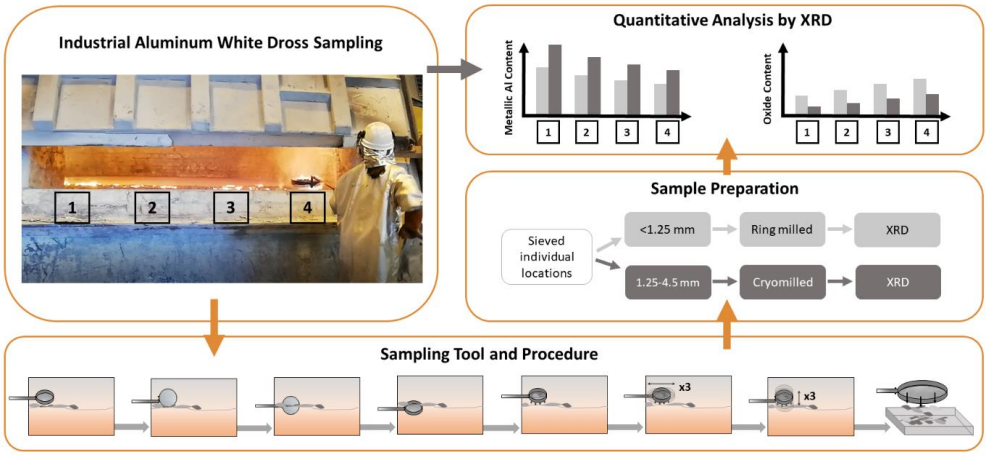

Keywords: Aluminum dross, Sampling, Cryomilling, XRD, Rietveld method

Abstract
Up to 10 % of all metallic aluminum (Al) produced is lost due to dross generation during production. It also causes an environmental problem due to hazardous waste generation following treatment, as well as toxic gas generation when in contact with water/humidity. As a result, it is desirable to identify the parameters contributing to the generation of the Al white dross mixture. In view of this, a sampling procedure for collecting representative dross samples directly from the casthouse holding furnace has been developed together with a methodology for analyzing and evaluating the results. XRD was used for phase/chemical composition analyses of sieved dross samples, and both ring milling and cryomilling were used during sample preparation. Cryomilling proved to be the superior method allowing dross fractions <1.25 mm and 1.25-4.5 mm to be pulverized. The fractions were analyzed and revealed that the sampling location inside the furnace plays a vital role as the injection of primary produced Al into the furnace influences the dross characteristics. From Location 1 (closest to the injection point) to Location 4 (furthest away from the injection point), the metallic Al content in the dross decreased simultaneously as the oxide content increased. The results also confirmed that the larger size fraction had a higher metallic Al concentration, which correlates well with literature findings. By adopting a methodical sampling procedure followed by consistent routines for sample preparation, characterization, and analyses, process operations can be studied and thereby potentially used to minimize the loss of Al due to dross formation.

Introduction
Aluminum (Al) is the second most important metal in modern society[1, 2], and the metal is carefully treated during production to obtain the desired characteristics of the product, *e.g.*, the required cleanliness, to tailor properties such as weldability, strength, and formability[3, 4]. Al is produced via both primary and secondary routes, and both routes generate side streams such as Al dross, which is a mixture of metallic Al, Al oxides, and oxides of alloying elements in addition to carbide and/or nitride compounds of these metals[5].

It is a well-known fact that Al has a high oxygen affinity and that the oxidation of Al is an exothermic reaction forming Al oxide (Al_2O_3)[6]. This means that during processing in the casthouse, there will always be a loss of Al when the Al oxide film formed on the surface of the molten metal is disturbed and broken up due to furnace operations such as during stirring and melt transfer operations[7].

During one-furnace practice (where melting of scrap, injection of primary-produced Al, stirring and skimming is performed in the same furnace), the injection of primary-produced Al is a critical process step as the injection influences the turbulence of the melt from one specific side of the furnace[8]. The same flow is, however, not seen during the two-furnace practice, as the melt is transferred from one furnace to another from the center-back of the furnace, causing a more symmetric melt distribution. Typical for both operations is that the melt must be stirred and skimmed before casting, which generates dross consisting of accumulated oxides together with metallic Al entrained within the oxide films and Non-Metallic Compounds (NMC)[8, 9]. Due to dross generation, as much as 10 % of the annual primary production of metallic Al has been reported to be lost[10, 11]. The dross generated during primary production of Al is defined as white dross and can potentially contain up to 70-75 % metallic Al in addition to the Al lost due to oxidation[2, 10].

Aluminum dross is a hazardous waste due to its reactivity when in contact with humidity or water[2, 12]. Toxic gases such as phosphine (PH_3), ammonia (NH_3), methane (CH_4), and hydrogen sulfide (H_2S) may be generated, which can cause both human and environmental harm during unit operations such as dross storage, transport, and in some countries when landfilled[12, 13]. It is,

therefore, desirable to reduce the dross generation during Al production to improve the metallic yield, as well as to lower the negative environmental load.

The heterogeneity of Al white dross makes it challenging to determine how different parameters, such as temperature, atmosphere, furnace operations, and chemical composition, influence the amount of dross generated and its characteristics. The present work has therefore sought to establish a methodology where Al white dross can be systematically collected directly from the holding furnaces in the casthouse and further analyzed. By adopting the method, the work also aims to determine the influence of standard furnace operations on dross generation, as well as how the sampling location inside the furnace influences the properties of the dross and the amount of entrained metallic Al.

Industrial Sampling Technique

Several studies dealing with the challenges of Al white dross collection and analyses can be found in the literature[14, 15]. However, as many of these studies characterize the dross, and report on their metallic Al concentration, see **Tab. 1**, the outcome of these studies varies. It has therefore been challenging to extract how the samples have been collected, analyzed, and further used to improve process operations[16–20].

***Tab. 1**. Examples of studies and the metallic Al content in the white dross.*

Metallic Al content in the dross, /wt.%	Reference
42.52	Abdulkadir et al.[16]
43.30	David and Kopac [17]
43.40	Hwang et al.[18]
55.70	Capuzzi and Timelli[19]
74.08	Meshram et al.[20]

Sampling equipment and procedure

The state-of-the-art for removing floating oxides and other NMC from the surface of molten Al is to manually use a metal rake (generally referred to as skimming, see Fig. 1 (a)). The removed dross is, in this case, collected directly into an open bin in front of the furnace, see Fig. 1 (b). However, the collection of dross samples is not part of the routine of furnace operation and is only sampled sporadically whenever needed. This could be when unusual behavior is seen, *e.g.*, when the gases generated while stirring the melt self-ignite[19].

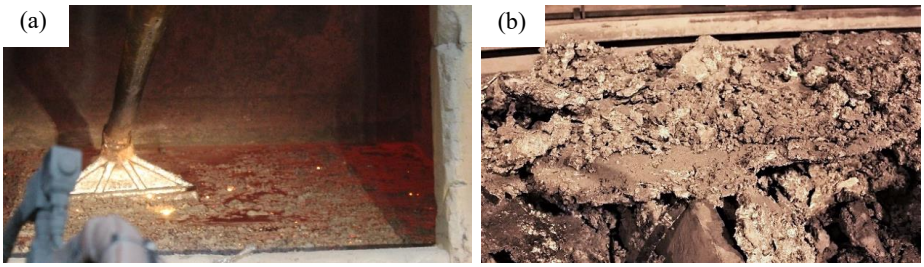

***Fig. 1**. (a) Non-Metallic Compounds (NMC) being removed (skimmed off) from a molten aluminum (Al) melt. (b) Skimmed off white Al dross consisting of large flakes, lumps, particles, and dust left for cooling.*

From observations made during industrial campaigns by the corresponding authors and conversations with the operators from different Al producers, it has been established that the total amount of dross generated during production is weighted after each skimming. The amount of dross

generated is used to evaluate if the operational conditions set for that specific melt are optimal, *i.e.*, the loss of metallic Al is at the lowest level possible in view of the operating conditions.

Molten Al samples are also collected to control the chemical composition of the metal. These samples are collected in a small cup submerged into the melt and then transferred to a mold shaped like a disc of 5 cm in diameter and 1 cm in height. The first sample is, by default, discarded due to the oxide skin the sampling equipment has to penetrate through during sampling, followed by two additional samples sent directly for analyses.

Quantitative analyses

The procedure for analysis of dross samples does, however, vary. Currently, the dross treatment plant analyzes the metallic Al dross content by remelting the dross to extract the Al metal. Samples collected from dross bins have also been analyzed at external characterization sites. The dross is therefore not currently analyzed and characterized during normal production. It is, however, protocol to scale the dross bin with skimmed-off dross to control the amount of dross generated for each melt.

The molten Al samples collected are first gently sanded on both sides before being analyzed by Optical Emission Spectroscopy (OES). The obtained result is then sent to the operator in the control room station within 5-10 minutes from the time of collection. OES is a convenient and quick technique allowing the chemical composition of the melt to be adjusted before casting if needed.

Present Sampling Technique

Sampling equipment and procedure

For collecting representative dross samples from inside the holding furnace, a tool (sieve) allowing the metal to drain off as the sample was collected was designed. The diameter and height of the sieve were set to 30 cm and 5 cm, respectively, and a 2-meter-long handle was added to allow samples to be collected from different locations in the furnace. A ¼-inch sized and 33 % perforated stainless-steel plate was selected as the sieve surface, see Fig. 2 (a) and (b). The present design was inspired by a sampling device for dross used in a study reported in the literature[21], where different combinations of hole sizes and perforations of the sieve were tested.

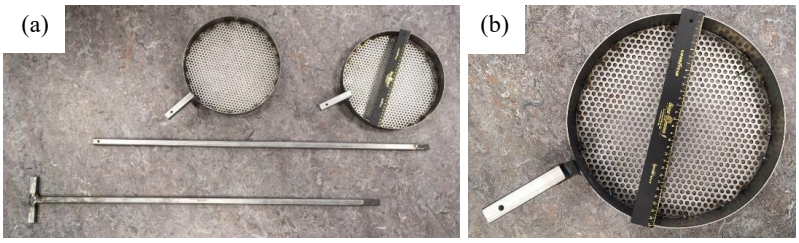

Fig. 2*. (a) Image of the sieve and disassembled handle used as the sampling tool to collect industrial Al white dross samples. (b) The perforated steel plate of the sieve.*

To avoid metallic Al from sticking to the surface of the sieve during sample collection, and potentially clogging the perforated surface of the sieve, Boron Nitride (BN) spray (COBN-3, NOR) was used for coating the sieve before each sampling.

Preparation of the furnace melt before sampling

The furnace operator mixed and prepared the molten Al melt according to the following standard procedures: (i) remelting of in-house scrap, (ii) addition of primary produced Al from the electrolysis process, and (iii) addition of alloying elements required for the chemical composition of the alloy in question to be met. In the skimming stage, the operators paused and allowed the collection of dross

(grey particles in Fig. 3 (a)-(c)) that was floating on top of the hot pool of molten metal (orange areas in Fig. 3 (a)-(c)).

It was, however, realized that even with a 2-meter-long handle on the sieve, reaching the oxides and NMCs floating on top of the melt inside the holding furnace was challenging. Hence, the operator carefully collected the floating layer without stirring it within reach of the furnace gate, as illustrated in Fig. 3 (d)-(f). The furnace door was also lowered, leaving a gap of ~1 m, to minimize the heat radiation from the melt.

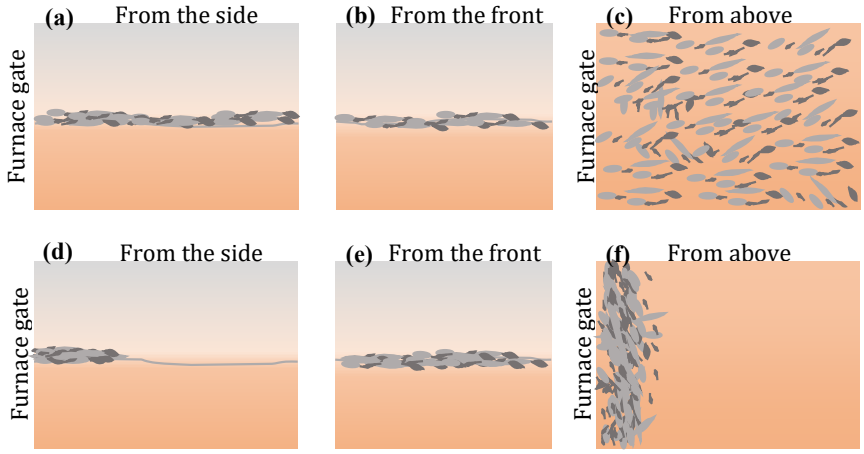

Fig. 3*. Illustration of the hot pool of molten metal, where (a)-(c) shows the oxides and NMCs (grey particles) naturally distributed while floating on top of the melt (orange areas), seen from the side, the front, and above, respectively, and (d)-(f) when carefully collected by the furnace gate, seen from the side, the front and above, respectively.*

Collection of dross samples

The dross samples were collected manually using the sieve, standing in front of the molten metal bath. The sieve was gently introduced over the liquid bath, flipped 90°, and submerged directly into the hot pool of molten metal partly through the oxide/NMC (dross) layer, as illustrated in Fig. 4 (a)-(c). The sieve was flipped back 90° when submerged in the melt, see Fig. 4 (d), before the sieve was lifted over the dross layer. The dross/molten metal floating just above the sieve was allowed to naturally drain off from the collected sample for 3 seconds before the sieve was shaken with a gentle force both horizontally and vertically to drain off as much molten Al as possible, *i.e.*, the first three times horizontally and then three times vertically, see Fig. 4 (f)-(g). The collected dross sample was then transferred from the sieve into a stainless-steel tray next to the furnace, see Fig. 4 (h). The dross sample was then allowed to cool naturally in air to ambient temperature. Finally, after an hour, the dross sample was collected from the tray and transferred into an air-sealed container awaiting further treatment.

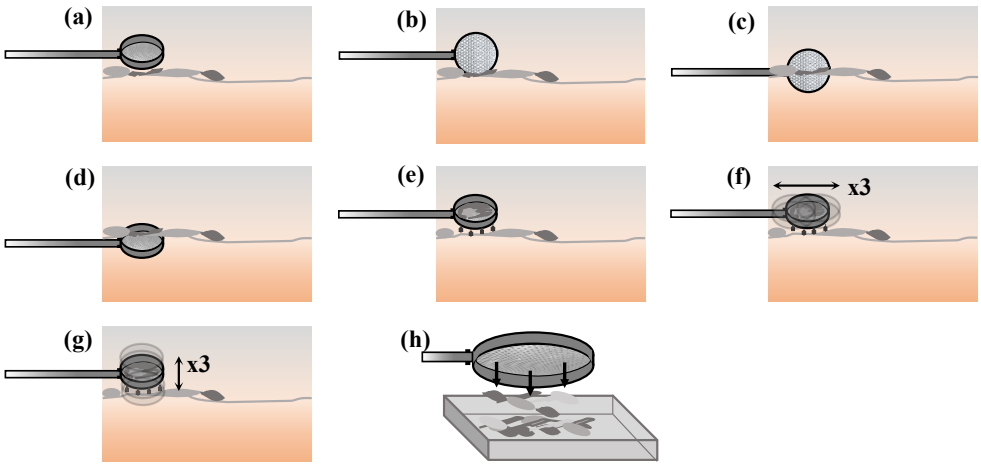

Fig. 4. Illustration of the sampling procedure of industrial Al white dross collected directly from the molten melt. The sieve is (a) introduced, (b) flipped 90°, (c) submerged into the melt, (d) flipped 90° back to a horizontal position, and (e) removed from the melt with the dross sample allowing the dross/molten metal floating just above the sieve to naturally drain off. The sieve was then shaken (f) horizontally and (g) vertically, draining off as much molten Al as possible, before being (h) transferred into a stainless-steel tray for cooling in air.

The same collection procedure was repeated for four different locations in the holding furnace in order to evaluate if the dross characteristics varied for different locations in the furnace. The locations were a function of distance from the primary produced Al injection hole, see Fig. 5. As seen from the figure, Location 1 was the sampling location closest to the injection hole and Location 4 furthest away. Location 2 and Location 3 were left and right of the center, respectively.

To minimize human errors with respect to the proposed sampling technique, the same person was responsible for carrying out the dross collection for all experiments evaluated in the present work.

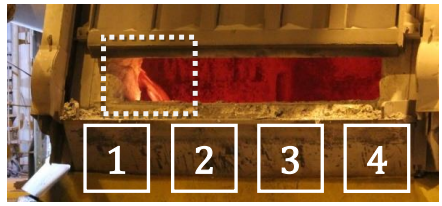

Fig. 5. Image of the front of a holding furnace in the casthouse showing the injection hole of the primary produced Al (dashed square), as well as the four different locations from which dross samples were collected.

Sample preparation

Each collected dross sample was sieved, and the fractions <1.25 mm and 1.25-4.5 mm were further studied. Pulverization of the collected dross samples, as well as thorough mixing of the individually obtained powders, was necessary to secure a homogeneous sample that would allow for reproducible quantitative analyses.

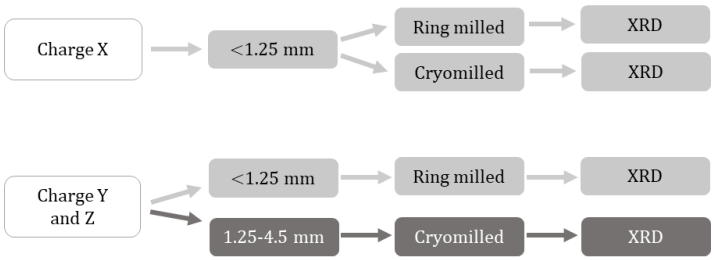

***Fig. 6**. Flow sheet showing the different charges, fractions, and milling techniques, followed by X-Ray Diffraction (XRD) analysis.*

Case Study A - Ring milling

The dross samples were individually milled using a ring milling unit from HERZOG (HSM 100 H, Germany). The unit was equipped with Tungsten Carbide (WC) rings with an inner diameter of 60 mm and a center bolt of 38 mm.

The ring mill was cleaned by milling two rounds of 20 seconds with silicon oxide (SiO_2) powder and thereafter cleaned with ethanol before use. One milling cycle consisted of three sequences, each with a milling time of 20 seconds. The powder was sieved between each sequence, and the powder fraction with a particle size of <100 µm was put aside. The rest of the powder was ring milled again using the same approach until reaching three sequences. Each sample had thereby a maximum milling time of 60 seconds.

For the smallest fraction of each dross sample, *i.e.*, the fraction <1.25 mm in size, the obtained powder was sieved into a sample with a particle size of <100 µm. After sieving, each sample was stored in a glass container awaiting analysis.

The mid-fraction of one dross sample, *i.e.*, the fraction 1.25-4.5 mm in size, was also ring milled. However, due to its ductile properties, the metallic Al present in the samples proved to be a problem as it became deformed and stuck to the sidewalls of the ring mill. As a result, the obtained powder was partly inhomogeneous.

Case Study B - Cryomilling

The dross samples were individually crushed at Institute for Energy Technology (IFE) in Norway using a cryomilling unit from SPEX (6770 Freezer/Mill, USA). Cryomilling was performed in the vial (with a volume of 16 cm^3) consisting of a central polycarbonate center cylinder and 440C steel end pieces. The cylindrical impactor was also made of 440C steel. Liquid nitrogen (N_2) was used to cool the sample down to -196 °C before and during milling. During milling, the cryomilling vial was completely submerged in a liquid N_2 bath.

The components of the cryomill vial were cleaned by sanding the impactor with sandpaper, brushed and cleaned with an abrasive detergent, and rinsed with ethanol between each milling cycle. One milling cycle consisted of a precooling step of 60 minutes, followed by 6 minutes of effective cryomilling (with an impact frequency of 24 Hz) and 3 minutes of cooling by liquid N_2. The cryomilling was then paused to refill the liquid N_2 bath. An additional pre-cooling step of 10 minutes was applied before the cryomilling was resumed to ensure reaching the target temperature (-196 °C). The procedure was repeated until a total milling time of 60 minutes was reached.

The mid-fractions of each dross sample (1.25-4.5 mm in size) were cryomilled, and the obtained powder was sieved into two different samples with a particle size of (i) >100 µm and (ii) <100 µm. In contrast to ring-milling, cooling the dross with the liquid N_2 allowed the metallic Al present in the

sample to embrittle and hence be crushed rather than deformed. After sieving, each sample was stored in a glass container awaiting further analyses.

Quantitative analyses

The milled and sieved samples were analyzed using an X-Ray Diffraction (XRD) unit from Bruker (D8 A25 DaVinci X-Ray Diffractometer, Billerica, USA). The unit was equipped with monochromatic CuKα radiation with a wavelength of λ=1.5406 Å. The XRD scans were carried out with a step size of 0.020° and a step duration of 8 s/step with a fixed divergence slit of 0.100°. A scattering angle of 2θ covering a range of 6-110° was set, and an X-Ray generator of 40.0 kV was applied for all measurements.

To evaluate the results and refine the data, the TOPAS software from Bruker (version 5, Billerica, USA) was applied to refine the data. The Powder Diffraction Files (PDFs) were extracted from the ICDD-4+PDF database. In addition, the crystallographic information for silicon (Si) and $Mg_{0.388}Al_{2.408}O_4$ (defect spinel) were obtained from literature[22, 23], see Tab. 2.

***Tab. 2**. Crystallographic information for the phases in the Al white dross, i.e., the Crystallographic Information File (CIF).*

Crystalline phase		Space group	Unit cell parameters	
			a, b, c	α, β, γ
Aluminum	α-Al	F m -3 m	4.0509, 4.0509, 4.0509	90, 90, 90
Magnesium oxide	MgO	F m -3 m	4.2140, 4.2140, 4.2140	90, 90, 90
Spinel	$MgAl_2O_4$	F d -3 m	8.0830, 8.0830, 8.0830	90, 90, 90
Defect spinel[22]	$Mg_{0.388}Al_{2.408}O_4$	F d -3 m:2	7.9783, 7.9783, 7.9783	90, 90, 90
Aluminum oxide	α-Al_2O_3	R -3 c	4.7602, 4.7602, 12.9933	90, 90, 120
Aluminum nitride	AlN	P 63 m c	3.1114, 3.1114, 4.9784	90, 90, 120
Silicon[23]	Si	F d -3 m	5.4304, 5.4304, 5.4304	90, 90, 90
Sodium aluminum oxide	$NaAl_{11}O_{17}$	P 63 / m m c	5.5930, 5.5930, 22.6100	90, 90, 120

The TOPAS software and the ICDD-4+PDF database were chosen for quantifying the phases, as they proved to be a suitable technique for analyzing metallic Al and the relevant oxides, *e.g.*, MgO. A reference sample containing 50 wt.% Al and 50 wt.% MgO was prepared and analyzed using the same instrument settings as for the collected dross samples, *i.e.,* the same step size, step duration, divergence slit, scattering angle, and voltage. The diffractogram, the fitted profile, and the difference between them are seen in **Fig. 7**, revealing a phase distribution of 49.9 wt.% Al and 50.1 wt.% MgO, see **Tab. 3**.

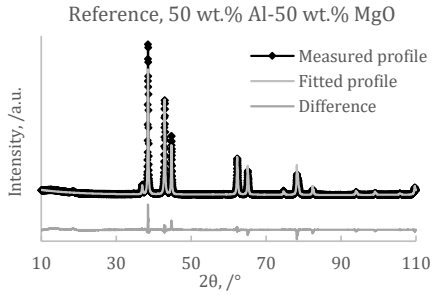

***Fig. 7**. XRD diffractogram of the pre-mixed reference sample containing 50 wt.% Al and 50 wt.% MgO, where the measured profile (black curve with diamonds), fitted profile by using the Rietveld Method (light grey curve), and the difference between the measured and fitted profile (dark grey curve) are plotted.*

Tab. 3. Phase distribution for the reference sample containing 50 wt.% Al and 50 wt.% MgO calculated by the Rietveld Method.

Phase	Phase distribution, /wt.%
α-Al	49.9
MgO	50.1

Results

Sampling equipment and procedure

When using the sieve, it was noted that a perforation high enough to allow the metallic Al to drain both naturally and when shaken to force excess metallic Al through the holes was required. It was also noted that the holes could not be too large, allowing the smaller oxide particles to follow the molten metal through the holes. Based on initial observations and experiences using the sieve, it was slightly modified to meet these requirements.

The sieve design and the 2-meter-long handle also ensured that the metallic Al quickly drained off, avoiding clogging of the sieve. At the same time, the oxide particles entrained in the metallic Al remained in the sieve.

Sample preparation and analyses

Both milling techniques chosen for sample preparation for pulverization and mixing proved to work well for the smaller fraction of the dross (<1.25 mm). However, cryomilling proved to be the superior method, allowing the dross to be pulverized for the smallest and mid fractions, *i.e.*, <1.25 mm and 1.25-4.5 mm in size.

From the results, it was clear that by using XRD, the heterogeneous Al dross samples were allowed to be analyzed after being pulverized to a homogeneous powder. The Rietveld Method also allowed quantification of the phase distribution by revealing the non-metallic phases.

Case Study A - Ring milling

One ring milled <1.25 mm pulverized dross sample (the smallest fraction) from each charge and location in the holding furnace was analyzed by XRD and quantified by the Rietveld Method. In some cases, two samples were analyzed to ensure reproducibility. **Fig. 8** (a)-(d) presents the diffractograms and the fitted profiles from the Rietveld refinement for Locations 1 to Location 4 of Charge Y. The differences between the measured diffractograms and the calculated fitted profiles are also presented in the same figure. In **Tab. 4**, the phase distribution obtained from the refinement of the XRD patterns shown in **Fig. 8** is summarized. It can be seen from the table that as the metallic Al content decreases from Location 1 to Location 4, the total oxide content increase.

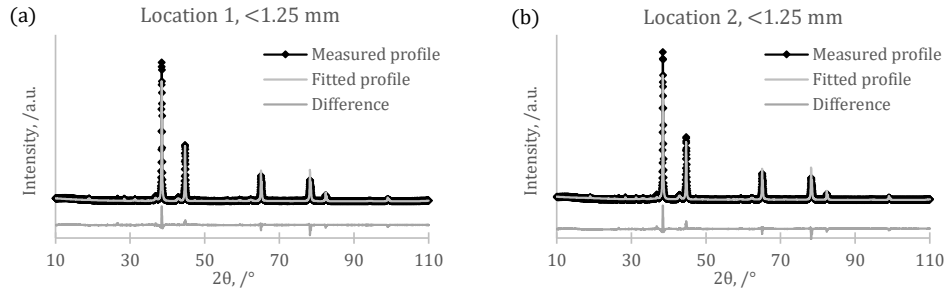

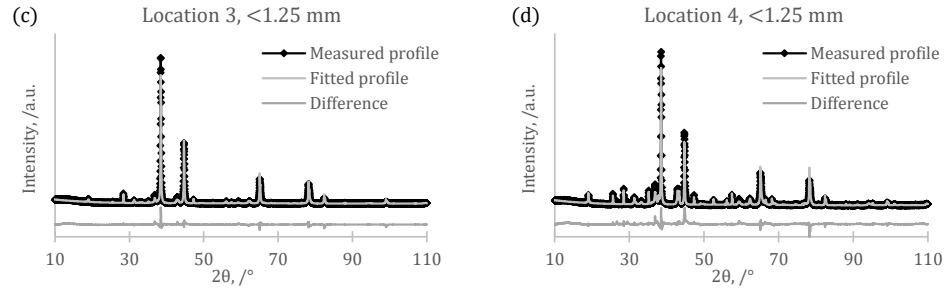

***Fig. 8**. XRD diffractograms of dross samples collected from Charge Y after being ring milled, where the measured profiles (black curve with diamonds), fitted profiles by using the Rietveld Method (light grey curve), and the difference between the measured and fitted profiles (dark grey curve) are plotted in (a)-(d) for the smallest fraction (<1.25 mm) at Location 1 to Location 4, respectively.*

***Tab. 4**. Phase distribution for Charge Y from Location 1 to Location 4 for the smallest fraction (<1.25 mm) of the ring milled dross samples calculated by the Rietveld Method.*

	Phase distribution from loc. 1 to 4, /wt.%			
Phase	**Loc. 1**	**Loc. 2**	**Loc. 3**	**Loc. 4**
Aluminum, Al	**80.8**	**75.3**	**69.0**	**51.5**
Magnesium oxide, MgO	8.6	9.8	18.7	14.4
Spinel, $MgAl_2O_4$	0.9	0.7	2.0	0.7
Defect spinel, $Mg_{0.388}Al_{2.408}O_4$	6.6	8.9	-	13.0
Aluminum oxide, Al_2O_3	1.0	1.6	3.7	14.6
Sodium aluminum oxide, $NaAl_{11}O_{17}$	0.0	0.1	0.3	0.3
Oxide content, total	**17.2**	**21.2**	**24.8**	**43.0**
Aluminum nitride, AlN	1.1	2.8	3.0	2.6
Silicon, Si	1.0	0.8	3.2	3.0

Similar behavior was established for Charge Z, as seen in Tab. 5.

***Tab. 5**. Phase distribution for Charge Z from Location 1 to Location 4 for the smallest fraction (<1.25 mm) of the ring milled dross samples calculated by the Rietveld Method.*

	Phase distribution from loc. 1 to 4, /wt.%			
Phase	**Loc. 1**	**Loc. 2**	**Loc. 3**	**Loc. 4**
Aluminum, Al	**56.2**	**31.7**	**20.5**	**17.9**
Magnesium oxide, MgO	6.9	3.0	2.8	24.4
Spinel, $MgAl_2O_4$	4.0	0.6	4.5	0.5
Defect spinel, $Mg_{0.388}Al_{2.408}O_4$	2.2	29.1	12.5	23.1
Aluminum oxide, Al_2O_3	17.9	20.5	54.2	23.8
Sodium aluminum oxide, $NaAl_{11}O_{17}$	4.8	3.2	0.9	4.5
Oxide content, total	**35.8**	**56.4**	**74.8**	**76.4**
Aluminum nitride, AlN	7.5	11.6	4.6	5.4
Silicon, Si	0.5	0.4	0.6	0.4

Case Study B - Cryomilling

One cryomilled 1.25-4.5 mm pulverized dross sample (mid-fraction) from each charge and location in the holding furnace was also analyzed by XRD, using the same program as for the smallest ring milled fraction. **Fig. 9** (a)-(d) presents the diffractograms and the fitted profiles from the Rietveld refinement for Location 1 to Location 4 of Charge Y, together with the differences between the measured diffractograms and the calculated fitted profiles. In **Tab. 6**, the phase distribution obtained from the refinement of the XRD patterns presented in **Fig. 9** is summarized. It can be seen from the table that as the metallic Al content decreases from Location 1 to Location 4, the total oxide content

increases, which confirms the results from the ring milled samples. When comparing the metallic Al content in the mid-fraction at all four locations with the smaller fraction at the same locations, an overall higher Al concentration was obtained.

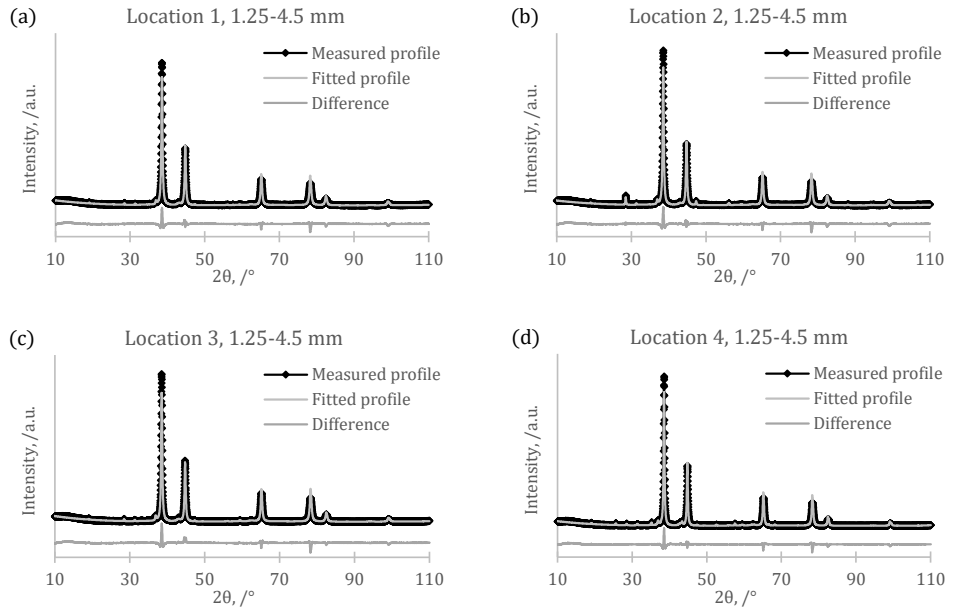

Fig. 9*. XRD diffractograms of dross samples collected from Charge Y after being cryomilled, where the measured profiles (black curves with diamonds), fitted profiles by using the Rietveld Method (light grey curve), and the difference between the measured and fitted profiles (dark grey curve) are plotted in (a)-(d) for the mid-fraction (1.25-4.5 mm) at Location 1 to Location 4, respectively.*

Tab. 6. *Phase distribution for Charge Y from Location 1 to Location 4 for the mid-fraction (1.25-4.5 mm) of the cryomilled dross samples calculated by the Rietveld Method.*

	Phase distribution from loc. 1 to 4, /wt.%			
Phase	**Loc. 1**	**Loc. 2**	**Loc. 3**	**Loc. 4**
Aluminum, Al	**88.1**	**86.3**	**85.2**	**81.7**
Magnesium oxide, MgO	4.5	6.4	7.2	7.8
Spinel, $MgAl_2O_4$	0.1	0.2	0.1	0.2
Defect spinel, $Mg_{0.388}Al_{2.408}O_4$	1.6	1.9	2.5	3.1
Aluminum oxide, Al_2O_3	0.5	0.3	0.3	4.3
Sodium aluminum oxide, $NaAl_{11}O_{17}$	2.9	0.0	2.1	0.00
Oxide content, total	**9.5**	**8.8**	**12.3**	**15.4**
Aluminum nitride, AlN	1.8	2.3	1.9	2.3
Silicon, Si	0.6	2.7	0.7	0.6

Similar behavior was also established for Charge Z, see Tab. 7, however, the differences between locations were clearly more noteworthy than for Charge Y.

Tab. *7. Phase distribution for Charge Z from Location 1 to Location 4 for the mid fraction (1.25-4.5 mm) of the cryomilled dross samples calculated by the Rietveld Method.*

	Phase distribution from loc. 1 to 4, /wt.%			
Phase	**Loc. 1**	**Loc. 2**	**Loc. 3**	**Loc. 4**
Aluminum, Al	**82.3**	**73.5**	**57.2**	**54.9**
Magnesium oxide, MgO	5.5	3.6	2.3	17.4

Spinel, $MgAl_2O_4$	1.0	12.5	2.4	0.9
Defect spinel, $Mg_{0.388}Al_{2.408}O_4$	6.0	5.5	10.9	12.7
Aluminum oxide, Al_2O_3	3.1	2.5	23.7	10.9
Sodium aluminum oxide, $NaAl_{11}O_{17}$	0.0	0.1	0.1	0.1
Oxide content, total	**15.6**	**24.1**	**39.4**	**41.9**
Aluminum nitride, AlN	1.7	2.0	2.1	3.0
Silicon, Si	0.5	0.4	1.4	0.2

Comparison between Ring milling and Cryomilling

The differences between the ring milling and cryomilling pulverizing processes could potentially influence the phase distribution in the final pulverized samples. In light of this, one dross sample from the <1.25 mm fraction of a third charge, *i.e.,* Charge X, was milled using both ring milling and cryomilling, see **Tab. 8**. As seen from the table, both the metallic Al and the oxide contents were fairly similar for both techniques.

***Tab. 8**. Phase distribution of the analyzed Al white dross sample (<1.25 mm fraction, Charge X.) pulverized by both ring milling (Case Study A) and by cryomilling (Case Study B).*

Phase	Case Study A Ring milling, /wt.%	Case Study B Cryomilling, /wt.%
Aluminum, Al	**25.4**	**28.4**
Magnesium oxide, MgO	14.9	18.0
Spinel, $MgAl_2O_4$	1.3	0.1
Defect spinel, $Mg_{0.388}Al_{2.408}O_4$	19.0	29.8
Aluminum oxide, Al_2O_3	34.5	18.7
Sodium aluminum oxide,	0.8	0.3
Oxide content, total	**70.5**	**66.9**
Aluminum nitride, AlN	1.5	3.5
Silicon, Si	2.6	1.2

Discussion

Sampling equipment and procedure

It has been reported in the literature that dross is a challenging material to study due to its heterogeneity[22, 24]. The sieve design and the long handle assured, however, successful dross sampling from different locations in the holding furnace. It also allowed the metallic Al to quickly drain off and thereby leaving the oxide particles entrained in the metallic Al in the sieve. Furthermore, it allowed for a systematic and reproducible way of dross sampling and was therefore seen as well-suited for the task.

During the development of the sampling procedure, several steps were assessed, testing different approaches, *e.g.*, (i) how and by what the sieve should be coated before being introduced into the bath, (ii) how deep the sieve should be submerged, (iii) how the sieve should be shaken after sample collection, and (iv) how many times the sieve should be shaken.

(i) Boron nitride was used for coating the sieve between each sampling and proved to be an essential step to avoid sticking of the metal to the stainless-steel sieve and occasionally even clogging the sieve. Both BN paint and spray were tested, but due to the viscosity of the paint, it was not as easily applied between each sampling as the spray.

(ii) To avoid a too large momentum when submerging the sieve into the molten metal bath, it was established that submerging the sieve just under the surface and moving it upwards towards the surface minimized the amount of metallic Al collected in the sieve during dross sampling.

(iii) For a successful sampling of the dross, it was noted that even more of the metallic Al collected in the sieve had to be drained. The sieve was therefore shaken with a gentle force both horizontally and vertically.

(iv) Shaking the sieve also proved to be an essential step that had to be fine-tuned to secure that the metallic Al did not solidify in the sieve, causing clogging. In regard to the time available, the sieve was shaken first three times horizontally and then three times vertically, giving the best possible dross sample with a minimum content of metallic Al.

Sample preparation and analyses

Under the present processing conditions, both ring milling and cryomilling proved to be efficient techniques to promote particle size reduction of dross samples of different fractions for further quantitative analysis by XRD. For larger size fractions, the cryomilling was superior as it made the Al brittle and, hence, possible to mill.

When comparing the milling techniques adopted in the present study, it should be noted that the processing temperatures are different, *i.e.*, ambient temperature versus cryogenic temperature. The milling dynamics are also different, with the driving force for ring milling being frictional forces and external impact forces for cryomilling. It was, however, demonstrated that despite these differences, the distribution of phases for the smallest fraction (<1.25 mm fraction), including the metallic Al content, was of a comparable magnitude even if the softness and ductility of metallic Al were a challenge during ring milling.

XRD was chosen for analyzing the sieved and milled samples as the technique produces clear and unambiguous results. Combined with the TOPAS software and the ICDD-4+PDF database, it becomes both a powerful and rapid technique capable of quantifying the phases present in the dross. It should, however, be noted that small crystalline structures that are present only in trace amounts may be undetected by the XRD readings.

The two analyzed charges, *i.e.*, Charge Y and Charge Z, showed correlating results with respect to the phases present in the dross samples. The decrease of the metallic Al concentration from Location 1 to Location 4 as the oxide content increased was also the case for both charges. It was also established that the larger dross particles contain higher concentrations of metallic Al which agrees well with literature findings[24]. In view of this, the hypothesis that the sampling tool and procedures adopted secure a consistent collection of dross samples with a high degree of reproducibility is strengthened.

Industrial dross sampling vs. present procedure

The industrial dross sampling procedure considers only the total amount of dross generated during one skimming session and not the chemical composition of the dross. By introducing a sampling tool, as well as methodologies for sampling, pulverization, and quantitative analysis, it is believed to be possible to systematically study (i) the Al white dross formation and (ii) the phase distribution between metallic Al and oxides at an industrial scale. This, in turn, is believed to give the industry further options and improved possibilities to control their generation of Al white dross and identify specific parameters to increase their total metallic Al yield.

Summary and Conclusion

Aluminum white dross is classified as a hazardous waste that generates toxic gases in contact with humidity and/or water. A burden on the environment is also recognized due to the large amounts of waste generated every year that must be transported and treated before being partly recycled or, in some cases, landfilled. In response to this, the present work has investigated the influence of standard

furnace operations on the characteristics of the generated dross. A sampling tool (sieve) was designed to collect representative dross samples directly from the molten Al melt in the casthouse holding furnace. The tool was used together with developed step-by-step procedures for pulverization, XRD analyses, and verification of different properties of the dross.

Based on the presented and discussed results, it is evident that the designed sieve, as well as the method developed for its use, secures representative dross samples. It was also established that ring milling (<1.25 mm fraction) and cryomilling (1.25-4.5 mm fraction) made it possible to prepare homogeneous powders for further quantitative XRD analysis containing both the brittle oxides and the soft Al. By refinement/optimization of standard process operations, it is believed that the Al industry will benefit from the outcome of the present study.

Future Work

Aluminum white dross samples generated during the production of Al alloys 1370 (>99.7 % pure Al) and 5182 (AlMg4.5Mn0.4) will be collected using the developed sampling tool, from the casthouse holding furnaces at the same industrial site as where the current sampling campaigns have been performed. The collected dross will be cooled in air and in protective atmospheres to evaluate the inhibiting effects that the protective atmospheres may have on the oxidation rate, as well as how it influences the dross morphology. The influence of the Mg concentration in alloy 5182 on the oxidation process and dross generation will also be investigated. In the future work, the method described in the present paper will also be followed for dross sample preparation (pulverization of three fractions, *i.e.*, <1.25 mm, 1.25-4.5 mm and >4.5 mm, metallographic characterization, and quantitative image analyses) and cross-validated by XRD analysis.

Acknowledgements

This research has been funded by the SFI Metal Production (Centre for Research-based Innovation, 237738). The authors gratefully acknowledge the financial support from the Research Council of Norway and the partners of the SFI Metal Production. Great gratitude is also given to Alcoa ANS Mosjøen and their operators for assisting during the industrial campaigns and sampling.

The authors declare that they have no conflict of interest.

References

1. Sverdrup HU, Ragnarsdottir KV, Koca D (2015) Aluminium for the Future: Modelling the Global Production, Market Supply, Demand, Price and Long Term Development of the Global Reserves. Resources, Conservation and Recycling 103:139–154. https://doi.org/10.1016/j.resconrec.2015.06.008

2. Mahinroosta M, Allahverdi A (2018) Hazardous Aluminum Dross Characterization and Recycling Strategies: A Critical Review. Journal of Environmental Management 223:452–468. https://doi.org/10.1016/j.jenvman.2018.06.068

3. Shi R, Miao J, Avey T, Luo AA (2020) A New Magnesium Sheet Alloy with High Tensile Properties and Room-Temperature Formability. Sci Rep 10:10044. https://doi.org/10.1038/s41598-020-67161-9

4. Banhart J, Chang CST, Liang Z, et al (2010) Natural Aging in Al-Mg-Si Alloys – A Process of Unexpected Complexity. Advanced Engineering Materials 12:559–571. https://doi.org/10.1002/adem.201000041

5. Steglich J, Friedrich B, Rosefort M (2020) Dross Formation in Aluminum Melts During the Charging of Beverage Can Scrap Bales with Different Densities Using Various Thermal Pretreatments. JOM 72:3383–3392. https://doi.org/10.1007/s11837-020-04268-4

6. Solem CKW, Ekstrøm KE, Tranell G, Aune RE (2020) Evaluation of the Effect of CO_2 Cover Gas on the Rate of Oxidation of an AlMgSi Alloy. In: Tomsett A (ed) Light Metals 2020. Springer International Publishing, Cham, pp 1141–1147

7. Takuya Y, Kenya K, Komarov SV, et al (2020) Evaluation of Aluminum Dross Generation Rate During Mechanical Stirring of Aluminum Through Model Experiment and Numerical Simulation. Metallurgical and Materials Transactions: Process Metallurgy and Materials Processing Science, B 51:1836–1846. https://doi.org/10.1007/s11663-020-01842-8

8. Johansen I, Strømhaug SI (2016) Energy control in primary aluminium casthouse furnaces. In: Sadler BA (ed) Light Metals 2013. Springer International Publishing, Cham, pp 935–939

9. Taylor JA, Prakash M, Pereira GG, et al (2010) Predicting Dross Formation in Aluminium Melt Transfer Operations. In: Materials Science Forum. https://www.scientific.net/MSF.630.37. Accessed 2 Nov 2018

10. Drouet MG, Handfield M, Meunier J, Laflamme CB (1994) Dross Treatment in a Rotary Arc Furnace with Graphite Electrodes. JOM 46:26–27. https://doi.org/10.1007/BF03220691

11. Ünlü N, Drouet MG (2002) Comparison of Salt-Free Aluminum Dross Treatment Processes. Resources, Conservation and Recycling 36:61–72. https://doi.org/10.1016/S0921-3449(02)00010-1

12. Tsakiridis PE (2012) Aluminium Salt Slag Characterization and Utilization – A Review. Journal of Hazardous Materials 217–218:1–10. https://doi.org/10.1016/j.jhazmat.2012.03.052

13. Das BR, Dash B, Tripathy BC, et al (2007) Production of η-Alumina from Waste Aluminium Dross. Minerals Engineering 20:252–258. https://doi.org/10.1016/j.mineng.2006.09.002

14. Hu K, Reed D, Robshaw TJ, et al (2021) Characterisation of aluminium black dross before and after stepwise salt-phase dissolution in non-aqueous solvents. Journal of Hazardous Materials 401:123351. https://doi.org/10.1016/j.jhazmat.2020.123351

15. Lashchev VYa, Rybinov VA, Terziyan PG (1969) Device for sampling metal and slag. Metallurgist 13:636–637. https://doi.org/10.1007/BF00734620

16. Abdulkadir A, Ajayi A, Hassan MI (2015) Evaluating the Chemical Composition and the Molar Heat Capacities of a white Aluminum Dross. Energy Procedia 75:2099–2105. https://doi.org/10.1016/j.egypro.2015.07.326

17. David E, Kopac J (2012) Hydrolysis of aluminum dross material to achieve zero hazardous waste. Journal of Hazardous Materials 209–210:501–509. https://doi.org/10.1016/j.jhazmat.2012.01.064

18. Hwang J-Y, Huang X, Xu Z (2006) Recovery of Metals from Aluminum Dross and Saltcake. https://doi.org/10.4236/JMMCE.2006.51003

19. Capuzzi S, Timelli G (2018) Preparation and Melting of Scrap in Aluminum Recycling: A Review. Metals 8:249. https://doi.org/10.3390/met8040249

20. Meshram A, Gautam D, Singh KK (2020) Recycling of White Aluminium Dross: Production of Potash Alum. Trans Indian Inst Met 73:1239–1248. https://doi.org/10.1007/s12666-020-01973-1

21. Kvithyld A, Bao S, Nordmark A, et al (2014) Development of a Sampling Device for Furnace Dross. In: Grandfield J (ed) Light Metals 2014. Springer International Publishing, Cham, pp 931–935

22. Gomez A, Lima NB, Tenorio JAS (2008) Quantitative Analysis of Aluminum Dross by the Rietveld Method. Mater Trans 49:728–732. https://doi.org/10.2320/matertrans.MRA2007129

23. Dutta BN (1962) Lattice Constants and Thermal Expansion of Silicon up to 900 °C by X-Ray Method. Physica Status Solidi (b) 2:984–987. https://doi.org/10.1002/pssb.19620020803

24. Kudyba A, Akhtar S, Johansen I, Safarian J (2021) Aluminum Recovery from White Aluminum Dross by a Mechanically Activated Phase Separation and Remelting Process. JOM 73:2625–2634. https://doi.org/10.1007/s11837-021-04730-x

Paper 6

Effect of (5%) CO_2 on the Oxidation Rate During Cooling of Industrial Aluminum White Dross

Corresponding author: Cathrine Kyung Won Solem, cathrine.k.w.solem@ntnu.no, Department of Materials Science and Engineering, Norwegian University of Science and Technology (NTNU), Alfred Getz veg 2, 7034 Trondheim, Norway

Stefano Deledda, Department for Hydrogen Technology, Institute for Energy Technology, 2027 Kjeller, Norway

Hannes Zedel, Department of Materials Science and Engineering, Norwegian University of Science and Technology (NTNU), Alfred Getz veg 2, 7034 Trondheim, Norway.

Gabriella Tranell, Department of Materials Science and Engineering, Norwegian University of Science and Technology (NTNU), Alfred Getz veg 2, 7034 Trondheim, Norway.

Ragnhild E. Aune, Department of Materials Science and Engineering, Norwegian University of Science and Technology (NTNU), Alfred Getz veg 2, 7034 Trondheim, Norway.

Keywords: Aluminum, white dross, oxidation, inhibition of oxidation, industrial sampling, image analysis

Abstract

Aluminum (Al) white dross is classified as hazardous waste and originates from the primary production of Al as a result of molten metal oxidation at an industrial scale. As the produced dross reduces the annual metallic Al production by ~10%, finding a way to reduce the dross formation has always been of interest. Several laboratory studies have shown that exposing molten Al to small amounts of CO_2 has an inhibiting effect on the oxidation rate of the metal. Still, no observations have been made at an industrial scale. The present work has therefore studied the impact of protective cooling of industrial white dross samples on the oxidation rate of the dross to spread some light on the issue. Samples were collected from the holding furnace in a casthouse during the production of two different charges of Al with varying amounts of magnesium (Mg), i.e., Charge 1 (AlMg1.0Mn0.4) and Charge 2 (AlMg1.2Mn0.4). The samples were cooled in ambient air and under a lid with 5% CO_2 mixed with 95% synthetic air in two parallels and later characterized by X-Ray Diffraction (XRD) and Electron Probe MicroAnalysis (EPMA) combined with deterministic image analysis allowing for a higher degree of accuracy in interpreting the results. Both methods confirm that all samples cooled under the protective atmosphere with 5% CO_2 had a higher content of metallic Al (89.4 wt.%) than those cooled in ambient air (86.0 wt.%), indicating that small amounts of CO_2 also inhibit the oxidation rate of dross at an industrial scale.

Introduction

Oxidation of aluminum (Al) and its alloys results in dross formation during industrial Al production, causing losses of up to 10% of the annual Al produced[1]. The rate of oxidation of Al has proven to be influenced by several parameters that can have both amplifying or inhibiting effects, i.e., the magnesium (Mg) content which has proven to have amplifying effects, and inert atmospheres to be inhibiting[2–5]. Controlling as many of the parameters as possible is therefore of utmost importance during process operations.

During primary production of Al, white dross is the oxidation product with a metallic Al content varying from 40 wt.% up to >80 wt.%[6–8]. The white dross is, in other words, highly heterogeneous, and it is also classified as a toxic and hazardous waste that should be managed in compliance with the current legislation. Landfilling of Al dross is forbidden in most European countries, and it must therefore be recycled and processed in a way that considers the environmental impact of the processing steps taken[9].

The Mg concentration in the Al alloy is reported to have a prompting effect on the dross formation resulting in an increasing oxidation rate[3, 10]. This effect is seen during production when adding Mg to the casthouse holding furnace, as well as at laboratory scale experiments. As a result, higher Mg concentrations contribute to formation of MgO and $MgAl_2O_4$ and consequently breakaway oxidation[11].

Furnace operations also have an effect on the oxidation rate of Al. Before casting the Al alloy, it is necessary to stir the melt to assure complete dissolution of the solid alloying elements added [12]. This task is mainly carried out by one of the furnace operators using a large rake that is carefully stirred through the melt, see Fig. 1[8]. The negative aspect of this step is that it disturbs and breaks up the oxide layers already formed and floating on top of the melt together with non-metallic compounds (NMCs) (areas marked with dotted white lines in Fig. 1), and new unreacted molten surfaces are exposed to the surrounding atmosphere (area marked with a dotted black line in Fig. 1). New oxide films and layers are, as a result, formed allowing even more of the molten Al to oxidize and thereby influence the overall metallic yield[13].

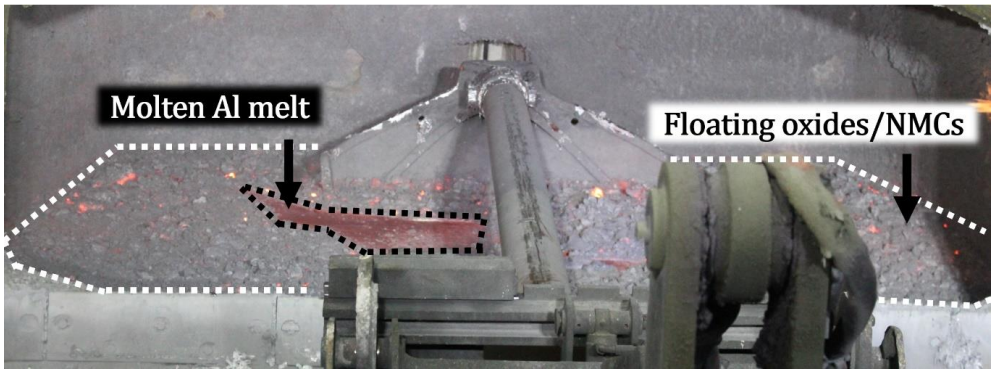

Fig. 1: Image of an aluminum (Al) melt being skimmed, where the oxides/non-metallic compounds (NMCs) are floating on top of the melt (marked with white). A small, cleaned area of the molten Al melt is also marked with a black dashed line.

As previously described, adding certain elements, e.g., beryllium (Be) and calcium (Ca), to the melt can inhibit the oxidation rate of Al[5, 14, 15]. There are, however, some risks related to adding these elements, as Be is known to be harmful to humans[16], and Ca may cause cracking of the alloy when being further processed through rolling and forming operations of the final product[17].

Another inhibiting parameter is adding small amounts of CO_2 to the atmosphere/cover gas in contact with the molten Al. Smith et al. reported an inhibiting effect from adding 50% CO_2 to an atmosphere of synthetic air, but an even greater impact was revealed when adding only 5% CO_2[18]. Further investigations using X-ray Photoelectron Spectroscopy (XPS) revealed a C-containing layer on top of an oxide layer, concluded to form by reactions with the CO_2 in the atmosphere[19].

The present authors (Solem et al. [20]) also investigated the influence of adding small amounts of CO_2 (4%) to an oxidizing atmosphere and its effect during heat treatment of Al alloys 5182 (AlMg4.5Mn0.4) and 6016 (AlSi1.2Mg0.4). The results revealed that small amounts of CO_2 significantly reduced the mass gain for both alloys and influenced the oxide layer morphologies compared to when heat treated in synthetic air. It was also observed that the CO_2 adsorbed onto a nanocrystalline MgO surface and formed an amorphous C layer preventing further oxidation of Mg to MgO and MgO to $MgAl_2O_4$ [11, 20].

The inhibiting effect caused by CO_2 has only been studied at laboratory scale and not at an industrial scale in view of its effect on dross formation. To do so, a tool for systematically collecting representative dross samples directly from the casthouse holding furnace was developed[21] and further modified by the present authors (Solem et al. [22]), supported by step-by-step procedures for sample collection, preparation, and analyses for quantifying the content of metallic Al, oxides, and other NMCs in the heterogeneous dross mixture collected. The developed tool was tested at an industrial campaign at Alcoa ANS in Mosjøn (Alcoa), Norway, and revealed to be well-suited for collecting representative dross samples. The chosen sample preparation method (cryomilling) and analysis technique (X-Ray Diffraction (XRD)) proved to give reproducible results.

Based on the above, the present work aims to investigate the effect of protective cooling of dross samples collected from the holding furnace at the casthouse facilities of Alcoa during the production of AlMgMn alloys with varying amounts of Mg. A cooling atmosphere of 5% CO_2 mixed with 95% synthetic air will be used and compared to cooling performed in ambient air. XRD and Electron Probe MicroAnalysis (EPMA) combined with deterministic image analysis will be used to analyze the results.

Experimental set-up and procedure

The sampling tool and procedure for collecting representative industrial Al dross samples developed by Solem et al. [22] were applied in the present work. To enable protective cooling of the collected dross samples, lids were designed to cover the dross trays, which also allowed for a gas or gas mixture to be purged onto the dross while it was being cooled. It was also crucial that the set-up did not disturb normal furnace operations while, at the same time, minimizing air exposure during sample handling.

Design of lids

The lids were made of stainless steel plates with a thickness of 2 mm. The shape chosen was rectangular with the dimensions 37x47 cm and a height of 16 cm, allowing one lid to cover one dross tray. A 43 cm long stainless-steel pipe was welded to the top surface of the lid to allow gas to be purged onto the dross tray (gas inlet). The pipe's location was chosen so that the gas was distributed evenly over the full dimensions of the tray. Two holes on each short side of the lid were added to create an escape route for the gas (gas outlet). In addition, two handles were placed on top of the lid to ease the lid's handling when placed over the dross tray or removed. The individual lids were connected by standard gas tubing to the gas bottles placed next to the holding furnace.

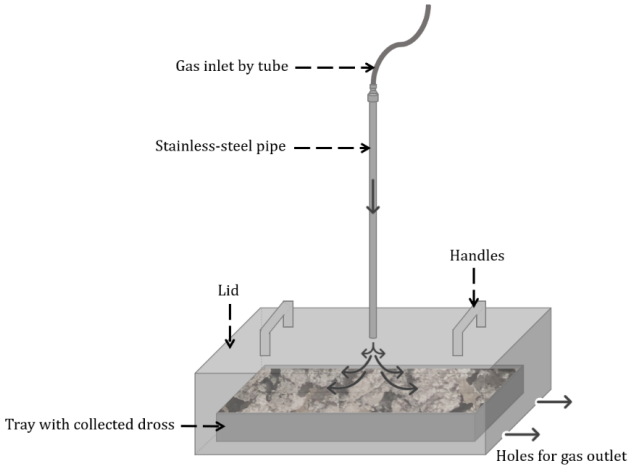

Fig. 2: Illustration of the lid and its use with the gas inlet on top and gas outlet on each short side.

Sampling

The sampling tool designed and its use to secure reproducible dross samples from the casthouse holding furnace during one-furnace practice have been discussed elsewhere (Solem et al. [22]). In the present study, the tool was used to collect dross samples from two different AlMgMn charges during production, i.e., Charge 1 (AlMg1.0Mn0.4) and Charge 2 (AlMg1.2Mn0.4). It was, however, made one significant adjustment to the previously developed procedure, and that was collecting *two* samples from each location instead of *one*.

The first dross sample that was collected was transferred to a dross tray and cooled in ambient air, and the second sample was transferred to a tray and immediately placed under a lid to be cooled in a protective atmosphere of 5% CO_2 mixed with 95% synthetic air. The same sampling procedure was followed for all locations where samples were collected, i.e., Location 1 (closest to the injection point of primary produced Al), Location 2 (left of the center of the holding furnace), Location 3

(right of the center of the holding furnace), and Location 4 (furthest away from the injection point of primary produced Al). This resulted in two parallels of collected samples for each charge.

An image of the complete set-up is seen in Fig. 3, where the gas is connected to each lid, covering a dross tray for protective cooling (marked with a red box). The other sample collected from the same location was placed in front and cooled in ambient air (marked with a blue box).

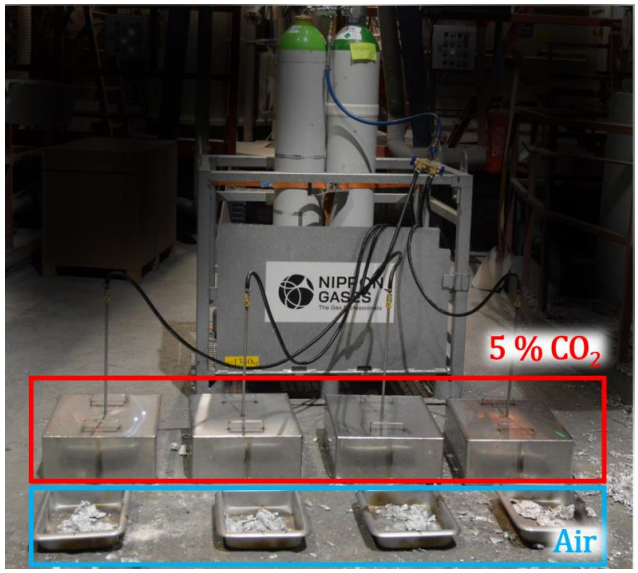

Fig. 3: Set-up for protective cooling of collected Al dross samples. Parallel samples are cooled under lids with a purging gas of 5% CO_2 mixed with 95% synthetic air (marked with red) and in ambient air (marked with blue).

To compare each sampled charge, the same person was responsible for collecting all the dross samples from the different locations in the holding furnace.

Figure 4 presents a flowchart showing the different steps that each dross sample collected from Charge 1 went through after being cooled, i.e., sieved into different fractions, pulverized, and characterized. Fig. 5 shows the same for Charge 2.

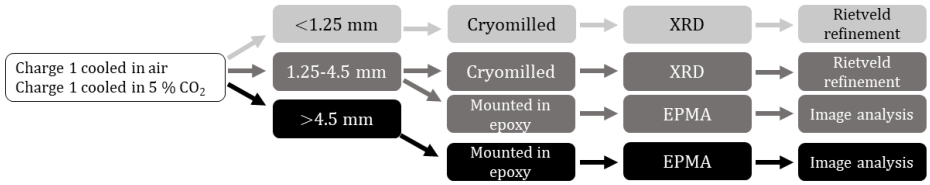

Fig. 4: Flowchart of the sample preparations and analysis for Charge 1.

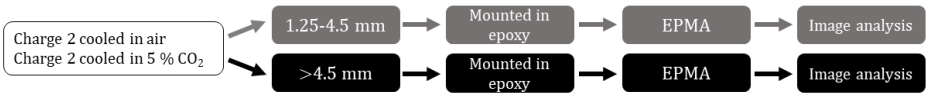

Fig. 5: Flowchart of the sample preparations and analyses for Charge 2.

Sample preparation

The two parallels of dross samples collected from each charge were sieved separately into three size fractions, i.e., <1.25 mm, 1.25-4.5 mm, and >4.5 mm. The smallest (<1.25 mm) and mid (1.25-4.5 mm) size fractions were pulverized by using cryomilling and later analyzed. Selected pieces of dross from the mid (1.25-4.5 mm) and largest (>4.5 mm) size fractions were mounted in epoxy and later analyzed.

Cryomilling of the smallest- and mid-size fractions of the dross samples: A cryomilling unit from SPEX (6770 Freezer/Mill, USA) was used for crushing each dross sample. The unit consisted of a vial made of polycarbonate, a cylindrical impactor, and end pieces made of steel. To cool the samples down to -196°C both before and during milling, liquid nitrogen (N_2) was used.

Each milling cycle consisted of a precooling step of 60 minutes to cool down the milling media and the samples, followed by 6 minutes of effective cryomilling and 3 minutes of pauses between the sequences. After three milling sequences, the apparatus was paused for the bath to be re-filled with liquid N_2 before the following milling sequence was started. This continued until an overall cryomilling time of 60 minutes was reached, which previously was reported by Solem et al. [22] to be sufficient for pulverizing the metallic Al lumps and flakes present as larger fractions in the dross. After finalizing the cryomilling, each sample was again sieved, and the portion of the sample that was <100 µm was put aside for XRD analysis.

Mounting and polishing of the mid- and large-size fractions of the dross samples: Eight randomly selected pieces of the dross from Charge 1 and Charge 2 were mounted in epoxy, polished with 1 µm diamonds, and dried in a cabinet at 65 °C for a minimum of 24 h before being coated with a 10-20 nm thin layer of carbon (C).

Quantitative analyses

All collected dross samples that were cryomilled were analyzed by XRD, and all mounted samples were analyzed by EPMA combined with deterministic image analysis (described below). This allowed for comparing the obtained results and, thereby, reaching a higher degree of accuracy when interpreting the results.

XRD: A D8 A25 DaVinci X-Ray Diffractometer (Bruker, Billerica, Ma, USA), equipped with a LynxEye^{TM} superspeed detector and monochromatic CuKα photons with a wavelength of λ=1.5406 Å, was used for the XRD analyses. A scattering angle of 2θ covering a range of 6-110° was set, and an X-Ray generator of 40.0 kV was applied for all measurements. Each XRD scan was carried out with a step size of 0.020° and a step duration of 8 s/step with a fixed divergence slit of 0.100°. Rietveld refinement was performed for all scans using the TOPAS software (version 5, Bruker, Billerica, Ma, USA) to refine the data and quantify the phases present in each sample.

EPMA: A JEOL JXA-6500F Field Emission Electron Probe Microanalyzer (JEOL Ltd., Tokyo, Japan) was used for the EPMA analyses. The same set-up of the instrument was used for all samples, i.e., the same detector was used for each specific element to assure consistency in the element

mapped, as well as the same magnification to allow for direct comparison of the microstructure and size.

Deterministic image analysis: For quantifying the elemental mappings in the EPMA scans, a previously established deterministic image analysis method was applied to 2D images where each pixel's intensity value represents the target element's concentration at its location[23]. Multiple quantitative metrics were derived for detecting the targeted phases using deterministic image analysis. Each pixel was classified into one of the targeted phases by its predominant content, and by applying an intensity threshold to the elemental C, the map provided detection of pores and epoxy. Where no pores or epoxy were detected, an oxygen (O) threshold was used to determine areas with a higher concentration of O representing non-metallics and areas with a lower concentration of O representing metallics. At a maximum, there were eight scans per experimental condition, of which one to two were discarded due to excessive cryolite content.

Each sample was distinctly divided into three different areas, i.e., (i) pores/epoxy-dominant areas, (ii) metallic areas, and (iii) non-metallic areas on a pixel-by-pixel basis, from the intensity thresholding of the elemental maps. The same thresholding was applied systematically for all EPMA scans to enable statistical pooling, comparisons, and the identification of trends. Based on this analysis, the relative content of each of the three phases per scan as a percentage of the total scanned area was determined. Each scan's relative metallic and non-metallic content was then pooled based on the experimental conditions for deriving means and medians per condition. An example is given in Fig. 6, where the EPMA result of Al (Fig. 6 (a)), O (Fig. 6 (b)), and C (Fig. 6 (c)) are presented together with the CP image (Fig. 6 (d)), as well as the phase detection based on the listed criteria above (Fig. 6 (e)).

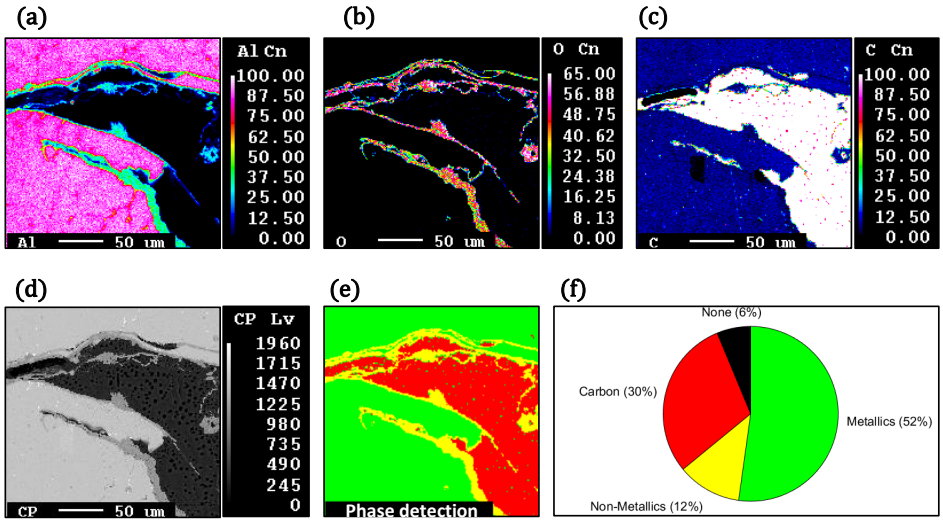

Fig. 6: EPMA results of (a) Al, (b) O, (c) C, (d) CP image, and (e) the binary phase detection based on those elements. A quantitative analysis is presented in (f).

Results and discussion

The effect of small amounts of CO_2 added to the atmosphere during protective cooling of industrial dross samples was (after sample reparation) evaluated by XRD, as well as EPMA combined with deterministic image analysis. XRD was chosen as it is a technique that gives unambiguous results and deterministic image analysis as it is a new and innovative approach with the ability to confirm the XRD results. Its method can also evaluate the presence of trace amounts that may be undetected by the XRD readings.

X-Ray Diffraction

The metallic Al content from the XRD measurements for the smallest fraction (<1.25 mm) and the mid fraction (1.25-4.5 mm) for Charge 1 cooled in CO_2 (red graphs) and in ambient air (blue graphs) for Location 1 and Location 4, are presented in Fig. 7 (a) and (b). As can be seen from the graphs, the metallic Al content is higher when cooled in CO_2 than in air for both fractions. It can also be seen that the metallic Al content is higher for the 1.25-4.5 mm fraction than for the <1.25 mm fraction.

The oxide content in the dross at respective locations for each of the fractions is given in Fig. 7 (c) for the smallest fraction (<1.25 mm) and in Fig. 7 (d) for the mid fraction (1.25-4.5 mm). From the XRD results, an increasing oxide/NMCs content with decreasing metallic Al content was established to exist from Location 1 to Location 4. This confirms the earlier observations made by the present authors[22].

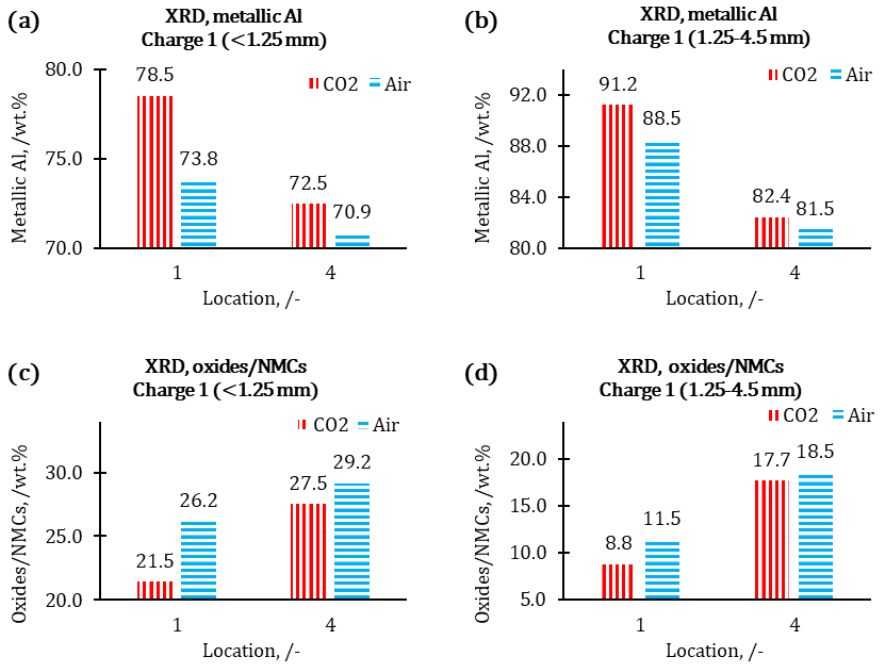

Fig. 7: X-Ray Diffraction (XRD) results of Charge 1 cooled in CO_2 (red, vertically lined) and ambient air (blue, horizontal lines) for the metallic Al content of (a) fraction <1.25 mm and (b) fraction 1.25-4.5, and for the oxide/Non-Metallic Compounds (NMCs) contents of (c) fraction <1.25, and (d) fraction 1.25-4.5 mm.

The metallic Al concentrations in the dross were observed to be slightly higher than earlier reported values[22], which is believed to be linked to the applied milling technique (more homogenous samples), as well as the protective cooling step. As previously mentioned, cryomilling was used for milling both sample fractions, but it was not the obvious choice of sample preparation technique from the start. Ring milling was first tested on the smallest fraction of the dross samples, but the technique did not successfully mill the dross down to the fine powder needed for accurate XRD analyses (large Al flakes were observed to exist in the pulverized material), resulting in an inhomogeneous powder. Based on this, cryomilling was used on both fractions of the dross samples, allowing the metallic Al content in the different fractions to be directly compared with a higher degree of accuracy. The potential inhibiting effect on oxidation from using protective cooling by purging gas with 5% CO_2 directly onto the dross samples while being covered by lids could then also be more accurately studied.

Based on the experimental approach, the mid fractions (1.25-4.5 mm) for both charges investigated proved to have a higher metallic Al concentration when cooled under protective conditions. This indicates that the oxidation process had been inhibited and that the earlier laboratory-scale findings, i.e., where the oxidation rate of Al alloys containing Mg was inhibited when exposed to small amounts (4%) of CO_2 during cooling, had been reproduced through protective cooling under industrial conditions.

EPMA and image analysis

The EPMA results for two of the analyzed Al dross samples from Charge 1, i.e., fraction >4.5 mm from Location 1, are presented in Fig. 8. Their respective Scanning Electron Microscopy (SEM) images are shown in the first row, where the sample in Fig. 8 (a) is cooled under a lid with 5% CO_2 and (b) in ambient air. The EPMA results for the elements Al (second row), Mg (third row), and O (fourth row) are also presented in the same figure, where the left column is the sample cooled in 5% CO_2 and the right in ambient air.

As can be seen from the EPMA results, it is confirmed that the collected dross samples are strongly heterogeneous, as it varies from dense metallic Al areas with thin films and small MgO areas (left column) to highly oxidized areas consisting of larger areas of $MgO/MgAl_2O_4$ and Al_2O_3 (right column). The respective scale bars based on the experimental calibration are also given for each element.

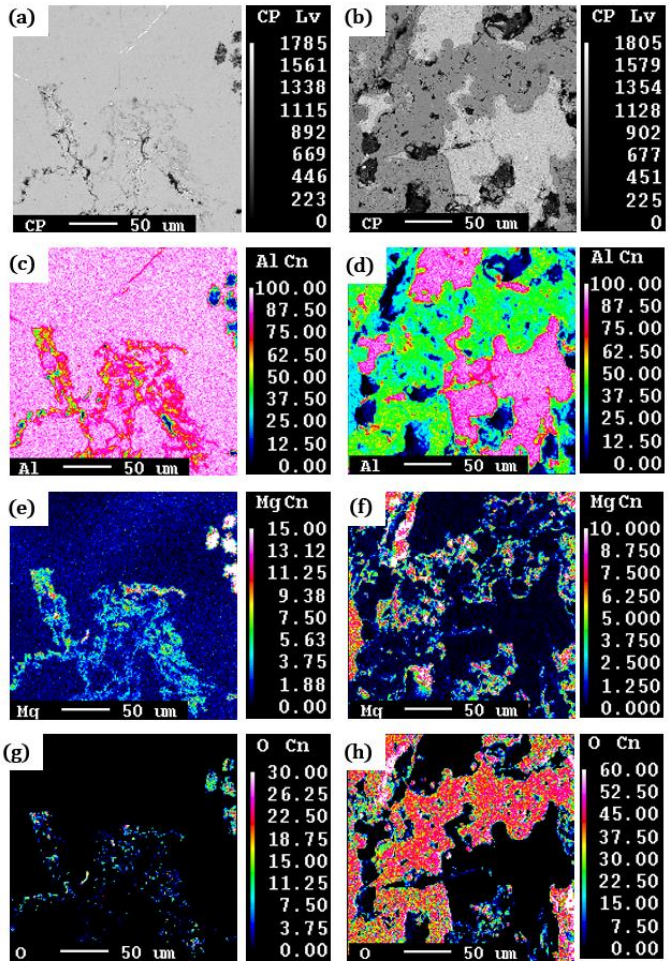

Fig. 8: Representative Electron Probe MicroAnalysis (EPMA) results of the collected dross samples for the elements Al (second row), Mg (third row), and O (fourth row), where the left column is dense Al areas with thin films, and the right column is a highly oxidized sample having larger areas with Al_2O_3 and $MgO/MgAl_2O_4$. Both samples are collected from Charge 1, Location 1, where the left sample has been cooled under a lid with 5% CO_2 and the sample to the right in ambient air.

It can also be seen from Fig. 7 that the samples protectively cooled under a lid with 5% CO_2 had, on average, a higher metallic Al content than the sample cooled in ambient air. However, it should be taken into account that the dross samples are highly heterogeneous. As a result, pure metallic Al areas are also recognized for some samples cooled in ambient air and highly oxidized areas for those cooled under a lid with 5% CO_2.

The average metallic Al contents identified by deterministic image analyses of the EPMA results for Charge 1 at Location 1 to Location 4 for the 1.25-4.5 mm and >4.5 mm fractions are presented in Fig. 9 (a), where the dross samples cooled under a protective atmosphere of 5% CO_2 are shown to the left (red checkered graphs) and in ambient air to the right (blue squared pattern). Even in this case, the figure shows that a higher metallic Al content is obtained for both fractions when cooled under a lid with 5% CO_2 than in ambient air, following the previously observed trends obtained at laboratory scale[11]. The results are, however, not consistent with the trend of having higher metallic

Al content for larger fractions[24]. This deviation is believed to originate from the number of dross samples analyzed. In the present study, eight randomly selected samples were considered for deterministic image analysis from each location, giving 32 samples for each fraction and for each cooling atmosphere (a total of 256 samples). In view of this, it should be noted that some samples were not included in the analysis as they proved to consist of pure cryolite. The overall result showed that the dross samples cooled under a protective atmosphere of 5% CO_2 had an average metallic Al content of 89.4 wt.% when including both Charge 1 and Charge 2, as well as Location 1-4 for both fractions 1.25-4.5 mm and >4.5 mm, compared to 86.0 wt.% metallic Al when cooled in ambient air.

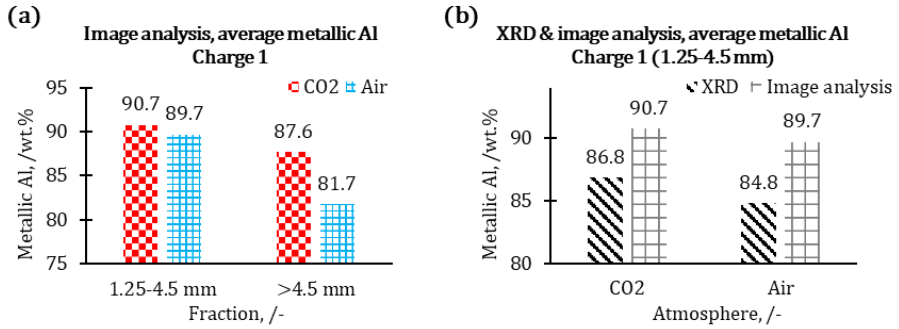

Fig. 9: Results from the deterministic image analysis showing the metallic Al content, i.e., (a) as a function of fraction comparing the samples cooled in 5% CO_2 (left graphs, red) and ambient air (right graphs, blue), and (b) as a function of the atmosphere where the deterministic image analysis (checkered graphs) is compared with the XRD results (striped graphs).

When comparing XRD and deterministic image analysis results, see Fig. 9 (b), results in the same order of magnitude are obtained (striped graphs to the left represent the XRD results, and the squared graphs to the right the deterministic image analysis). Using XRD data as a reference, being an established method, validates the novel quantitative analysis of the EPMA scans as a possible approach for observing trends with similar metrics.

Summary and conclusions

The present study investigated whether protective cooling of industrial Al white dross samples would influence the oxidation rate of Al. Two parallels of dross samples were collected directly from the casthouse holding furnace, of which one parallel was cooled under a lid purged with 5% CO_2 mixed with 95% synthetic air and the other in ambient air (casthouse atmosphere). The samples were further sieved, pulverized, and analyzed to determine their metallic Al content, as well as the oxide/NMC concentrations.

It is concluded that the CO_2-enriched atmosphere inhibits the oxidation rate of the industrial dross samples, confirming earlier observations from laboratory trials. From the XRD analysis, it is also established that the industrial dross samples cooled under a lid purged with 5% CO_2 have a higher metallic Al content for all fractions than for those cooled in ambient air. These results were further confirmed by EPMA analyses combined with deterministic image analysis.

Future work

Future work will continue to investigate the influence of different ratios of CO_2 on the oxidation rate of industrial white dross samples, as well as other atmospheres and different temperatures. Transmission Electron Microscopy (TEM) will also be carried out to see if an amorphous C layer is present on the surface of the samples cooled under a protective atmosphere.

Acknowledgments

This research has been funded by SFI Metal Production (Centre for Research-based Innovation, 237738). The authors gratefully acknowledge the financial support from the Research Council of Norway and the partners of SFI Metal Production. Special gratitude is given to Alcoa ANS for allowing us to collect the industrial dross samples from their site at Mosjøen, Norway, and to their operators for assisting during the industrial campaigns and sampling.

The authors declare that they have no conflict of interest.

References

1. Taylor JA, Prakash M, Pereira GG, et al (2010) Predicting Dross Formation in Aluminium Melt Transfer Operations. In: Materials Science Forum. https://www.scientific.net/MSF.630.37. Accessed 2 Nov 2018

2. Gomez A, Lima NB, Tenorio JAS (2008) Quantitative Analysis of Aluminum Dross by the Rietveld Method. Mater Trans 49:728–732. https://doi.org/10.2320/matertrans.MRA2007129

3. Cochran CN, Sleppy WC (1961) Oxidation of High-Purity Aluminum and 5052 Aluminum-Magnesium Alloy at Elevated Temperatures. J Electrochem Soc 108:322–327. https://doi.org/10.1149/1.2428080

4. Miresmaeili SM (2009) Effect of Strontium on the Oxidation Behavior of Liquid Al–7Si Alloys. Oxid Met 71:107–123. https://doi.org/10.1007/s11085-009-9136-3

5. Ha S-H, Yoon Y-O, Kim SK (2014) Effect of Al_2Ca on Oxidation Resistance and Tensile Property of Al-5Mg Alloy. Journal of Korea Foundry Society 34:194–199. https://doi.org/10.7777/jkfs.2014.34.6.194

6. Meshram A, Gautam D, Singh KK (2020) Recycling of White Aluminium Dross: Production of Potash Alum. Trans Indian Inst Met 73:1239–1248. https://doi.org/10.1007/s12666-020-01973-1

7. Abdulkadir A, Ajayi A, Hassan MI (2015) Evaluating the Chemical Composition and the Molar Heat Capacities of a white Aluminum Dross. Energy Procedia 75:2099–2105. https://doi.org/10.1016/j.egypro.2015.07.326

8. Peterson RD (2011) A Historical Perspective on Dross Processing. Materials Science Forum 693:13–23. https://doi.org/10.4028/www.scientific.net/MSF.693.13

9. Aluminium Dross Processing: A Global Review. In: alcircle. https://www.alcircle.com/specialreport/306/drossprocessing. Accessed 22 Oct 2020

10. Bergsmark E, Simensen CJ, Kofstad P (1989) The Oxidation of Molten Aluminum. Materials Science and Engineering: A 120–121:91–95. https://doi.org/10.1016/0921-5093(89)90723-5

11. Solem CKW, Vullum PE, Tranell G, Aune RE (2022) Heat Treatment of Mg-Containing Aluminum Alloys 5182 and 6016 in an Oxidizing Atmosphere with 4% CO_2. In: Eskin D (ed) Light Metals 2022. Springer International Publishing, Cham, pp 587–593

12. Bui RT, Perron J (1988) Performance Analysis of the Aluminum Casting Furnace. Metall Mater Trans B 19:171–180. https://doi.org/10.1007/BF02654201

13. Bonner SJ, Taylor JA, Yao J-Y, Rhamdhani MA (2016) Oxidation of Commercial Purity Aluminum Melts: An Experimental Study. In: Sadler BA (ed) Light Metals 2013. Springer International Publishing, Cham, pp 993–997

14. Glazoff MV, Rashkeev SN (2010) Beryllium Adsorption at Transition Aluminas: Implications for Environmental Science and Oxidation of Aluminum Alloys. J Phys Chem C 114:14208–14212. https://doi.org/10.1021/jp1044942

15. Smith N, Gleeson B, Kvithyld A, Tranell G (2017) Effects of 2 ppm Beryllium on the Oxidation of a 5XXX Aluminum Alloy at Temperatures Between 500 and 750 °C. In: Ratvik AP (ed) Light Metals 2017. Springer International Publishing, Cham, pp 1465–1474

16. Cooper RG, Harrison AP (2009) The Uses and Adverse Effects of Beryllium on Health. Indian J Occup Environ Med 13:65–76. https://doi.org/10.4103/0019-5278.55122

17. Yancey DD, DeYoung DH (1997) Calcium Contamination of Molten Al-Mg Alloys by Calcium Carbonate. In: Light Metals 1997. pp 1035–1041

18. Smith N, Gleeson B, Saidi W, et al (2019) Effects of CO_2 Cover Gas and Yttrium Additions on the Oxidation of AlMg Alloys. In: Chesonis C (ed) Light Metals 2019. Springer International Publishing, Cham, pp 1025–1032

19. Smith N, Gleeson B, Saidi WA, et al (2019) Mechanism Behind the Inhibiting Effect of CO_2 on the Oxidation of Al–Mg Alloys. Ind Eng Chem Res 58:1434–1442. https://doi.org/10.1021/acs.iecr.8b04691

20. Solem CKW, Vullum PE, Ebadi M, et al (2022) The Role of CO_2 in the Oxidation-Protection of Mg-Containing Aluminum Alloys. Metall Mater Trans B. https://doi.org/10.1007/s11663-022-02524-3

21. Kvithyld A, Bao S, Nordmark A, et al (2014) Development of a Sampling Device for Furnace Dross. In: Grandfield J (ed) Light Metals 2014. Springer International Publishing, Cham, pp 931–935

22. Solem CKW, Deledda S, Tranell G, Aune RE (2022) Sampling Procedure, Characterization, and Quantitative Analyses of Industrial Aluminum White Dross. Submitted to Journal of Sustainable Metallurgy

23. Solem CKW, Zedel H, Tranell G, Aune RE (2023) Characterization of Low- and High Mg-Containing Aluminum White Dross Using Deterministic Image Analysis of EPMA Images. To be submitted to Light Metals 2023

24. Kudyba A, Akhtar S, Johansen I, Safarian J (2021) Aluminum Recovery from White Aluminum Dross by a Mechanically Activated Phase Separation and Remelting Process. JOM 73:2625–2634. https://doi.org/10.1007/s11837-021-04730-x

ISBN 978-82-326-6390-3 (printed ver.)
ISBN 978-82-326-6606-5 (electronic ver.)
ISSN 1503-8181 (printed ver.)
ISSN 2703-8084 (online ver.)

NTNU
Norwegian University of
Science and Technology